Analysis of Long-Term Sediment Loadings from the Upper North Fork Toutle River System, Mount St Helens, Washington

U.S. Department of Agriculture – Agricultural Research Service
National Sedimentation Laboratory
Watershed Physical Processes Research Unit
National Sedimentation Laboratory Technical Report Number 77.
January 2012

Andrew Simon* and Danny Klimetz

*Previously affiliated with NSL. Current affiliation and contact information: Cardno ENTRIX, 1223 Jackson Ave. East, Suite 301, Oxford MS, 662.236.6983; Andrew.simon@cardno.com

UNITED STATES DEPARTMENT OF AGRICULTURE
Agricultural Research Service

Analysis of Long-Term Sediment Loadings from the Upper North Fork Toutle River System, Mount St Helens, Washington

Prepared by

U.S. Department of Agriculture – Agricultural Research Service
National Sedimentation Laboratory
Watershed Physical Processes Research Unit

For

U.S. Army Corps of Engineers, Portland District

January 2012

CONTENTS

LIST OF FIGURES

LIST OF TABLES

LIST OF ABBREVIATIONS AND UNITS

a	exponent assumed to equal 1.0
A	shear surface or flow area, in square meters, m^2
A_r	root area in the plane of the shear surface, in square meters; m^2
BSTEM	Bank-Stability and Toe-Erosion Model
c'	effective cohesion, in kilopascals; kPa
c_a	apparent cohesion, in kilopascals; kPa
c_f	non-dimensional bed roughness coefficient
c_r	cohesion due to roots, in kilopascals; kPa
d, D	root diameter, or characteristic diameter of bed sediment, in meters; m
D_{50}	median diameter of grains in the bed, in millimeters; mm
dA	debris avalanche
DA	drainage area, in square kilometers; km^2
DEM	Digital Elevation Model
DOQ	Digital Orthophoto Quadrangle
e	multiplier in the root tensile stress- root diameter function (MPa m^{-b})
E	erosion distance, in centimeters; cm or elevation of the channel bed, in meters; m
f	exponent in the root tensile stress- root diameter function (dimensionless)
FBM	Fiber-bundle models
F_P	root pullout force, in Newtons; N
F_s	Factor of Safety
g	acceleration due to gravity, in meters per square second; 9.807 m s^{-2}
h	flow depth, head of water above mid-point of layer, or groundwater elevation, in meters; m
H	bank height, in meters; m
i	layer, node, root, or flow segment index
I	total number of soil layers, or roots crossing the shear plane
k	erodibility coefficient, in cubic centimeters per Newton second; $cm^3N^{-1}s^{-1}$ or cubic meters per Newton second; $m^3N^{-1}s^{-1}$
K_r	relative permeability
K_{sat}	saturated hydraulic conductivity, in meters per second; m s^{-1}
l	curve-fitting parameter in the van Genuchten (1980) equation, per meter; m^{-1}
L_r	root length, in meters; m
LiDAR	Light Detection And Ranging
m	curve-fitting parameter in the van Genuchten (1980) equation

n	Manning’s roughness coefficient, in seconds per cubic root of a meter; s m$^{-1/3}$. If present, the subscripts g, f and v signify the grain, form and vegetal components of the roughness
NFT	North Fork Toutle River
Q	bankfull discharge, in cubic meters per second; m^{3}s^{-1}
Q_s	bed-material discharge per unit channel width, or sediment load, in cubic meters per meter per second; m^{3} m^{-1} s^{-1}
P	hydrostatic-confining force due to external water level, in kilonewtons per meter; kN m^{-1}
r	residual moisture content
R	hydraulic radius (area/wetted perimeter), in meters; m
s	saturated moisture content
S	channel gradient, in meters per meter; m m^{-1}
S_e	energy slope, in meters per meter; m m^{-1}
S_i	force produced by matric suction on the unsaturated part of the failure plane surface, in kilonewtons per meter; kN m^{-1}
SG	specific gravity, dimensionless
SRS	Sediment Retention Structure
t	time, in seconds; s
T_r	root tensile strength per unit area of soil = ultimate root tensile stress, in kilopascals; kPa
TOW	USGS gage at Tower Road
U	mean flow velocity, in meters per second; m s^{-1}
U_i	hydrostatic-uplift force on the saturated portion of the failure surface, in kilonewtons per meter; kN m^{-1}
UNFT	Upper North Fork Toutle River
USGS	United States Geologic Society
W	failure block weight, in kilonewtons; kN
z	water surface elevation, in meters; m
α	local bank angle, in degrees from horizontal
β	failure-plane angle, in degrees from horizontal
ζ	angle of a root at rupture relative to the failure plane, in degrees
γ_s	unit weight of sediment, in kilonewtons per cubic meter, kN m^{-3}
γVS	unit stream power
γ_w	unit weight of water, 9.807 kN m^{-3}
θ	angle of shear distortion, in degrees
Ω	total stream power
μ_a	pore-air pressure, in kilopascals; kPa
μ_w	pore-water pressure, in kilopascals; kPa

ν	kinematic viscosity of water, in square meters per second; $m^2 s^{-1}$
Θ	soil saturation
Θ_r	residual moisture content
Θ_s	saturated moisture content
ρ, ρ_w	density of water, in kilograms per cubic meter; 1000 kg m^{-3}
ρ_s	density of the sediment, in kilograms per cubic meter; 2650 kg m^{-3}
σ	normal stress on the shear plane, in kilopascals; kPa
τ	boundary shear stress, in Pascals; Pa
τ_c	critical shear stress, in Pascals; Pa
$\tau^*{}_c$	dimensionless critical shear stress
τ_s	soil shearing resistance, in kilopascals; kPa
τ_o	average bed shear stress, in Pascals; Pa. If present, the additional subscripts *g*, *f* and *v* signify the grain, form and vegetal components of the bed shear stress.
ϕ	angle of internal friction, in degrees
ϕ'	effective soil friction angle, in degrees
ϕ^b	angle describing the increase in shear strength due to an increase in matric suction ($\mu_a - \mu_w$), in degrees
χ	initial root orientation relative to the failure plane, in degrees

1. INTRODUCTION AND OBJECTIVES

Uncertainty regarding current estimates of long-term sediment loadings from Mount St. Helens is hampering sediment-management decisions on the lower Cowlitz River. A location map of the North Fork Toutle (NFT) River system which drains the study area is provided in Figure 1, showing the original N-1 earthen retention structure and Sediment Retention Structure (SRS). Previous research has clearly shown that the primary source of sediment is the debris avalanche, deposited in the upper North Fork Toutle River (UNFT) Valley during the May 18, 1980 eruptions of the mountain. Subsequent erosion of these deposits by fluvial action, undercutting of terrace (hummock) slopes and consequent mass failures continues to be an important, if not primary source of sediment (Simon, 1992; 1999; Major et al., 2000; West, 2002). Analysis of loadings, therefore, must explicitly account for bank/terrace instability. Sediment erosion from surrounding hillslopes peaked soon after the eruption and is no longer an important source (Simon, 1999).

"…Channel adjustments are rapidly dominated by widening…Sediment entrainment relies primarily on bank collapse…If bank instability persists, high sediment yield persists. When bank instability declines, sediment yield declines." (Major *et al*., 2000, p. 821). The questions, therefore, to be thoroughly researched and quantified regarding long term rates of erosion from the debris avalanche are: (1) the relative importance of bank erosion in total erosion from the debris avalanche, and (2) whether bank-erosion rates are declining with time. Assuming a stable channel bed and because bank retreat is at least partly controlled by the ability of the hydraulic forces acting at the bank toe to undercut the overlying bank mass, we can assume that as the channel widens, the shear stress applied by a given discharge will decrease with time as flow depth decreases. If the resistance (composition) of the bank-toe material remains unchanged as the bank retreats with time, the rate of hydraulic erosion and, therefore upper-bank collapse should also decrease with time. This scenario would ultimately lead to a decay in streambank/terrace erosion rates.

A significant amount of pertinent data, including time-series channel geometry, bed-material particle size, sediment loadings and flow are available for the area. The primary objectives of this work were to predict magnitudes and sources of sediment emanating from the UNFT Basin over the next 100 years and to determine whether these loadings are likely to remain constant at elevated levels, or decay at some rate. This report brings together empirical analysis of available channel geometry and digital elevation data, used to discern changes in erosion and deposition rates during the thirty years of post eruption channel adjustment, and numerical simulations of streambank and terrace erosion using the Bank-Stability and Toe-Erosion Model (BSTEM). Relations developed from analysis of empirical data were used to predict erosion rates, volumes and relative contributions of sources 100 years into the future. BSTEM was enhanced to dynamically simulate daily hydraulic and geotechnical processes over the next 100 years for the purpose of quantifying erosion rates, and to determine if those erosion rates have been and will continue to decay with time.

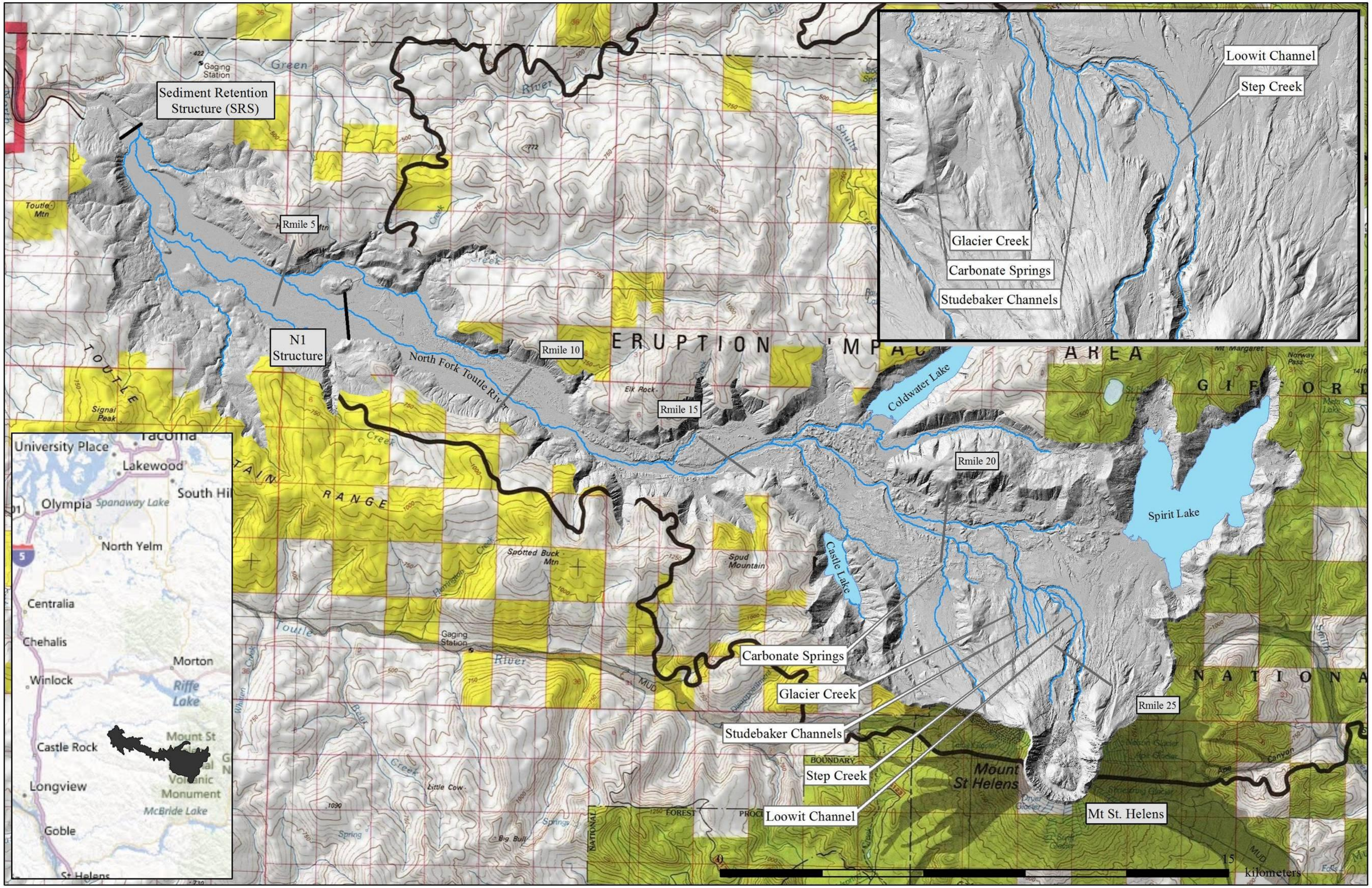

Figure 1. Location map of the upper North Fork Toutle River study area showing drainage network as of 2009, the locations of the Sediment Retention Structure (SRS) and original N-1 earthen retention structure.

2. BACKGROUND AND THEORY

2.1 Theoretical and Empirical Basis for Non-Linear Decay

It is well documented in the geomorphic literature that following large magnitude disturbances to alluvial systems, temporal adjustment of a whole host of variables typically follow patterns of non-linear decay that become asymptotic and reach minimum variance with time (Leopold and Langbein, 1962; Graf 1977). Variables used include: entropy production (Karcz, 1980); channel gradient (Simon and Robbins, 1987); sediment discharge (Parker, 1977; Simon, 1999); stream power (Bull, 1979; Simon, 1992) relative degradation (Begin et al., 1981; Williams and Wolman, 1984); relative roughness (Davies and Sutherland, 1983; Simon and Thorne, 1996); and flow energy and the rate of energy dissipation ((Simon, 1992; Simon and Thorne, 1996; Simon and Darby, 1997; Simon, 1999). This concept is summarized in Figure 2, which shows idealized adjustment trends for a site on the North Fork Toutle River (Simon and Rinaldi, 2006) with excess energy or stream power. The curves represent trends in important controlling variables computed for a single discharge based on relations from the literature cited above for periods of 10-100 years. The upper part of the figure represents non-linear decreases in available force or energy or sediment load with increasing time after the disturbance, while the bottom part represents increases in roughness and resistance to entrainment. Aspects of all of these attributes of non-linear adjustment have been documented for the UNFT (Simon, 1992; 1999; Major *et al.*, 2000; Major and Mark, 2006). Actual relations show considerably more scatter about the idealized trends as will be shown below.

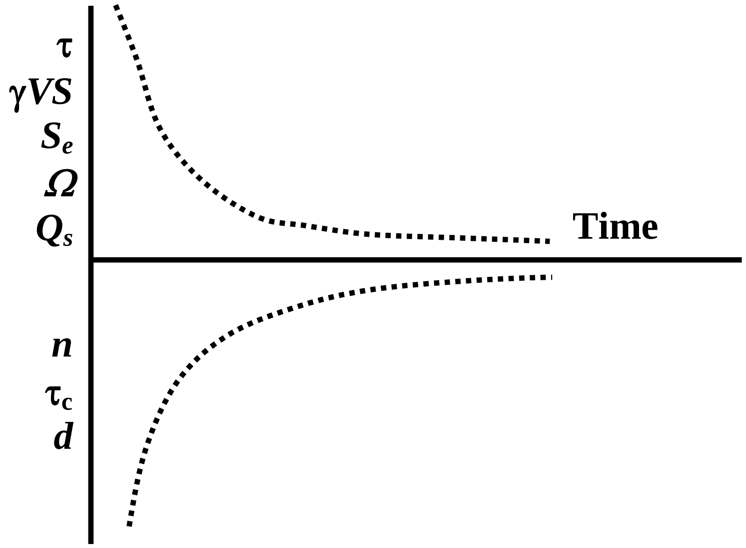

Figure 2. Idealized representation of adjustment trends in a reach with excess flow energy. Note: τ is boundary shear stress; γVS = unit stream power; S_e is the energy slope; Ω is total stream power; Q_s is sediment load; n is Manning's roughness; τ_c is critical shear stress; and d is the characteristic diameter of bed sediment. Adapted from Simon and Rinaldi (2006).

As shown in Figure 3, opposing trends of boundary and critical shear stress along the NFT indicate that bed-material coarsening with time is an integral part of channel adjustment and represents an additional degree of freedom in the Toutle River system (Simon and Thorne, 1996). In general, increases in critical shear stress as a result of bed-material coarsening exceed reductions in average boundary shear stress by a factor of about 1.8. Results demonstrate that development of a mobile pavement on the channel bed must be accounted for in assessing expected changes in channel geometry and sediment loads in highly unstable coarse-grained alluvial streams. Gomez (1983) also came to the conclusion that temporal variations in bed-load transport rates were, in part, a function of progressive armouring on the channel bed. If coarse-grained sediments (gravel and cobbles) had not been available, it is probable that increases in critical shear stress would have been limited and, therefore, geometric changes would have occurred at rates greater than those actually observed, to reduce values of boundary shear stress to levels commensurate with the erosional resistance of the finer bed sediments. Under this scenario, morphologic changes would be more drastic and cause high sediment discharges to persist for longer periods.

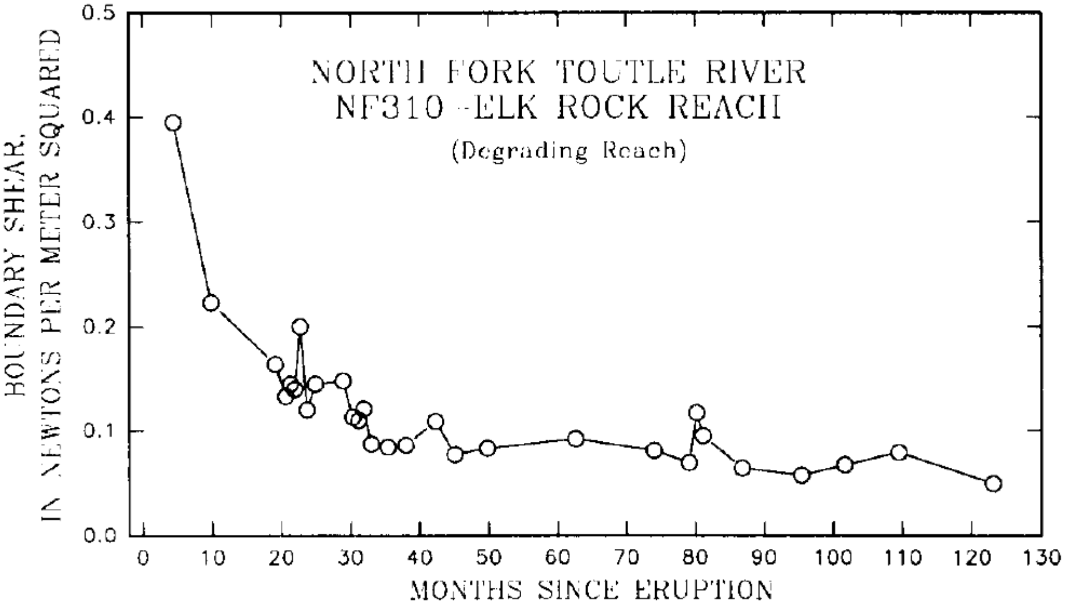

Figure 3. Non-linear decrease in average boundary shear stress due to morphologic adjustments for a constant discharge in the Elk Rock Reach, UNFT. Non-linear reductions in boundary shear stress result in non-linear decay of sediment loads (From Simon, 1992).

The non-linear, asymptotic nature of these relations for a given discharge is explained in terms of the magnitude of the difference between the available energy or stream power imposed by the post-disturbance stream channel, and the critical stream power. This imbalance is at a maximum immediately following a disturbance and results in a maximum rate of energy dissipation and morphologic change. In upstream reaches this occurs through changes in datum head (bed elevation), channel gradient, velocity head, hydraulic depth and roughness. Although adjustment is a continuous process acting over the range of flows, it is convenient for discussion to consider it as a series of discrete events. The initial maximum adjustment reduces excess energy or stream power by an amount proportional to the available energy and critical conditions for entrainment.

With a diminished amount of excess energy or stream power available for the next event, smaller changes occur. If this process is repeated over a number of events of equal magnitude, each successive adjustment will be smaller, resulting in a non-linear asymptotic adjustment function.

In the context of channel adjustment and the attainment of equilibrium conditions, Wolman (1955, p. 47) suggests "...the adjustment of channel shape may be as significant as the adjustment of the longitudinal profile." With time there is a decreased tendency for degradation relative to channel widening because of reductions in energy components that account for boundary shear stress - hydraulic radius and channel gradient:

$$\tau_o = \gamma RS \qquad (1)$$

where τ_o is the mean bed shear stress, in N/m^2 (Pa) and R is the hydraulic radius, in meters. Not only does boundary shear stress decrease with time (Figure 2), but resistance to bed erosion may increase by armoring of the channel bed and by the increase in relative roughness as channel depths decrease through widening. The resulting increase in hydraulic roughness and critical shear-stress, in combination, cause less rapid degradation with time. This provides a physical basis for the non-linear shape of the bed level functions.

Perturbations or oscillations around the generalized nonlinear functions (Figure 4) were caused by temporally short but dramatic changes in channel geometry during extreme flow events (Table 1). For example, the February 1982 storm and lake breach resulted in about 83 m of channel widening and 0.7 m of filling in the Elk Rock reach. The passage of a debris flow just one month later resulted in an average of only 1 m of widening but 6.2 m of incision, and resulted in an increase in head loss in the reach. However, even with the additional disruptions caused by a debris flow, the breaching of impoundments, and the addition of significant flows by human activities, general trends of minimization of energy dissipation were maintained (Figure 4). Critical dates in erosion of the debris avalanche (dA) are described in Table 1.

It is predominantly through the process of channel widening that hydraulic depths (Equation 1) can be maintained or decreased along degrading reaches of the coarse-grained Toutle River system. Without channel widening, incision, concentrated at locations of maximum boundary shear and unit stream power would result in increases in hydraulic depth, and not allow energy to decrease with time. In the UNFT system, channel widening represents an important mode of reducing specific energy, particularly early in the adjustment sequence. On the North Fork Toutle River, widening in the cohesionless bank materials associated with downcutting led to rapid reductions in energy dissipation (Simon, 1991) by causing reductions in hydraulic depths, datum heads, channel gradients, and velocity heads. Thus, if accompanied by channel degradation, widening can be the most effective means of minimizing energy dissipation and total-mechanical energy, and reducing specific energy, because all energy components decrease simultaneously.

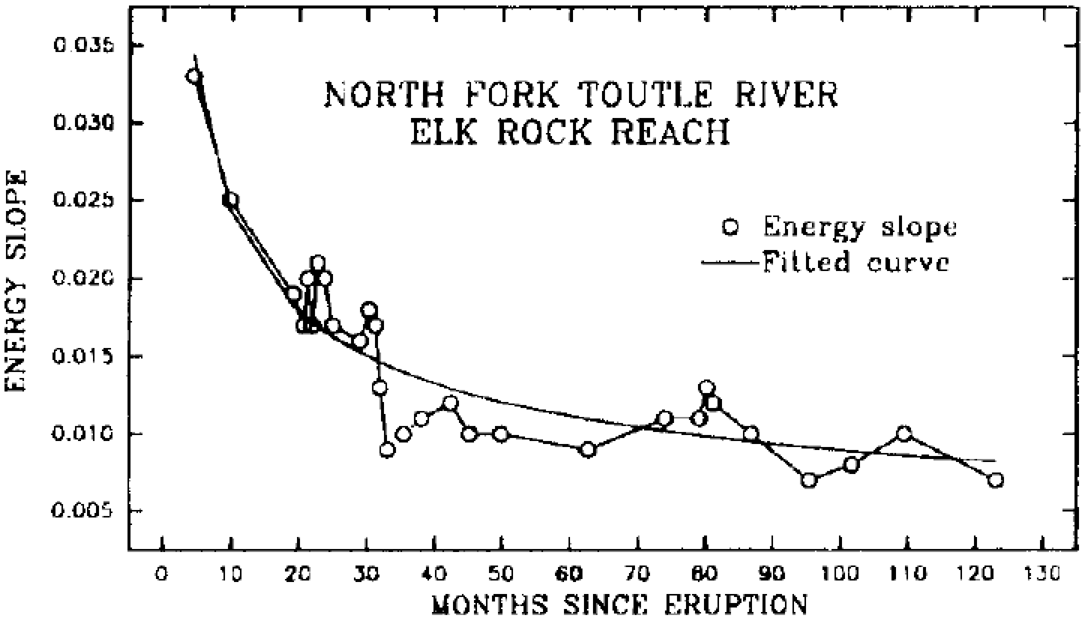

Figure 4. Maintenance of non-linear decay (adjustment) of energy slope in the Elk Rock Reach, UNFT notwithstanding additional perturbations caused by a debris flow and the breakout of Jackson Lake. From Simon, 1992.

Table 1. Integration of debris avalanche deposit and important dates in erosion of the blockage (Modified from R. Janda, U.S. Geological Survey, pers. comm., 1991)

Date	Lake breach	Estimated water volume (X 10^3 m^3)	Event and remarks
May 18, 1980	-	-	Emplacement of debris avalanche and formation of some channels by associated lahar
August 19, 1980	Marana Lake	-	-
August 27, 1980	Elk Rock Lake	310	Drainage above Elk Rock Reach
November 7, 1980	Carbonate Lake	165	-
January 25, 1982	Ponds on levee impounding Coldwater Lake	379	-
February 13, 1982	Ponds adjacent to northern avalanche boundary	710	Above Coldwater Reach
February 17, 1982	-	157	Probable breakout of ponds
February 20, 1982	-	385	Flood
February 20, 1982	Jackson Creek Lake	2470	Adjacent to Elk Rock Reach
March 19, 1982	-	-	Lahar; retention structure at toe of debris avalanche breached
November 5, 1982	-	-	Pumping from Spirit Lake into pilot channel starts
December 3, 1982	-	-	Flood; avalanche 100% integrated
April 5, 1985	-	-	Drainage from Spirit Lake through tunnel into South Coldwater Creek starts

3. MODELING OF PAST, PRESENT AND FUTURE EROSION RATES

Simulations of long-term streambank erosion rates were conducted using an enhanced version of the Bank-Stability and Toe-Erosion Model (BSTEM; Simon *et al*., 1999; 2000). To simulate long-term erosion rates, the model was enhanced to automatically handle time-series data which allowed for continuous simulation using daily time steps. This version of the model is called BSTEM-Dynamic, Version 1.0.

3.1 Bank Stability and Toe-Erosion Model (BSTEM)

BSTEM is a mechanistic bank-stability model specifically designed for alluvial channels. It is programmed in Visual Basic and exists in the *Microsoft Excel*© environment as a simple spreadsheet tool. Data input, along with the various sub-routines are included in different worksheets including *Input Geometry*, *Bank Material*, *Bank Vegetation and Protection*, *Bank Model Output* and *Toe Model Output*. The user is able to move freely between worksheets according to their needs at various points of model application. The most up to date "static" version of BSTEM (Version 5.4) is available to the public free of charge at http://www.ars.usda.gov/Research/docs.htm?docid=5044.

3.1.1 General Model Capabilities

The original model developed by Simon *et al*. (1999; 2000) is a Limit Equilibrium analysis in which the Mohr-Coulomb failure criterion is used for the saturated part of the streambank, and the Fredlund *et al*. (1978) criterion is used for the unsaturated part. The latter criterion indicates that apparent cohesion changes with matric suction (negative) pore-water pressure, while effective cohesion remains constant. In addition to accounting for positive and negative pore-water pressures, the model incorporates complex geometries, up to five user-definable layers, changes in soil unit weight based on water content, and external confining pressure from streamflow. Current versions combine three limit equilibrium-method models that calculate Factor of Safety (F_s) for multi-layer streambanks. The methods simulated are horizontal layers (Simon et al., 2000), vertical slices with tension crack (Morgenstern and Price, 1965) and cantilever failures (Thorne and Tovey, 1981). The model can easily be adapted to incorporate the effects of geotextiles or other bank-stabilization measures that affect soil strength.

BSTEM includes a sub-model to predict bank-toe and bank-surface erosion and undercutting by hydraulic shear. This is based on an excess shear-stress approach that is linked to the geotechnical algorithms. Complex geometries resulting from simulated bank-toe erosion are used as the new input geometry for the geotechnical part of the bank-stability model. The geometry of the potential failure plane can be input by the user or can be determined automatically by an iterative search routine that locates the most critical failure-plane geometry. In previous "static" versions of the model, if a failure is simulated, that new bank geometry can be exported back into either sub-model to simulate conditions over time by running the sub-models iteratively with different flow and water-table conditions. To efficiently simulate 100 years of flow data, however, BSTEM was enhanced to conduct these iterations automatically using daily time steps.

In addition, the bank-stability sub-model automatically selects between cantilever and planar-failure modes. The mechanical, reinforcing effects of riparian vegetation (Simon and Collison, 2002; Micheli and Kirchner, 2002) can be included in model simulations. This is accomplished with the RipRoot model (Pollen and Simon, 2005) that is based on fiber-bundle theory and included in the *Bank Vegetation and Protection* worksheet.

3.2 Bank-Toe Erosion Sub-Model

The magnitude of bank-face, bank-toe and bed erosion, and the extent of bank steepening by hydraulic forces are critical to accurately modeling streambank erosion. The Bank-Toe Erosion sub-model is used to estimate erosion of bank and bank-toe materials by hydraulic shear stresses. The effects of toe protection are incorporated into the analysis by changing the characteristics of the toe material in the model. The model calculates an average boundary shear stress from channel geometry and flow parameters using a rectangular-shaped hydrograph defined by flow depth and the duration of the flow (steady, uniform flow). The assumption of steady, uniform flow is not critical insomuch as the model does not attempt to rout flow and sediment and is used only to establish the boundary shear stress for a specified duration along the bank surface. The model also allows for different critical shear stress and erodibility of separate zones with potentially different materials at the bank and bank toe. The bed elevation is fixed because the model does not incorporate the simulation of bed sediment transport.

3.2.1 Predicting the Distribution of Shear Stress along the Bank Face

The distribution of shear stress vertically along the streambank is calculated using an algorithm that computes the hydraulic force acting on the near-bank zone during a particular flow event. The boundary shear stress exerted by the flow on each node, i, is estimated by dividing the flow area at a cross-section into segments that are affected only by the roughness of the bank or the bed and then further subdividing to determine the flow area affected by the roughness on each node (e.g. Einstein, 1942; Figure 5).

The procedure is as follows:

1. Extend a bisector through the base of the bank toe to the water surface at an angle that is the average of the two nodes closest to the base of the bank toe (Figure 5; label 1);
2. Determine the mid-points between nodes on the bank face (Figure 5; label 2);
3. Compute the absolute vertical distance between the mid-points on the bank face and bank toe and compute the total absolute vertical distance encompassed by the mid-points of the bank face and bank toe nodes. Split the water surface between the water-bank intersect and the intersect of the line drawn in step 1 into segments with lengths that are proportional to the ratio between the absolute vertical distance between each mid-point and the total absolute vertical distance (Figure 5; label 3); and
4. For each node, i, the hydraulic radius of a segment, R_i, is the area of the flow segment formed (delineated by dashed lines in Figure 5), A_i, divided by the wetted perimeter of the segment. The boundary shear stress active at the node i may then be estimated from Equation 1.

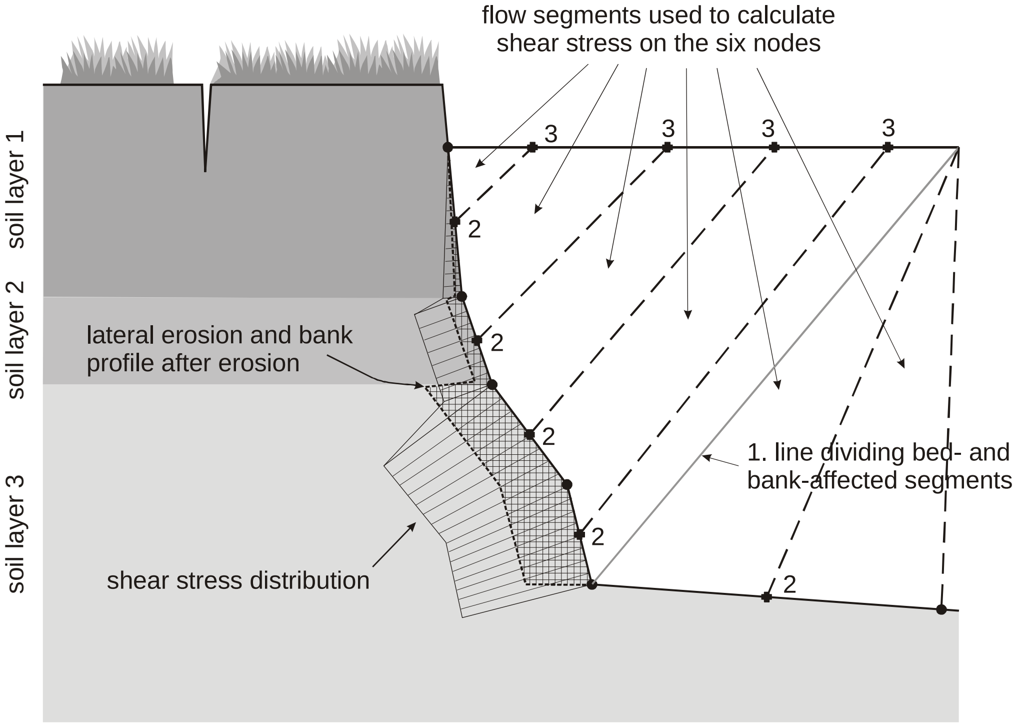

Figure 5. Segmentation of local flow areas and hydraulic radii.

Flow resistance in an open channel is a result of viscous and pressure drag over its wetted perimeter. For a vegetated channel, this drag may be conceptually divided into three components: 1) the sum of viscous drag on the ground surface and pressure drag on particles or aggregates small enough to be individually moved by the flow (grain roughness); 2) pressure drag associated with large non-vegetal boundary roughness (form roughness); and 3) drag on vegetal elements (vegetal roughness) (Temple *et al*., 1987). As energy lost to the flow represents work done by a force acting on the moving water, the total boundary shear stress may also be divided into three components:

$$\tau_o = \tau_{og} + \tau_{of} + \tau_{ov} \tag{2}$$

where the subscripts *g*, *f* and *v* signify the grain, form and vegetal components of the boundary shear stress, respectively.

If it is assumed that these components may be expressed in terms of a Manning's coefficient for each, and Manning's equation is assumed to apply for each component, equation 8 can be rewritten as (Temple, 1980):

$$n^2 = n_g^2 + n_f^2 + n_v^2 \tag{3}$$

where n = Manning's roughness coefficient (s m$^{-1/3}$). Grain roughness is estimated for each node on the bank profile using the equation of Strickler (Chow, 1959):

$$n_g = 0.045\,(D_{50}^{1/6}) \tag{4}$$

Combining equations 2 and 3, the effective boundary shear stress, the component of the boundary shear stress acting on the boundary in the absence of form and vegetal roughness, may be computed as:

$$\tau_g = \tau_o \, (n_g^2 / n^2) \tag{5}$$

An average erosion rate (in m/s) is computed for each node by utilizing an excess-shear stress approach (Partheniades, 1965). This rate is then integrated with respect to time to yield an average erosion distance in centimeters.

$$E = k \, \Delta t \, (\tau_0 - \tau_c) \tag{6}$$

where E = erosion distance (cm), k = erodibility coefficient (cm^3/N-s), Δt = time step (s), τ_0 = average boundary shear stress (Pa), and τ_c = critical shear stress (Pa).

3.2.2 Resistance to Hydraulic Erosion

Whether sediment is entrained by a moving fluid depends on both the properties of the fluid (i.e. its density, viscosity and velocity) and the physical properties of the sediment, such as its size, shape, density and arrangement (Knighton, 1998). A basic distinction exists between the entrainment of non-cohesive sediment (usually coarse silt, sand, gravel and boulders or cobbles) and cohesive sediments, because the entrainment of the latter is complicated by the presence of cohesion (Knighton, 1998). In both cases, most approaches to sediment transport have relied upon the concept of a critical value of a parameter such as either the depth-averaged or near-bed velocity (Hjulström, 1935), unit stream power (Bagnold, 1966; Yang, 1973) or bed shear stress (e.g. Meyer-Peter and Müller, 1948; Laursen, 1958; van Rijn, 1984a; 1984b; Parker, 1990; Wu *et al.*, 2000 and many others). Herein, we employ the bed shear stress, τ_o, as the independent variable.

Resistance of bank-toe and bank-surface materials to erosion by hydraulic shear is handled differently for cohesive and non-cohesive materials. Originally, for cohesive materials the relation developed by Hanson and Simon (2001) using a submerged jet-test device (Hanson, 1990; 1991) was used:

$$k = 0.2 \, \tau_c^{-0.5} \tag{7}$$

This relation has been recently updated based on hundreds of tests on streambank materials across the United Sates (Simon *et al., 201*):

$$k = 1.62 \, \tau_c^{-0.838} \tag{7a}$$

Most of the sediments in the Upper North Fork Toutle River are non-cohesive. The Shields (1936) criterion is used for resistance of non-cohesive materials as a function of roughness and particle size (weight), and is expressed in terms of a dimensionless critical shear stress (Figure 6):

$$\tau^*_c = \tau_o / [(\rho_s - \rho_w) \, g \, D] \tag{8}$$

where τ^*_c = critical dimensionless shear stress, ρ_s = sediment density (kg/m^3), ρ_w = water density (kg/m^3), g = gravitational acceleration (m/s^2), and D = characteristic particle diameter (m).

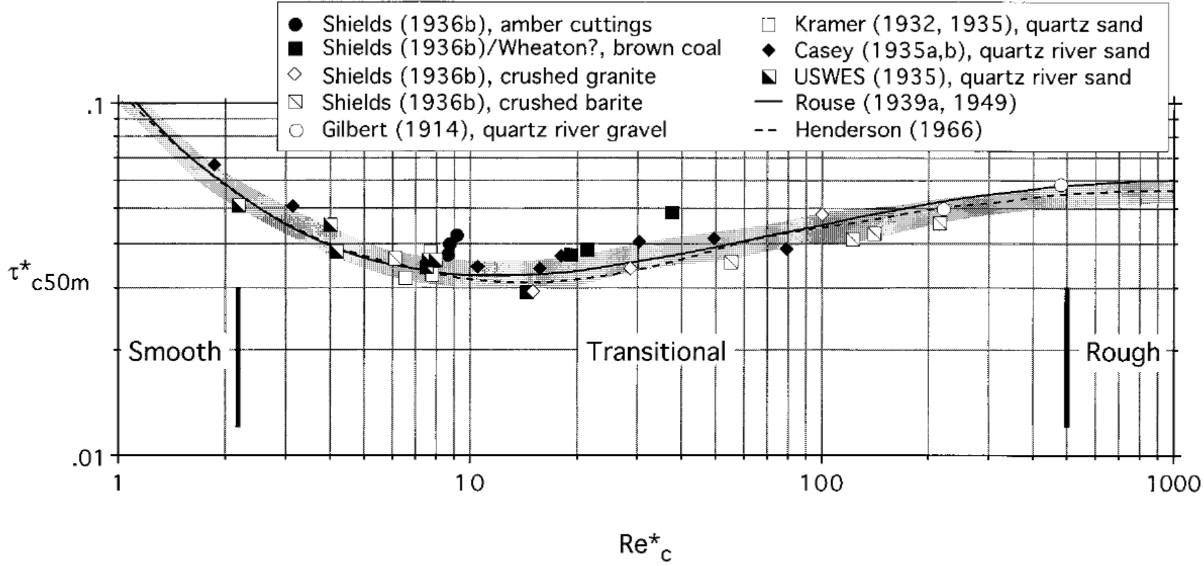

Figure 6. Shields diagram for incipient motion (modified from Buffington, 1999). The *y*-axis is defined by Equation 1 and the *x*-axis is defined by Equation 2.

3.2.3 Quantifying the Resisting and Driving Geotechnical Forces

Soil shear strength varies with the moisture content of the bank and the elevation of the saturated zone in the bank mass. In the part of the streambank above the "normal" level of the groundwater table, bank materials are unsaturated, pores are filled with both water and air, and pore-water pressure is negative. The difference ($\mu_a - \mu_w$) between the air pressure, μ_a, and the water pressure in the pores, μ_w, represents matric suction. The increase in shear strength due to an increase in matric suction ($\mu_a - \mu_w$) is described by the angle ϕ^b. ϕ^b varies for all soils and with moisture content for a given soil (Fredlund and Rahardjo, 1993), but generally takes a value between 10° and 20°, with a maximum of the effective soil friction angle, ϕ', under saturated conditions (Fredlund and Rahardjo, 1993). The effect of matric suction on shear strength is reflected in the apparent cohesion (c_a) term, which incorporates both electro-chemical bonding within the soil matrix (described by the effective cohesion, c') and cohesion due to surface tension on the air-water interface of the unsaturated soil:

$$c_a = c' + (\mu_a - \mu_w)\tan\phi^b \tag{9}$$

where c_a = apparent cohesion (kPa), c' = effective cohesion (kPa), μ_a = pore-air pressure (kPa), μ_w = pore-water pressure, ($\mu_a - \mu_w$) = matric suction (kPa) and ϕ^b is the angle describing the increase in shear strength due to an increase in matric suction (degrees).

As can be seen from Equation 9, negative pore-water pressures (positive matric suction) in the unsaturated zone provide for cohesion greater than the effective cohesion, and thus, greater shearing resistance. This is often manifest in steeper bank slopes than would be indicated by ϕ'. Conversely, the wetter the bank and the higher the water table, the weaker the bank mass becomes and the more prone it is to failure. Accounting for the effects of friction, the shear strength of a soil, τ_s, may thus be described by the Mohr-Coulomb shear strength criterion for unsaturated soils (Fredlund *et al*., 1978):

$$\tau_s = \left[c' + (\mu_a - \mu_w)\tan\phi^b + (\sigma - \mu_a)\tan\phi'\right] \tag{10}$$

where σ = normal stress on the shear plane (kPa) and ϕ' = effective angle of internal friction (degrees).

While it is assumed that the pore-air pressure is atmospheric (i.e. $\mu_a = 0$), positive and negative pore-water pressures are calculated for the mid-point of each layer based on hydrostatic pressure above and below the water table so that:

$$\mu_w = \gamma_w h \tag{11}$$

where μ_w = pore-water pressure (kPa), γ_w = unit weight of water (9.807 kN m^{-3}) and h = head of water above the mid-point of the layer (m).

For saturated parts of the failure plane Equation 10 simplifies to:

$$\tau_s = \left[c' + (\sigma - \mu_a)\tan\phi'\right] \tag{12}$$

The geotechnical driving forces are controlled by bank height and slope, the unit weight of the soil and the mass of water within it, and the surcharge imposed by any objects on the bank top.

3.3 Root Reinforcement Sub-Model (RipRoot)

Soil is generally strong in compression, but weak in tension. The fibrous roots of trees and herbaceous species are strong in tension but weak in compression. Root-permeated soil, therefore, makes up a composite material that has enhanced strength (Thorne, 1990). Numerous authors have quantified this reinforcement using a mixture of field and laboratory experiments. Endo and Tsuruta (1969) used in situ shear boxes to measure the strength difference between soil and soil with roots. Gray and Leiser (1982) and Wu (1984) used laboratory-grown plants and quantified root strength in large shear boxes.

Many studies have found an inverse power relationship between ultimate tensile stress, T_r, and root diameter, d (examples include but are not limited to: Waldron and Dakessian, 1981; Riestenberg and Sovonick-Dunford, 1983; Coppin and Richards, 1990; Gray and Sotir, 1996; Abernethy and Rutherfurd, 2001; Simon and Collison, 2002; Pollen and Simon, 2005; Fan and Su, 2008):

$$T_r = e(1000d)^f \tag{13}$$

where e = multiplier (MPa m^{-f}), and f = exponent (dimensionless) in the root tensile stress-diameter function, respectively. Note that f is always negative. Root tensile strength (in kN) can therefore be evaluated as the product of the root area, A_r ($\pi d^2/4$), and the ultimate tensile stress, T_r:

$$T_r A_r = \frac{e\pi\left(1000^{1+f}\right)d^{2+f}}{4} \tag{14}$$

Smaller roots are stronger per unit area (higher ultimate tensile stress), but the larger cross-sectional area of larger diameter roots means that the peak load they can withstand before breaking is higher than that of small roots.

Wu *et al*. (1979, after Waldron, 1977) developed a widely-used equation that estimates the increase in soil strength (c_r) as a function of root tensile strength, areal density and root distortion during shear:

$$c_r = \frac{1}{A}\sum_{i=1}^{i=I}\left(A_r T_r\right)_i\left[sin(90-\zeta)+cos(90-\zeta)tan\,\phi'\right] \tag{15}$$

where c_r = cohesion due to roots (kPa), T_r = tensile strength of roots (kPa), A_r = area of roots in the plane of the shear surface (m^2), A = area of the shear surface (m^2), I = total number of roots crossing the shear plane, the subscript i = i^{th} root, and

$$\zeta = \tan^{-1}\left(\frac{1}{\tan\theta+\cot\chi}\right) \tag{16}$$

where θ = angle of shear distortion (degrees), and χ = initial orientation angle of fiber relative to the failure plane (degrees).

Pollen *et al*. (2004) and Pollen and Simon (2005) found that models based on Equation 14 tend to overestimate root reinforcement because it is assumed that the full tensile strength of each root is mobilized during soil shearing and that the roots all break simultaneously. This overestimation was largely corrected by Pollen and Simon (2005) by developing a fiber-bundle model (RipRoot) to account for progressive breaking during mass failure.

Fiber-bundle models (FBMs) have been widely used in the materials industry to aid in the understanding of composite materials (starting with the work of Daniels, 1945). They are easy to parameterize and incorporate the most important aspects of soil-root interactions, using a dynamic approach to remove the assumption that all of the roots in the soil matrix break simultaneously. When a load is applied to the bundle of fibers it is apportioned equally between all intact fibers (Daniels, 1945). The maximum load that can be supported by the bundle corresponds not to the weakest or strongest fiber, but to one of the fibers in the middle.

FBMs work by apportioning the total load applied to a bundle of N parallel fibers (roots) and then monitoring whether the load applied to the n^{th} fiber exceeds its strength. The governing equation of a fiber-bundle model can therefore be written as:

Load to Break n^{th} Fiber = Total Applied Load / Number of Intact Fibers, N (17)

The term “break” does not differentiate between failure modes. Once the load has increased sufficiently for a fiber to break, the load that was carried by the broken fiber is redistributed equally amongst the remaining ($N-1$) intact roots, each of which then bears a larger load, and is hence more likely to break. If this redistribution causes further roots to break, additional redistribution of load occurs until no more breakages occur (in this type of model this is known as an avalanche effect). Another increment of load is then added to the system, and the process is repeated until either all of the fibers have broken, or the maximum driving force acting on the matrix is supported by the fibers contained within it.

RipRoot was validated by comparing results of root-permeated and non-root-permeated direct-shear tests. These tests revealed that, relative to results obtained with the perpendicular model of Wu *et al*. (1979), accuracy was improved by an order of magnitude, but some error still existed (Pollen and Simon, 2005). One explanation for the remaining error in root-reinforcement estimates lies in the fact that observations of incised streambanks suggest that when a root-reinforced soil shears, two mechanisms of root failure occur: root rupture and root pullout. The anchorage of individual leek roots was studied by Ennos (1990), who developed a function for pullout forces based on the strength of the bonds between the roots and soil:

$$F_P = \pi d \tau_s L_r \tag{18}$$

where F_P = pullout force for an individual root (N), and L_r = root length (m), which can be estimated in the absence of field data using $L_r = 123.1\ d^{\,0.7}$ (Pollen, 2007).

The pullout force was not accounted for in the original version of RipRoot (Pollen and Simon, 2005) and so the role played by spatio-temporal variations in soil shear strength was neglected. Pollen (2007) tested the appropriateness of Equation 21 through field measurements of the forces required to pull out roots. Pullout forces were then compared with breaking forces obtained from tensile strength testing and the RipRoot model was modified to account for both breaking and pullout. Thomas and Pollen-Bankhead (2010) improved Equation 21 by employing Rankine’s active earth pressure theory to compute τ_s. See Terzaghi and Peck (1967) for a description of Rankine’s active earth pressure theory.

A second explanation is that, following the work of Wu *et al*. (1979), it has commonly been assumed that the $\sin(90-\zeta) + \cos(90-\zeta)\tan\phi'$ term in equation 18 takes an approximately constant value of 1.2. Sensitivity analysis indicates that this assumption is flawed as this term varies from -1 when $\zeta = 60°$ to a maximum as $\zeta \rightarrow \phi'$ (Thomas and Pollen-Bankhead, 2010). A series of Monte Carlo simulations was undertaken, assuming that θ was uniformly distributed between 0° and 90° and assuming that χ was uniformly distributed between ±90° from the vertical, approximating a heartroot network. Friction angle was varied from 0° to 44° and failure plane angle was varied from 10° to 90°. For this assumed distribution, the $\sin(90-\zeta) + \cos(90-\zeta)\tan\phi'$ term was found to be independent of failure plane angle. In addition, for a given friction angle, the distribution of values was highly skewed, with the median and 84th percentile being approximately equal but the 4th percentile being much smaller (Thomas and Pollen-Bankhead, 2010). We found during tests that it was possible to predict the median value of the

$\sin(90-\zeta) + \cos(90-\zeta)\tan\phi'$ term using a cubic polynomial involving only the friction angle and this has been implemented herein.

The combination of the fiber bundle approach, in which roots break progressively during failure, the incorporation of pullout forces that vary as a function of the shear strength of the soil surrounding each root, and the variability in root orientation caused by local factors (e.g., water and nutrient availability, substrate and topographic variability) ensure that predictions of c_r cannot be readily extrapolated from one areal density to another nor from site to site.

3.4 Bank-Stability Sub-Model

The bank stability sub-model combines three limit equilibrium-methods to calculate a Factor of Safety (F_s) for multi-layered streambanks. The methods simulated are horizontal layers (Simon and Curini, 1998; Simon *et al.*, 2000), vertical slices for failures with a tension crack (Morgenstern and Price, 1965) and cantilever failures (Thorne and Tovey, 1981).

3.4.1 Planar Failures

For planar failures without a tension crack, the Factor of Safety (F_s) for both the saturated and unsaturated parts of the failure plane is given by the ratio of the resisting and driving forces:

$$F_s = \frac{\sum_{i=1}^{I}\left(c_i' L_i + S_i \tan\phi_i^b + \left[W_i \cos\beta - U_i + P_i \cos(\alpha-\beta)\right]\tan\phi_i'\right)}{\sum_{i=1}^{I}\left(W_i \sin\beta - P_i \sin[\alpha-\beta]\right)} \tag{19}$$

where c_i' = effective cohesion of ith layer (kPa), L_i = length of the failure plane incorporated within the ith layer (m), S_i = force produced by matric suction on the unsaturated part of the failure surface (kN/m), ϕ^b = angle representing the rate of increase in shear strength with increasing matric suction (^{o}), W_i = weight of the ith layer (kN), U_i = the hydrostatic-uplift force on the saturated portion of the failure surface (kN/m), P_i = the hydrostatic-confining force due to external water level (kN/m), β = failure-plane angle (degrees from horizontal), α = bank angle (degrees from horizontal), ϕ' = angle of internal friction (^{o}), and I = the number of layers.

The hydrostatic confining force, P_i, is calculated from the area of the confining pressure ($\gamma_w h$) by:

$$P_i = \frac{\gamma_w h^2}{2} \tag{20}$$

where h = head of water in the channel (m). The loss of the hydrostatic-confining force is the primary reason bank failures often occur after the peak flow and on the recessional limb of hydrographs.

3.4.2 Cantilever Failures

The cantilever shear failure algorithm results from inserting β = 90° into Equation 5 and simplifying. F_s is given by:

$$F_s = \frac{\sum_{i=1}^{I}\left(\left[c_i' + c_r\right]L_i + \left(\mu_a - \mu_w\right)_i L_i \tan\phi_i^b + \left[P_i \sin\alpha - \mu_{ai} L_i\right]\tan\phi_i'\right)}{\sum_{i=1}^{I}\left(W_i + P_i \cos\alpha\right)} \qquad (21)$$

Put simply, the F_s is the ratio of the shear strength of the soil to the weight of the cantilever. The inclusion of α-terms in Equation 21 ensures that if the bank is partially or totally submerged the weights of the layers affected by water are correctly reduced irrespective of the geometry of the basal surface of the overhang.

BSTEM can utilize the different failure algorithms depending on the geometry and conditions of the bank. Determining whether a failure is planar or cantilever is based on whether there is undercutting and then comparing the factor of safety values. The failure mode is automatically determined by the smaller of the two values.

3.4.3 Search Routine: Locating the Failure Geometry that Minimizes Fs

A minimum can be either global (truly the lowest function value) or local (the lowest in a finite neighborhood and not on the boundary of that neighborhood). Finding the global minimum is, in general, a very difficult problem (Press *et al*., 1992). Herein, we adopt one of the standard heuristics: at a user-defined number of failure base elevations, we isolate the failure plane angle that produces the minimum factor of safety. Once all the potential failure base locations have been searched, we select the minimum of all the local minima. This reduces our problem to a series of one-dimensional minimization problems. We follow the recommendation of Press *et al*. (1992): “For one-dimensional minimization (minimize a function of one variable) without calculation of the derivative, bracket the minimum… and then use Brent’s method... If your function has a discontinuous second (or lower) derivative, then the parabolic interpolations of Brent’s method are of no advantage, and you might wish to use the simplest form of golden section search.”

3.4.4 Modeling Movement of the Near-Bank Groundwater Table

It is apparent from Equations 19, 20, and 21 that the elevation of the groundwater table is an important parameter controlling soil shear strength. For the purposes of this study, a simplified one-dimensional (1-D) groundwater model, based on the 1-D Richards Equation, was developed to simulate the motion of the groundwater table. This model assumes that the dominant pressure gradient within a streambank is the difference between the groundwater table elevation and the in-channel water surface elevation (i.e., it neglects the influence of infiltrating precipitation) (e.g. Langendoen, 2010). Assuming that water infiltrates either into or out of the bank along a horizontal plane of unit length and computing distance-weighted mean soil properties between these two elevations, the simplified equation can be written as:

$$\frac{\partial h}{\partial t} - K_r K_{sat} \left| h - z \right|^2 = 0 \tag{22}$$

where h = groundwater elevation (m), z is the water surface elevation (m), t = time (s), and $K_r K_{sat}$ = relative permeability × saturated hydraulic conductivity. K_r is evaluated as $K_r = \Theta^{1/2}\left[1-\left(1-\Theta^{1/n}\right)^n\right]^2$, where Θ = soil saturation and, following van Genuchten (1980), Θ is evaluated as:

$$\Theta = \Theta_r + \frac{\Theta_s - \Theta_r}{\left[1+\left(\frac{[z-h]}{\alpha}\right)^{1/1-n}\right]^n} \tag{23}$$

where the subscripts r and s denote the residual moisture content and saturated moisture content (= porosity), and α and n are curve-fitting parameters defined by van Genuchten (1980). Note that if $h \geq z$, $K_r = 1$.

3.5 Model Enhancements Specific to this Study

To simulate streambank erosion over 100 years required additional model enhancements and assumptions. Channels of the UNFT are braided. During moderate- and high-flow events, channels commonly avulse from one side of the valley to the other, thereby placing the focus of hydraulic bank-toe erosion against both banks over time. Insomuch as BSTEM and BSTEM-Dynamic are single-bank models, we assumed that over the course of 100 years that bank erosion on each bank would be the same. Thus, simulations were conducted for one bank and resulting loading values were multiplied by two different methods, described later in the text.

3.5.1 Updating the Stage-Discharge Relation

BSTEM-Dynamic requires time series stage data for both the toe-erosion and groundwater sub-models. These data are generally obtained from daily discharge data applied to a normal-depth approximation to produce a stage discharge relation that is used to obtain daily stage. This is described in more detail in following sections on developing a flow series for sites along the UNFT. As the channel widens, however, the stage discharge relation changes as the flow depth for a given discharge decreases, resulting in lower shear stresses along the bank toe (assuming constant slope). This represents one of the mechanisms for the decay in streambank erosion rates with time. To accommodate the adjustments to the stage-discharge relation with time within the BSTEM-Dynamic code, the model re-calculates the stage-discharge relation every three months, or four times per year. Thus, over the course of the simulation, the relation between discharge and stage and, therefore, shear stress is adjusted 400 times. It is hoped that this provides a more accurate depiction of how applied boundary shear changes with time.

3.5.2 Hydraulic Resistance of Volcaniclastic Sediments on Banks

Predicting the hydraulic resistance (τ_c) of sediments at Mount St Helens is somewhat challenging given the variability in the specific gravity (*SG*) of the volcaniclastic materials. It is expected that the vesicular materials such as pumice and dacite would be of lower density, making a grain of a given diameter easier to entrain. The specific gravity of quartz-feldspar sediment is relatively constant with 99% of the material showing less than a 5% variation (Blatt *et al*., 1980). Work in the blast zone at Mount St Helens by Smith and Smith (1985) showed a general non-linear, inverse relation between *SG* and grain size for both blast dacite and pumice lapilli. The authors also determined that in general, the relative composition of materials emplaced by the blast was: 30% dacite, 30% pumice, 25% plagioclase, and 15% heavy minerals 15%. From this information we designed a method to adjust the unit weight (ρ_s in Equation 8) and critical shear stress (τ_c in Equation 6) of the sediment according to the *SG* of the material. Using the data provided in Smith and Smith (1985), regression equations were developed to predict the *SG* of the dacite and pumice as a function of particle size (Figure 7):

For dacite: $SG = 2.36\,D^{-0.036}$, $r^2 = 0.90$ (24a)

For pumice: $SG = 1.44\,D^{-0.09}$, $r^2 = 0.87$ (24b)

For other materials: $SG = 2.65$ (24c)

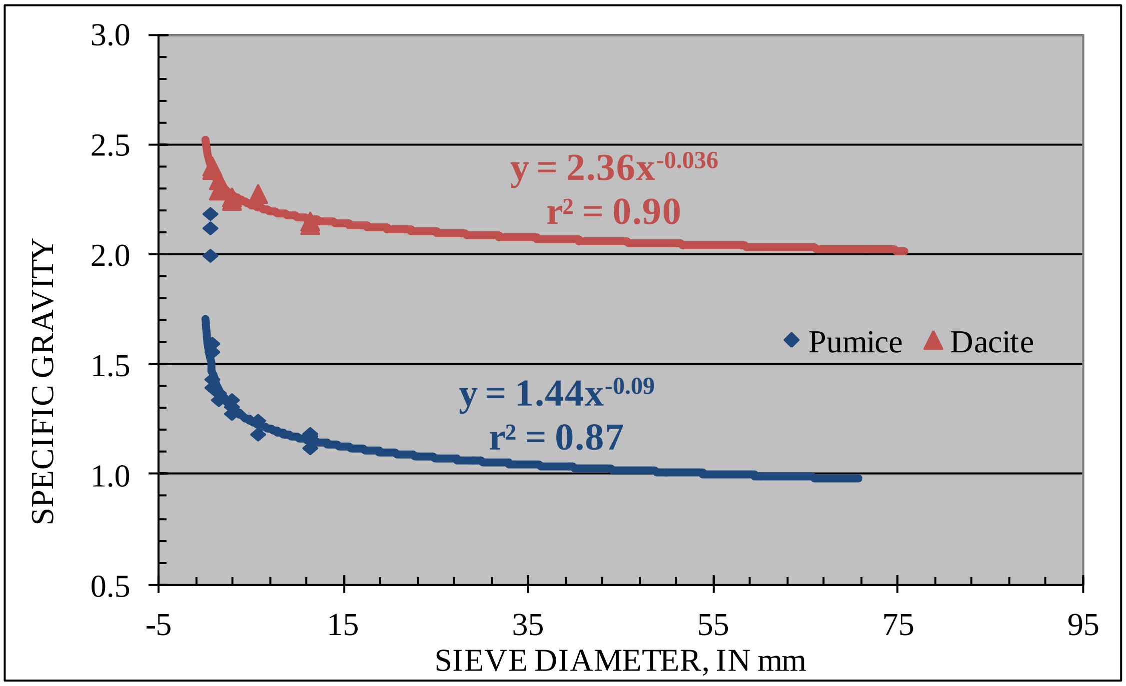

Figure 7. Regression relations for the variation in specific gravity with particle diameter. Raw data from Smith and Smith (1985).

Component critical shear stresses were then calculated for the d_{50} of the material by substituting the appropriate regression equations (above) for ρ_s in Equation 8 and multiplying the value by the relative contribution of the material (*ie*. 30% dacite, 25% plagioclase, etc., Smith and Smith, 1985). These values are then summed to obtain an adjusted τ_c that has been weighted according to the *SG* and the composition of the material. At small particle sizes,(< 0.5 mm) the affect of adjusting SG on decreasing τ_c is less than 4% but quickly increases to 30-40% in the gravel-size range (Figure 8). At a particle size of 256 mm the reduction in τ_c is about 55%.

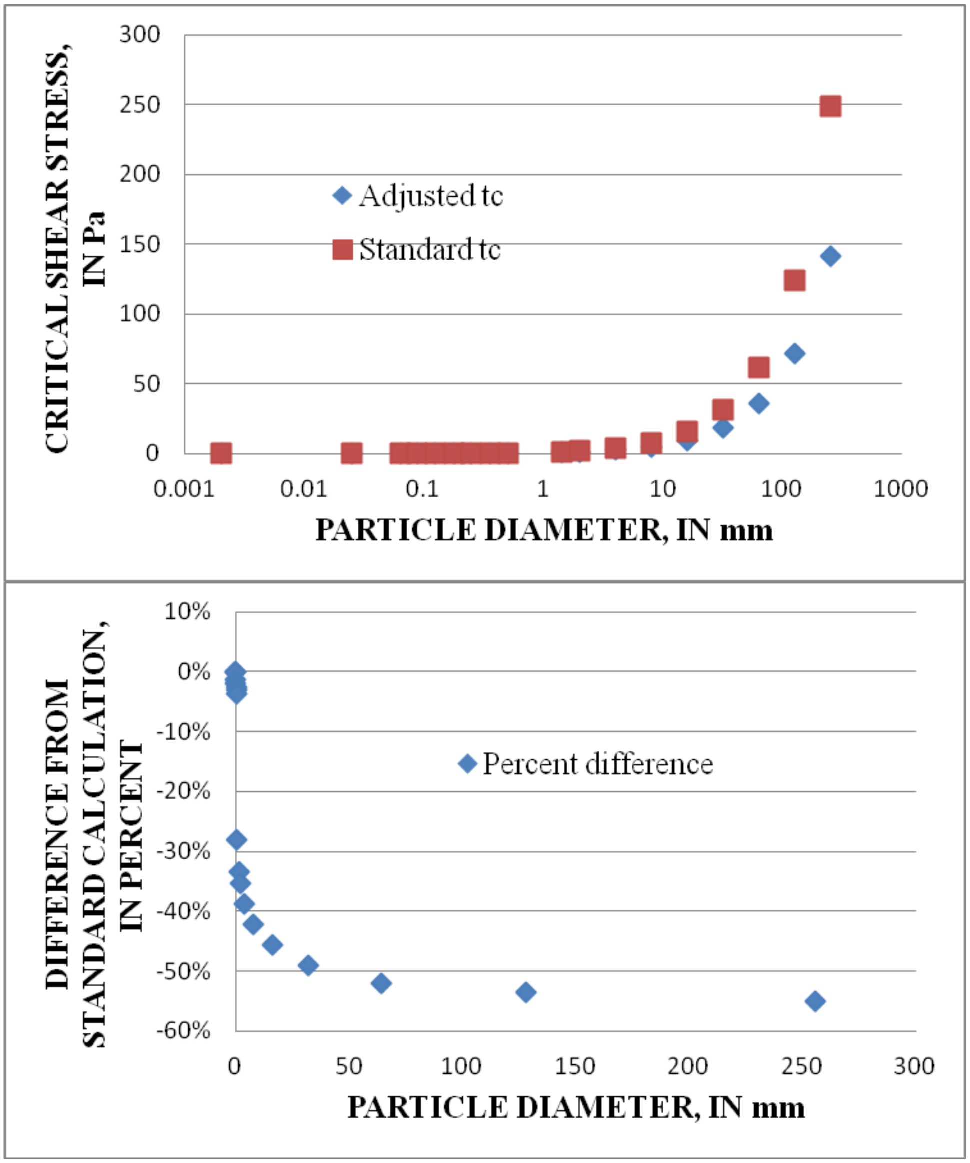

Figure 8. Comparison in calculated τ_c for given particle diameters using the standard value of specific gravity (2.65) and by adjusting specific gravity according to material composition and particle size (top); Percent differences between the two methods (bottom).

3.6 Data Requirements

As BSTEM is a mechanistic model, the data required to operate the model are all related to quantifying the driving and resisting forces that control the hydraulic and geotechnical processes that operate on a streambank. Input-parameter values can all be obtained directly from field surveying and testing. If this is not possible, the model provides default values by material type for many parameters. Required data fall into three broad categories: (1) bank geometry and stratigraphy, (2) hydraulic data, and (3) geotechnical data. A summary of the required input parameters is provided in Table 2. The default geotechnical values that are included in the model are provided in Table 3.

Table 2. Required user-input parameters for BSTEM.

Hydraulic Processes: Bank Surface					
Driving Forces			**Resisting Forces**		
Parameter	**Purpose**	**Source**	**Parameter**	**Purpose**	**Source**
Channel slope (S)	Boundary shear stress (τ_o)	Field survey or design plan	Particle diameter (D) *(cohesionless)*	Critical shear stress (τ_c)	Bulk sample particle size (*cohesionless*); Default values in model
			Critical shear stress (τ_c) *(cohesive)*	Critical shear stress (τ_c)	Jet test (*cohesive*); Default values in model
Flow depth (h)	Boundary shear stress (τ_o)	Field survey, gage information, design plan	Particle diameter (D) *(cohesionless)*	Erodibility coefficient (k)	Bulk sample particle size (*cohesionless*); Default values in model
			Critical shear stress (τ_c) *(cohesive)*	Erodibility coefficient (k)	Jet test (*cohesive*); Default values in model
Unit weight of water (γ_w)	Boundary shear stress (τ_o)	Considered constant, 9810 N/m^3			
Geotechnical Processes: Bank Mass					
Driving Forces			**Resisting Forces**		
Parameter	**Purpose**	**Source**	**Parameter**	**Purpose**	**Source**
Unit weight of sediment (γ_s)	Weight (W), Normal force (σ)	Core sample in bank unit; Default values in model	Unit weight of sediment (γ_s)	Weight (W), Normal force (σ)	Core sample in bank unit; Default values in model
Bank height (H)	Shear stress	Field survey or design plan	Effective cohesion (c')	Shear strength (τ_f)	Borehole shear, direct shear, triaxial shear; Default values in model
Bank angle (α)	Shear stress	Field survey or design plan	Effective friction angle (ϕ')	Shear strength (τ_f)	
			Pore-water pressure (μ_w)	Shear strength (τ_f)	Interpolated from water table

Table 3. Default values in BSTEM (bold) for geotechnical properties. Data derived from more than 800 *in situ* direct-shear tests with the Iowa Borehole Shear Tester except where indicated. From Simon *et al*., 2011.

Soil Type	**Statistic**	**c' (kPa)**	**ϕ' (degrees)**	**γ_{sat} (kN/m^3)**
Gravel (uniform)*		**0.0**	**36.0**	**20.0**
Sand and Gravel*		**0.0**	**47.0**	**21.0**
Sand	75th percentile	1.0	32.3	19.1
	Median	**0.4**	**30.3**	**18.5**
	25th percentile	0.0	25.7	17.9
Loam	75th percentile	8.3	29.9	19.2
	Median	**4.3**	**26.6**	**18.0**
	25th percentile	2.2	16.7	17.4
Clay	75th percentile	12.6	26.4	18.3
	Median	**8.2**	**21.1**	**17.7**
	25th percentile	3.7	11.4	16.9

* Data from Hoek and Bray (1977)

4. FIELD-DATA COLLECTION METHODS

4.1 Hydraulic Resistance

All of the materials encountered on the bank toes and low-bank surfaces were cohesionless. Because of this, values of the critical shear stress of the surface sediments that would be subjected to hydraulic forces were based on the particle-size distribution of the materials. If the materials were composed primarily of sand and fine gravel, a bulk sample was obtained and returned to the laboratory for an analysis of particle size. For coarser materials, the intermediate axis of 100 particles were measured and recorded. If more than 15 particles were characterized as sand or finer during the particle count, a bulk sample of these finer materials were obtained to be combined with the results of the particle count. Results of the laboratory analyses were then applied to Equation 8 to obtain τ_c.

4.2 Geotechnical Resistance

Although BSTEM-Dynamic can utilize default values for geotechnical parameters, *in situ* data provide more reliable measures of the geotechnical resistance of each streambank. Measurements of the unit weight of the sediments (γ_s) were obtained by extracting a 2 inch-diameter by 2 inch-long core from the bank face. These cores were capped to retain ambient matric suction and weighed in the laboratory. Values of γ_s were obtained by dividing the tared weight of the core by the volume of the core, and then multiplying by g.

Generally, we rely on the Iowa Borehole Shear Tester (Lohnes and Handy, 1968) operated within a borehole to obtain separate values of effective cohesion (c') and the angle of internal friction (ϕ). Because of the difficulties in hand auguring a borehole through the tall, coarse deposits of the debris avalanche, the following field methods were employed to provide values of shear strength.

The Torvane Shear Device is used to obtain rapid measurements of shear strength from a smooth surface of any inclination (Figure 9). The vane is pressed firmly into the materials to the depth of the vanes and rotated under constant normal force until the material fails. The maximum resistance is then read directly from the dial. The test takes a matter of seconds to complete allowing for multiple tests to be conducted in a short time. We conducted three to five tests in each material. While the Torvane Shear does provide a good indication of shear values and has a very good correlation between its readings and those of an unconfined compression test, readings are dependent on several factors, including operator methods and rate of load, progressive failure, plane orientation, and varying moisture levels. (Humboldt Manufacturing, 2011a). Differences in operator methods were minimized by having only two staff conduct all of the measurements.

Figure 9. Photographs of Torvane Shear Device (left) and Pocket Penetrometer (right) used to obtain geotechnical measurements of shearing resistance. Modified from Humboldt Manufacturing (2011a; 2011b).

One of the issues with relying on the Torvane Shear Device to obtain geotechnical measurements for use in slope-stability analyses such as BSTEM is that measurements are for *total shear strength* (τ_s), thereby combining the cohesive, frictional, and matric suction components (Equation 10). To obtain separate values of these parameters and to ultimately be able to calculate effective cohesion (c') from Equation 10, additional measurements of the components of total shear strength were conducted. Measurements of the angle of talus slopes composed of the same materials as those tested with the Torvane Shear Device were obtained to provide values for the angle of internal friction (ϕ'). Values for matric suction were obtained with a digital tensiometer and/or a relation between matric suction and moisture content developed from a series of *in situ* measurements during the field campaign. The last parameter value needed to calculate c' from Equation 10 was the normal stress (σ). This was obtained using a two-step process. A Pocket Penetrometer (Figure 9), generally used to measure compressive strength, provided a measure of the normal stress required to push a piston of 0.05 in^2 (0.32 cm^2) ¼" (6.35 mm) into the material. The stress required to accomplish this is then read directly from the scale indicator. Assuming that the stress required to push the Torvane Device is directly proportional to the stress required to insert the Penetrometer, a relation was developed between the area of the vanes multiplied by the depth (for the Torvane) and the area of the piston multiplied by the depth (for the Penetrometer). This value was then multiplied by the value obtained with the Penetrometer to obtain the normal stress (σ) employed during the Torvane tests. Values of effective cohesion (c') were obtained by then re-organizing Equation 10 and solving for c'.

Bulk samples of all bank layers were also collected for particle-size analysis. These data were used in conjunction with simulated volumes of erosion to predict erosion amounts by size class.

5. **SAMPLING AND TESTING LOCATIONS: THE STUDY AREA**

The study area encompasses the channels of the UNFT System from the breached N-1 earthen sediment-retention structure, 15.6 km upstream of the SRS upstream to the upstream-most sites on the main stem and tributary channels. This is a somewhat different geographical scope than was used in the empirical analysis which extended from N-1 to the source of the UNFT in the crater of Mount St Helens. Major tributaries included in the study are, Castle Creek, Coldwater Creek, Carbonate Springs, Glacier Creek, Truman Channel, Loowit Creek, Step Creek and Studebaker Creek (Figure 1). In total, field data were collected on both banks/terraces at 31 sites, with *'site'* defined as a valley cross section. (Figure 10). In some cases, particularly with the north-flowing channels draining to Loowit Creek, multiple channels were encountered and sampled (Table 4). All of the data required for input into BSTEM-Dynamic as described above and in Table 2 were collected. Channel-geometry data for all of the sites were surveyed in either 2009 or 2010. This work is described in greater detail in sections on the empirical analysis of channel adjustments since 1980. Throughout this report, distances along the UNFT are referenced to the SRS (ie. SRS is located at river kilometer [rkm] 0.0).

Table 4. Summary of site locations for field sampling and testing. [1]Includes same channels as those indicated for Step Creek.

Channel	Number of Sites	Sites with Multiple Channels
North Fork Toutle River	13	
Carbonate Springs	2	1
Castle Creek	1	
Coldwater Creek	1	
Glacier Creek	1	
Loowit Creek	4	2[1]
Step Creek	3	2
Studebaker Creek	2	2
Truman Channel	4	

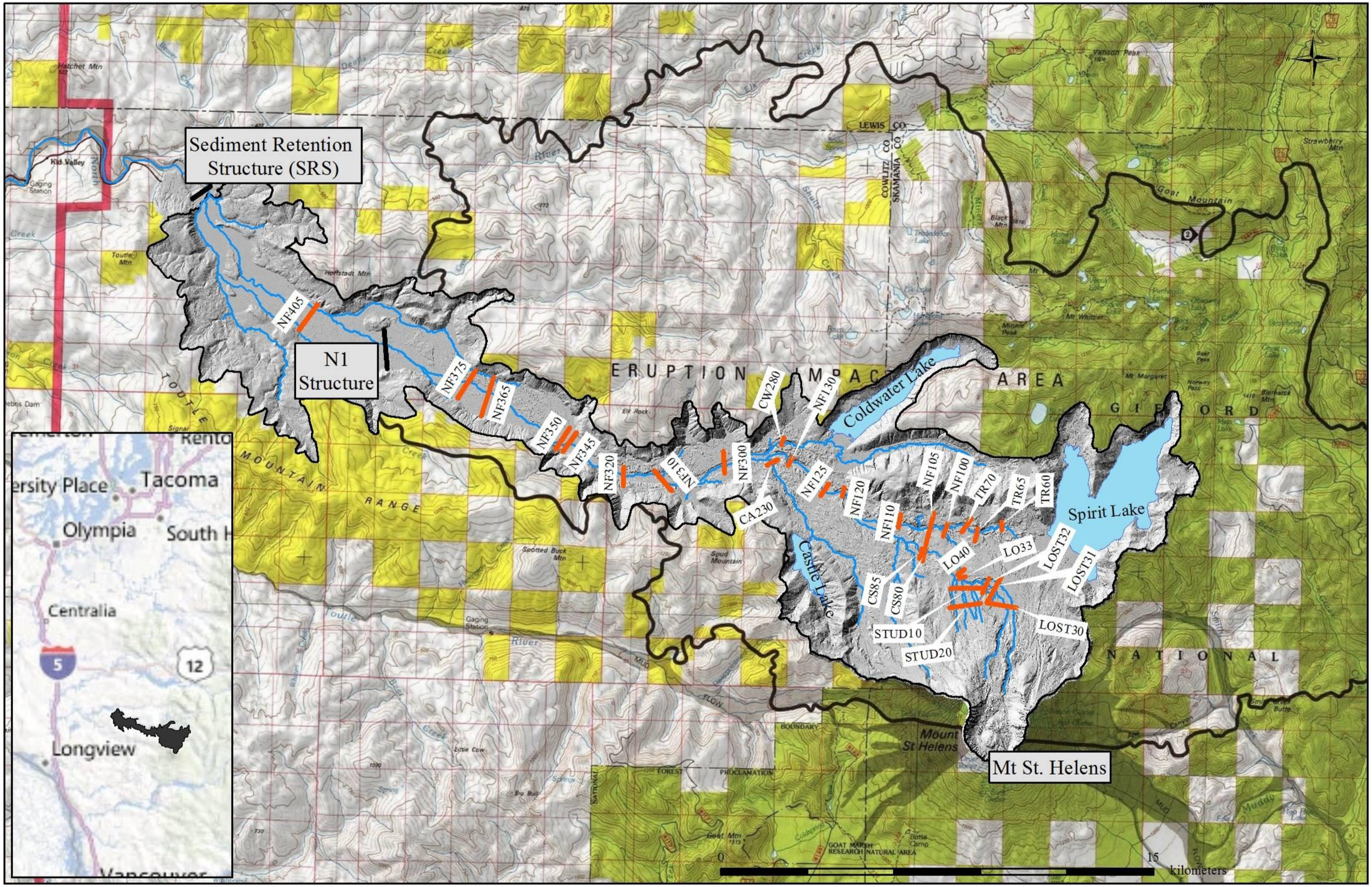

Figure 10. Location map of study area showing 'sites', defined as valley cross-sections, where field data were collected.

5.1 Determining an Appropriate Flow Series for the Upper North Fork Toutle River (UNFT)

The driving force behind any mechanistic analysis of channel erosion must be flow discharge. In this study, flow data were required for two primary purposes: (1) for empirical analyses of sediment transport rates since the 1980 eruptions, and (2) for numerical simulations (BSTEM), of channel adjustments, erosion rates and sediment loadings from channels. Flow data is the primary independent variable for simulation purposes and needed to be expressed as mean-daily data for numerous locations in the UNFT. The starting point for generating a flow series for locations on the debris avalanche was to develop a discharge record at the outlet of the UNFT, considered here to be located at the SRS.

Efforts by the United States Geologic Society (USGS) to maintain gauging stations on the debris avalanche deposit were fraught with difficulties due to highly mobile boundaries. Estimates of flow emanating from the UNFT were made using a straightforward procedure of subtracting the flow rate at the Green River station near Kid Valley (14240800) from the discharge at the NFT, Kid Valley station (14241100). This provided a flow record from March 21, 1981 until the gauges were discontinued at the end of the 1994 water year (September 30, 1994). Data was still available for the Toutle River main stem at Tower Road (14242580) and served as additional source to estimate flows from the UNFT based on comparisons of contributing drainage areas.

Beginning with the 1990 water year (October 1, 1989), mean-daily flows were available from a gauging station installed just downstream of the SRS. These data were used to represent mean-daily flows emanating from the UNFT, except for two periods where the gauge was discontinued (October 1, 1998 – September 30, 2000; October 1, 2002 – September 30, 2006). A comparison of the measured, mean-daily discharge values at the SRS gauge with those calculated using the two Kid Valley stations for overlapping periods of record showed excellent agreement (Figure 11) and were used, therefore, to create a flow series for the period March 21, 1981 to September 30, 1989 for the UNFT. For the two periods of missing data listed above, only discharge data from the Toutle River main stem were available. In cases such as these, discharges are often estimated by multiplying the measured discharge by the ratio of the drainage area of the site in question to the drainage area at the measurement station (14242580). Drainage areas for the UNFT and Tower Road gauge are 453 and 1,284 km^2, respectively; a ratio of 0.353. Flow estimates determined in this fashion were consistently lower than those measured (Figure 12). To improve flow estimates, a relation was developed between the flow rate at the Tower Road gauge and the calculated, percent contribution from the UNFT. Results show a general non-linear trend of decreasing contribution with increasing discharge (Figure 13). Substituting this variable-contribution value (according to the discharge at Tower Road) in place of the constant drainage area ratio provides much improved estimates of flow from the UNFT (Figure 14). This latter method was, therefore, employed for the two missing periods of record in the absence of any measured data. The resulting flow series for the UNFT covering the period March 21, 1981 to September 30, 2010 is shown in Figure 14 along with the data source for the different time periods.

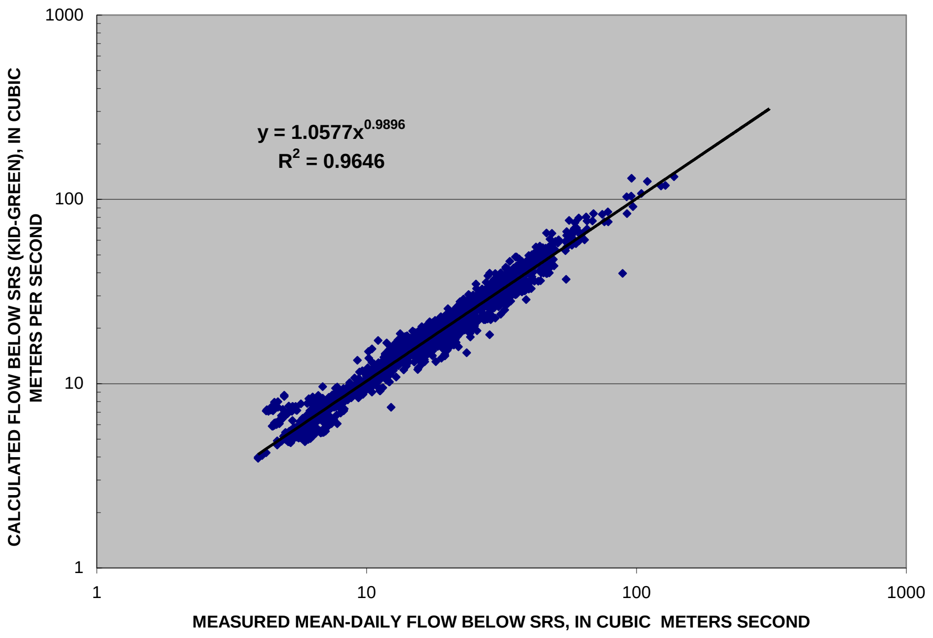

Figure 11. Comparison of mean-daily flows from Upper North Fork Toutle River calculated by subtracting Green River Flows from Kid Valley flows, with discharge measured at the gage just downstream of the SRS.

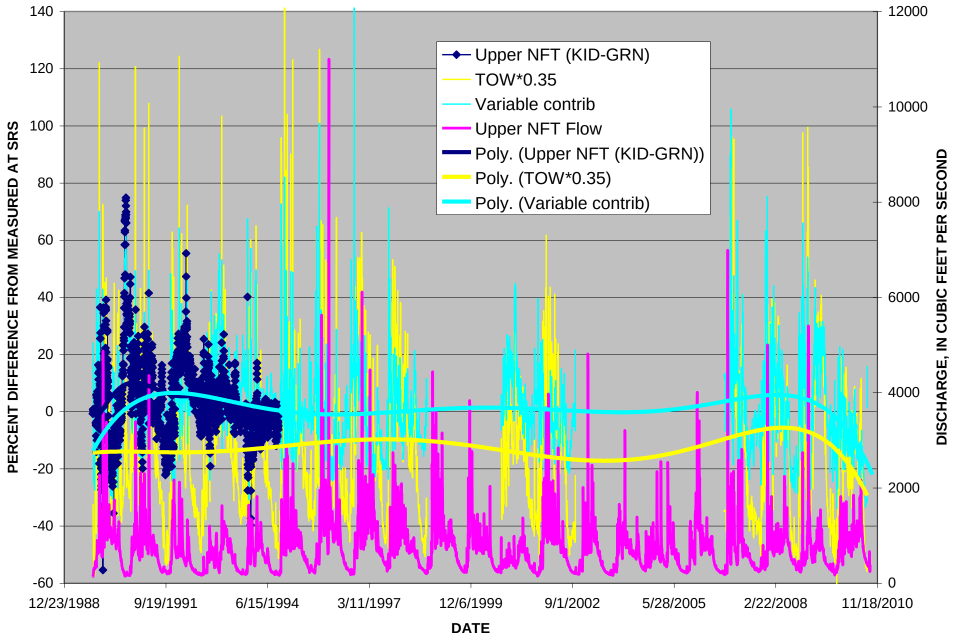

Figure 12. Analysis of methods used to calculate flow at the SRS. Note the variable contribution method (turquoise line) is superior to a standard drainage area comparison (yellow).

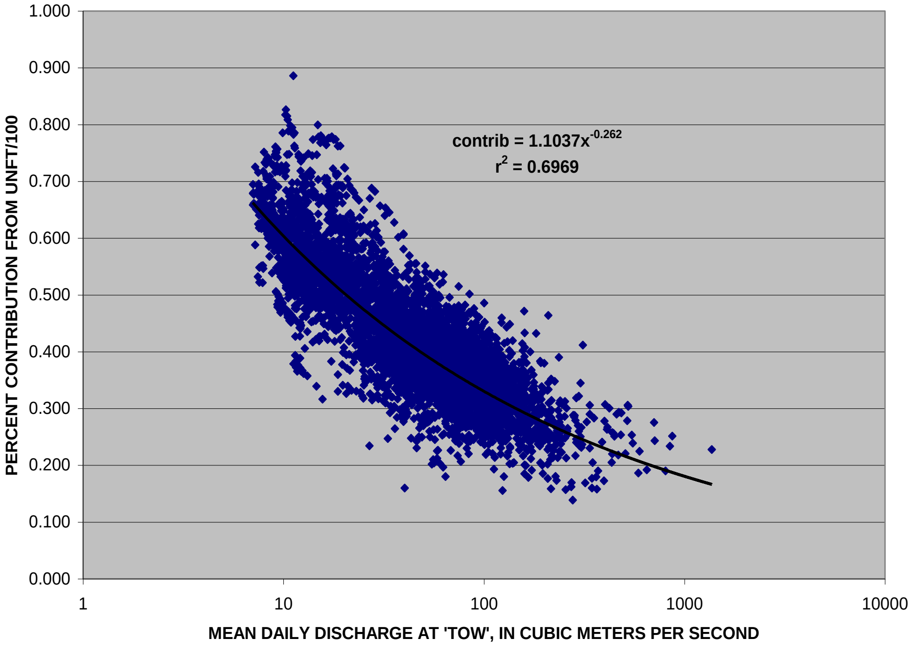

Figure 13. Percent contribution of flow discharge from Upper North Fork Toutle River to flow rate at Toutle River at Tower Road gage.

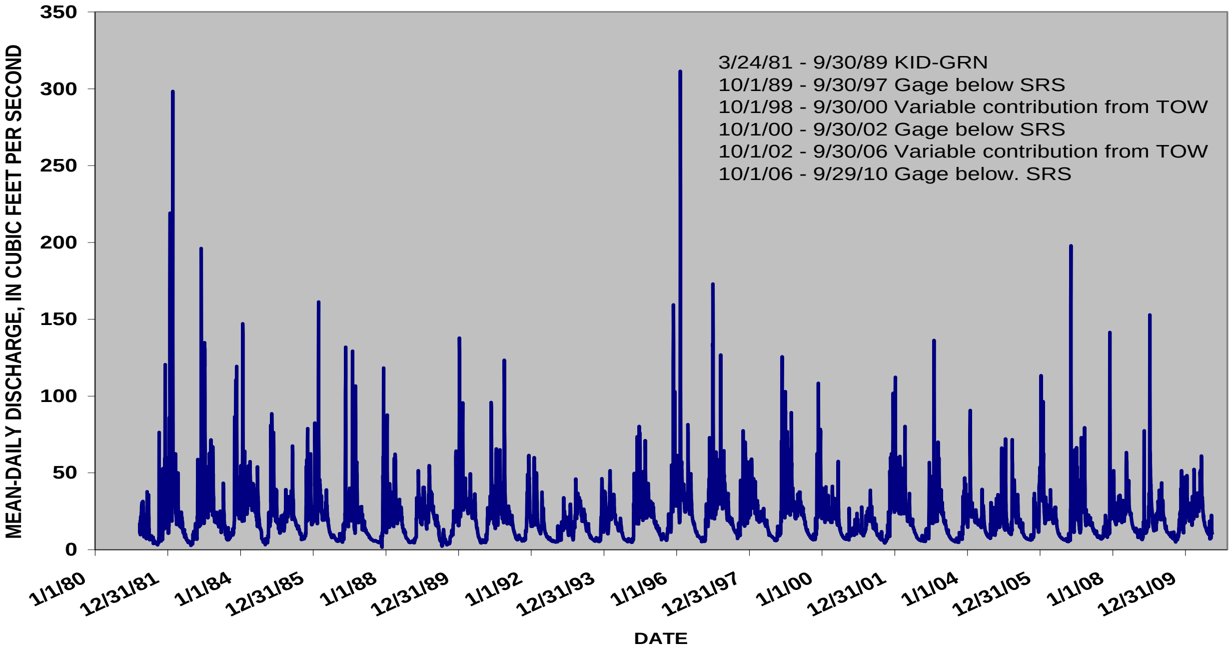

Figure 14. Flow series developed for the UNFT at the SRS. Data is either from the gage located just downstream from the structure, or calculated as indicated from flow at North Fork Toutle River at Kid Valley minus flow at Green River near Kid Valley, or from the variable contributing relation (Figure 13) developed with the gage at Tower Road (TOW) on the Toutle River main stem.

Flow events from the UNFT were generated not only by typical alpine, hydrologic processes such as rainfall events and ‘rain on snow’ events, but also by processes somewhat unique to Mount St. Helens and volcanic landscapes in general. These include lahars and the breakout of debris-dammed ponds and lakes. Most of these latter types of events occurred within the first two years following the May 18, 1980 eruptions (Table 5); with the largest being the breakout from Jackson Lake which occurred on February 20, 1982 during a period of prolonged rainfall (432 mm over 9 days). In combination, this created the second largest post-eruption mean-daily flow, with a discharge of 298 m^3/s. Finally, engineering works such as sediment-retention structures and operations such as pumping from debris-dammed lakes affected UNFT flows. An earthen sediment-retention structure (N-1) constructed on the debris plain breached twice in early 1982. Construction of a large, concrete sediment-retention structure between 1984 and 1986 attenuated flows leaving the UNFT until it filled with sediment in 1995.

Table 5. Important dates and flow events affecting integration and erosion of the debris-avalanche deposit. Modified from Simon (1999).

Date	**Event**	**Estimated volume of water** (10^3 m)
5/18/1980	Eruption	
8/19/1980	Maratta Sink breach	
8/27/1980	Elk Rock Lake breach	310
11/7/1980	Carbonate lake breach	165
7/1/1981	Controlled releases from Coldwater Lake	
10/1/1981	Controlled releases from Castle Lake	
1/24/1982	Breach of ponds on Coldwater Lake levee	379
2/13/1982	Breach of ponds on northern avalanche boundary	710
2/20/1982	Flood	385
2/20/1982	Jackson Lake breach (nr. Elk Rock reach)	2470
2/20/1982	North embankment of N-1 breached	
3/19/1982	Lahar (N-1 breached)	
11/5/1982-1985	Controlled releases from Spirit Lake (about 5 m^3/s)	
12/3/1982	Flood: Complete integration	
3/14/1984	Lahar	
4/1/1985	Flow from Spirit Lake to S. Coldwater Creek	
1984-1986	SRS construction (flows attenuated 1985-1998)	
2/8/1996	Large 'rain on snow' event; peak post-eruption flow	
10/18/2004	Debris flow causes shift of Loowit Creek drainage from Spirit Lake to Step Creek	
11/7/2006	Intense rainfall event avulses Loowit Creek to present course	

The frequency distribution of mean-daily flows shows the typical bell-shaped curve, but with a marked secondary peak centered between 7.2 and 8.4 m^3/s (Figure 15). This reflects the prolonged period of pumping at a rate of about 5 m^3/s from Spirit Lake that was conducted from

November 3, 1982 through 1985 to prevent a catastrophic breaching of the lake. The pumping caused incision through highly erodible, pyroclastic-flow deposits forming a 3 km-long channel (Paine, 1984). Controlled releases from Coldwater and Castle Lakes were conducted for the same reason during July and October, 1981, respectively. The most frequently occurring (modal) flow rate was 22.6 m^3/s which was equaled or exceeded about 36% of the time (Figure 15).

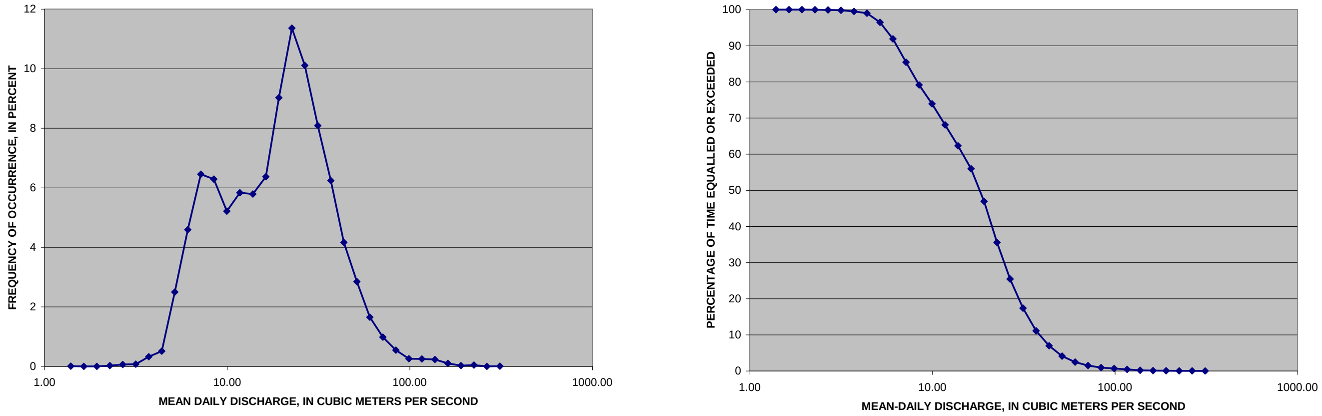

Figure 15. Frequency distribution of mean-daily flows (left), and percentage of time flows are equaled or exceeded (right) for the UNFT.

A summary of the 50 largest mean-daily flows is provided in Table 6. The largest, with a discharge of 318 m^3/s occurred on February 8, 1996 as a result of up to 284 mm of rainfall over five days, combined with about 102 mm of equivalent snow melt. This flow will be referred to later in this report as ‘the 1996 event’ and is one of the storms used as a metric for evaluating erosion trends in the UNFT. Aside from the 1996 event (February 7-9, 1996) and the February 20th 1982 lake breakout event, other important flow events include January 24, 1982 (219 m^3/s; breakout of ponds) and a rare rainfall event culminating on November 7, 2006 (566 mm of rain over 5 days without snow cover) that produced a peak, mean-daily flow of 198 m^3/s. This latter event, hereafter referred to as ‘the 2006 event’ caused considerable amounts of erosion, particularly in the Loowit Creek and Step Creek sub-drainages, and will be discussed in greater detail later.

The mean-daily flow series produced for the UNFT at the SRS (Figure 14) was used to generate flow series’ for modeling purposes at various locations of the UNFT using a drainage area ratio:

$$Q_x = Q_{SRS} * (DA_x / DA_{SRS}) \tag{25}$$

where, Q = discharge, in m^3/s; $_x$ = denotes a specific location; $_{SRS}$ = denotes at sediment retention structure; DA = drainage area in km^2.

Although drainage from the UNFT was fully integrated by November 1982, total contributing drainage area to the UNFT main-stem went through minor changes due to the avulsions of Loowit and Step Creeks described above. Using data provided by the U.S. Army Corps of Engineers derived from Light Detection And Ranging (LiDAR) it was possible to estimate 2009 drainage basin areas for all sites in the UNFT, these values are provided in Table 7. Areas are also provided for several time periods of interest; 1980 – 1984, 1984 – 2004, 2004 – 2006 and 2006 – present (2009). These time periods were chosen through communication with the USGS. From 1980 to 1984 all channels flowed through to the SRS. In 1984 a lahar diverted the Loowit channel to Spirit Lake. By 2004 Loowit had incised enough to capture Step and flow to the SRS again. In 2006 another debris jam caused Loowit to avulse and both Loowit and Step now flow separately to the SRS, and therefore have the same drainage areas as pre-1984.

Table 6. List of the 50 largest mean-daily flows from the Upper North Fork Toutle River (UNFT).

Rank	**Date**	**Q in m^3/s**	**Rank**	**Date**	**Q in m^3/s**
1	2/8/96	311	**26**	2/14/82	134
2	2/20/82	298	**27**	12/1/95	133
3	1/24/82	219	**28**	11/24/86	132
4	2/9/96	219	**29**	12/31/96	132
5	11/7/06	198	**30**	1/8/83	131
6	12/3/82	196	**31**	2/15/82	131
7	2/7/96	194	**32**	2/17/82	131
8	2/16/82	173	**33**	12/4/82	130
9	1/1/97	173	**34**	2/1/87	129
10	1/23/82	167	**35**	1/11/90	128
11	2/24/86	161	**36**	3/19/97	127
12	11/30/95	159	**37**	11/26/98	126
13	11/6/06	159	**38**	12/16/82	125
14	1/8/09	153	**39**	1/7/09	125
15	1/24/84	147	**40**	4/6/91	123
16	11/29/95	144	**41**	11/28/95	122
17	12/3/07	142	**42**	12/5/81	121
18	1/25/84	140	**43**	1/7/83	120
19	2/21/82	138	**44**	11/24/83	119
20	1/2/97	138	**45**	12/10/87	118
21	1/10/90	138	**46**	1/6/83	117
22	1/31/03	136	**47**	1/11/06	113
23	2/18/82	136	**48**	12/4/07	113
24	1/5/83	135	**49**	11/23/86	113
25	12/30/96	134	**50**	1/8/02	112

Table 7. Contributing drainage area of sites along the UNFT. *Present drainage area is calculated from 2009 LiDAR data provided by the U.S. Army Corps of Engineers.

Site	**Channel**	**Present drainage area* (km^2) minus Spirit Lake**	**Drainage area (km^2) 1980 - 1984 2006 - Present**	**Drainage area (km^2) 2004 - 2006**	**Drainage area (km^2) 1984 - 2004**
SRS	NF Toutle	324.91	372.74	372.74	369.39
NF435	NF Toutle	276.23	324.06	324.06	320.71
NF420	NF Toutle	273.44	321.28	321.28	317.93
NF405	NF Toutle	269.43	317.27	317.27	313.92
NF400	NF Toutle	265.01	312.85	312.85	309.50
NF375	NF Toutle	173.72	221.55	221.55	218.21
NF365	NF Toutle	171.02	218.86	218.86	215.51
NF360	NF Toutle	170.50	218.33	218.33	214.98
NF350	NF Toutle	165.04	212.87	212.87	209.52
NF345	NF Toutle	162.30	210.13	210.13	206.78
NF320	NF Toutle	151.36	199.19	199.19	195.84
NF310	NF Toutle	144.76	192.59	192.59	189.24
NF305	NF Toutle	130.73	178.57	178.57	175.22
NF300	NF Toutle	124.28	172.12	172.12	168.77

Site	Channel	Present drainage area* (km^2) minus Spirit Lake	Drainage area (km^2) 1980 - 1984 2006 - Present	Drainage area (km^2) 2004 - 2006	Drainage area (km^2) 1984 - 2004
NF300-Confl	NF Toutle	121.64	169.48	169.48	166.13
CW280	Coldwater	46.40	46.40	46.40	46.40
CW245	Coldwater	46.12	46.12	46.12	46.12
CW255	Coldwater	45.86	45.86	45.86	45.86
CA230	Castle	21.93	21.93	21.93	21.93
CA225	Castle	20.38	20.38	20.38	20.38
CA220	Castle	18.92	18.92	18.92	18.92
CA200	Castle	7.72	7.72	7.72	7.72
NF130	NF Toutle	42.55	90.38	90.38	87.03
NF125	NF Toutle	40.06	87.89	87.89	84.54
NF120	NF Toutle	39.43	87.26	87.26	83.92
NF117	NF Toutle	37.38	85.22	85.22	81.87
NF110	NF Toutle	22.20	70.03	70.03	66.68
NF105	NF Toutle	18.97	66.80	66.80	63.45
TR100	Truman	5.50	53.33	53.33	53.33
TR70	Truman	5.30	53.14	53.14	53.14
TR65	Truman	4.05	51.88	51.88	51.88
TR60	Truman	3.33	51.17	51.17	51.17
LO100	Loowit	12.71	12.71	12.71	9.36
LO40	Loowit	11.25	11.25	11.25	7.91
LO33	Loowit	11.07	11.07	11.07	7.72
LO32	Loowit	3.63	3.63	0.28	0.28
LO31	Loowit	3.55	3.55	0.20	0.20
LO30	Loowit	3.35	3.35	3.35	To Spirit L.
Step32	Step Creek	5.35	5.35	8.70	5.35
Step31	Step Creek	4.19	4.19	7.54	4.19
Step30	Step Creek	3.55	3.55	3.55	3.55
CS1	Carbonate Springs	-	13.97	13.97	13.97
CS2	Carbonate Springs	-	13.65	13.65	13.65
CS3	Carbonate Springs	-	13.23	13.23	13.23
CS4	Carbonate Springs	-	12.63	12.63	12.63
CS5	Carbonate Springs	-	3.55	3.55	3.55
CS6	Carbonate Springs	-	3.47	3.47	3.47
CS7	Carbonate Springs	-	2.81	2.81	2.81
CS8	Carbonate Springs	-	2.55	2.55	2.55
Studa1	Studabaker	-	6.13	6.13	6.13
Studa2	Studabaker	-	5.39	5.39	5.39
Studa3	Studabaker	-	4.47	4.47	4.47
Studa4	Studabaker	-	3.20	3.20	3.20
Glacier1	Glacier	-	2.70	2.70	2.70
Glacier2	Glacier	-	2.29	2.29	2.29
Glacier4	Glacier	-	2.02	2.02	2.02
Glacier5	Glacier	-	1.96	1.96	1.96
Glacier6	Glacier	-	1.84	1.84	1.84
Glacier7	Glacier	-	1.50	1.50	1.50
Glacier8	Glacier	-	1.23	1.23	1.23
Glacier9	Glacier	-	0.89	0.89	0.89

6. METHODS OF EMPRICAL ANALYSIS OF PAST, PRESENT AND FUTURE EROSION RATES

The most straightforward and fundamental means of determining changes in channel geometry and, therefore, erosion rates are to compare measured cross-sectional surveys. Following the catastrophic eruption of Mount St Helens on May 18, 1980, the U.S. Geological Survey established a network of monumented cross sections along the stream systems draining the mountain. The network of cross sections in the UNFT basin is shown in (Figure 16). The first surveys were conducted along the UNFT in 1980 at NF120, NF300, NF320 and NF375. At least one survey was conducted at most of the stations annually, with multiple surveys conducted during some years to document changes in channel geometry following large storm events, lahars, or pumping from the various debris-dammed lakes. Changes in channel geometry from 1980-1985 are summarized in a pair of USGS publications (Meyer *et al.*, 1986; Meyer and Dodge, 1988). Simon (1999) provided a summary of channel changes throughout the Toutle River Basin from 1980 to 1992. The frequency of cross-section surveys decreased with time through 1992. No surveys were conducted during 1993-1995 and only three sections were surveyed between 1996 and 1997 (Table 8). A relatively complete set of surveys was made in 1998 but again only sporadic surveys were available between 1998 and the set that was completed as part of this study during 2009 and 2010. Fortunately, however, digital elevation models (DEMs) derived from Light Detection And Ranging (LiDAR) and Digital Orthophoto Quadrangles (DOQs) were available to fill in these gaps.

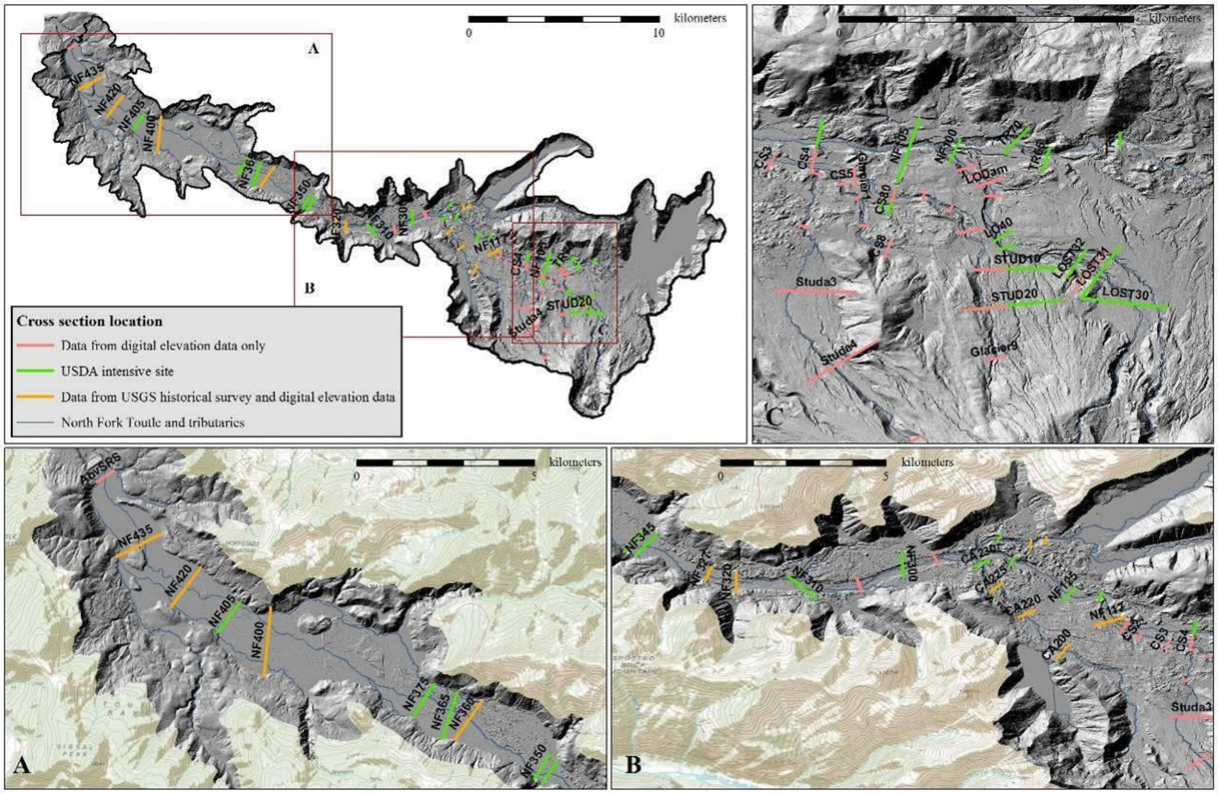

Figure 16. Map showing locations of cross sections used in this study to determine time-series thalweg elevations, erosion areas by bed and bank processes and erosion volumes for the UNFT.

Table 8. Summary of available cross-sectional surveys conducted by the USGS (X) and USDA-ARS (X), 1980 – 2010. No surveys were conducted between 1993 and 1995, and between 2000 and 2003.

Location and Cross-Section	1980	1981	1982	1983	1984	1985	1986	1987	1988	1989	1990	1991	1992	1996	1997	1998	1999	2004	2005	2006	2007	2008	2009	2010
Carbonate Springs																								
80		X	X	X	X	X	X	X									X						X	
85		X	X	X	X								X				X						X	
Castle Creek																								
230																								X
Coldwater																								
280		X	X		X	X	X	X	X	X	X													X
Loowit																								
30			X	X	X	X	X	X					X		X			X			X		X	
31																							X	
32																							X	
33		X	X	X	X								X						X		X		X	
40		X	X	X	X	X	X	X					X	X					X		X		X	
NF Toutle River																								
100			X	X	X	X	X	X	X	X	X					X			X		X		X	
105				X	X																		X	
110				X	X											X				X	X		X	
120	X			X	X	X	X	X	X	X	X	X	X		X						X		X	
125		X						X	X		X					X								X
130		X	X	X	X	X	X	X	X	X	X		X			X					X			X
300	X			X	X	X	X	X	X	X	X					X				X			X	
310		X	X	X	X	X	X	X	X	X	X		X				X						X	
320	X	X	X	X	X	X	X	X	X	X	X	X	X			X					X?		X	
345		X	X	X	X	X	X	X	X	X	X		X				X						X	
350		X	X	X	X		X						X			X				X				X
365		X	X	X																				X
375	X	X	X	X	X	X	X	X	X	X	X						X							X
405				X	X																			X
Truman																								
60			X	X	X	X	X	X	X	X	X					X							X	
65			X	X	X	X	X	X	X	X	X	X	X										X	
70			X	X	X	X	X	X				X	X				X						X	
Step																								
31																								X
32																								X
Studabaker																								
10																								X
20																								X

The U.S. Army Corps of Engineers, Portland District provided a number of terrain surfaces for the UNFT. These were of varying aerial extent, grid size and resolution (Figure 17 and Table 9). DEMs were used for the years: 1980, 1987, 1999, 2003, 2006, 2007 and 2009. All the DEMs started at or below the SRS except for the 1980 surface which started just below NF400. The 1980 surface was extrapolated with a 5 meter grid from the post eruption USGS 7.5 minute quadrangles with 40 ft contour interval. These maps were most likely created from aerial photos taken in 1980 and then field checked in 1981. The 1987 and 1999 DEMs were derived from photogrammetric analysis of aerial photos. The 2003, 2006, 2007, and 2009 DEMs were created from aerial based LiDAR collected points. The 2003 DEM exhibited the worst vertical error believed to be due to re-sampling that occurred during the surface creation. Transects generated from the 2003 surface showed considerable amounts of smoothing as if a spline curve had been applied to the entire dataset. In some areas, the profiles compared well to ground surveys while in others, the differences appeared exaggerated. Transects generated from the other DEMs showed excellent agreement when compared to ground surveys taken at about the same time.

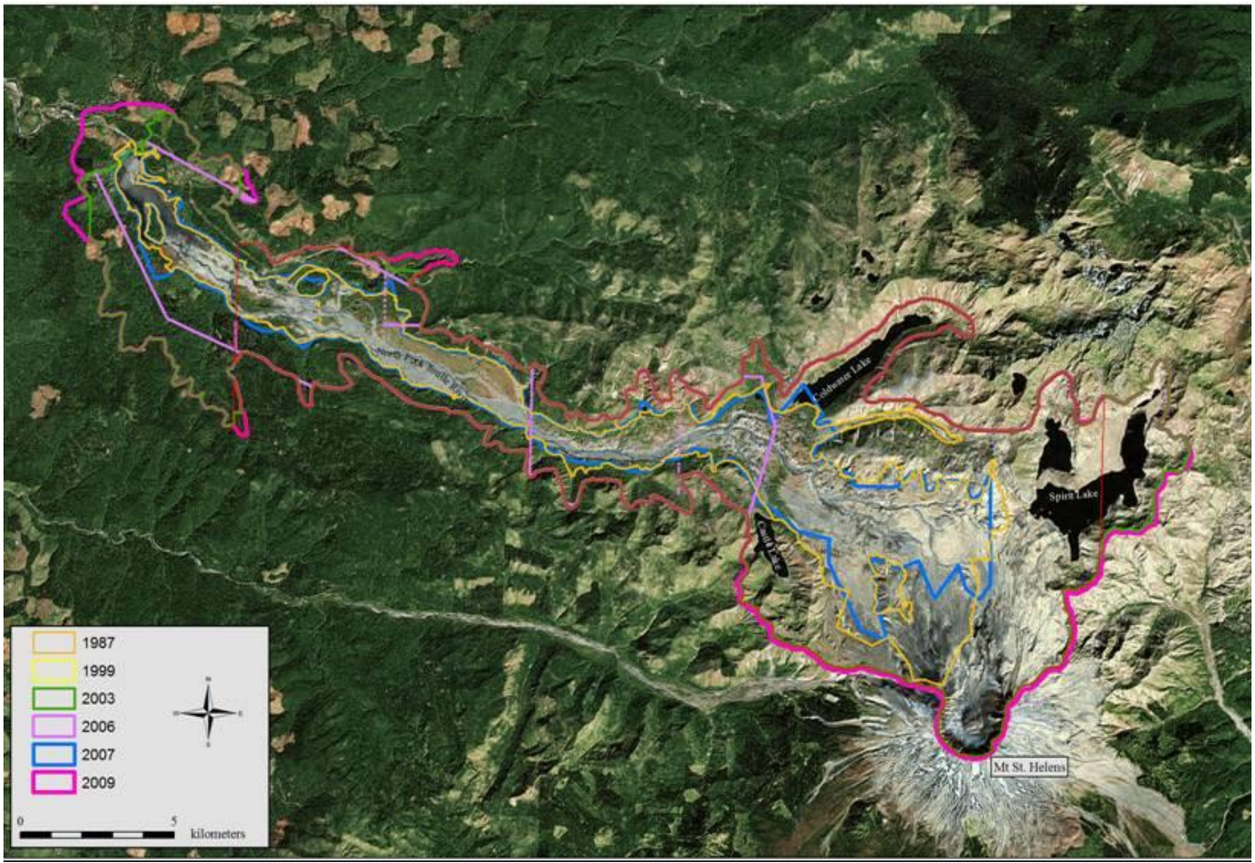

Figure 17. Extent of raster data used to determine changes in channel geometry for locations and periods where no ground survey existed.

To empirically determine trends of net erosion of the UNFT, the two data sets (ground surveys and DEMs) were used in combination to analyze how specific cross sections changed with time. Time-series channel geometries for a given cross-section location were overlain for successive time periods to identify changes over the period between surveys. Four types of metrics were used to understand how the UNFT had evolved with time since 1980, and to determine trends in net erosion that could then be extrapolated into the future. The metrics were: 1) thalweg elevation, 2) net bed erosion, 3) net bank erosion and 4) net total erosion. The rationale for separating out total erosion into its component parts was to be able to test the hypothesis spelled out in the research proposal that the dominant source of sediment in the UNFT was lateral erosion of streambanks, terraces and hummocks on the debris avalanche deposit, and that the rate of erosion was decreasing non-linearly with time.

Table 9. Digital elevation models provided by the Portland District, USACE.

Date used for calculation	Dates flown	Collection method	Grid size
September 18, 2009	September 16-20, 2009	Aerial LiDAR	1 meter
October 25, 2007	October 22-27, 2007	Aerial LiDAR	1 meter
October 21, 2006	October 21, 2006	Aerial LiDAR	1 meter
October 1, 2003	September 19 - October 2, 2003	Aerial LiDAR	5 meters
October 1, 1999	Unknown	Aerial Photography	3 meters
June 6, 1987	April 27, June 6 & 11, 1987	Aerial Photography	3 meters
May 18, 1980	1980	7.5-minute USGS Topographic Quad	5 meters

6.1 Thalweg Elevations – Incision and Aggradation

Thalweg elevation was noted for each survey, so as to develop a concise picture of vertical adjustment over time and space, and to test whether non-linear trends of bed-level change with time were applicable, as documented in Simon (1992; 1999). In addition, this analysis provided a means of determining incision magnitudes along the UNFT for individual events and over the 30-year adjustment period (1980-2010). Trends in thalweg elevation were fit to power functions of the form (Simon, 1994 and Figure 18):

$$E = a\,t^{b} \qquad (26)$$

where E = elevation of the channel bed, in meters; a = regression, determined by regression representing the initial elevation of the channel bed, in meters; t = time since emplacement of the debris-avalanche deposit, in years where t_0 represents May 18, 1980 = 1.0; and b = exponent, determined by regression and representing the non-linear rate of change of bed elevation with time.

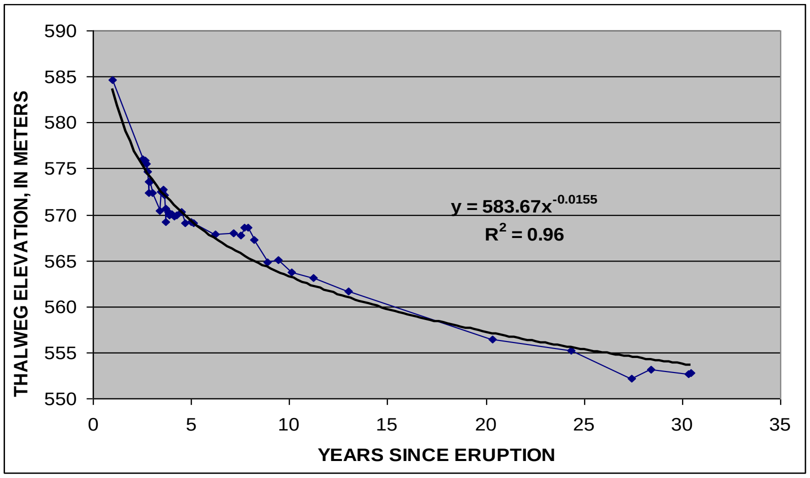

Figure 18. Thalweg elevation at NF310 showing more than 30 m of incision and demonstrating the use of a power function to fit trends of thalweg elevation along the UNFT.

In cases where more than one non-linear trend was observed from the data, multiple non-linear regressions of thalweg change with time were developed using years other than 1980 as t_0. The existence of multiple non-linear trends were ascribed to one or more of the following causes:

1. A secondary trend of aggradation following initial adjustment by incision (Figure 19). This has been identified in many disturbed fluvial systems as the excess sediment-transport capacity and boundary shear stress of the flow is reduced with time through incision (reduction in slope) and widening (reduction in pressure head and increase in relative roughness) (Simon, 1992). Sediment delivered to this hypothetical cross section or reach then does not have sufficient sediment-transport capacity to transport the enhanced loadings generated from eroding reaches upstream; and

2. Accelerated rates of incision due to pumping for extended periods (months to years) from debris-dammed lakes and at discharge magnitudes and durations atypical for the site (Figures 20 and 21). A good example of this is the emergency pumping from Spirit Lake into the Truman channel at a rate of about 5 m^3/s (Paine, 1984).

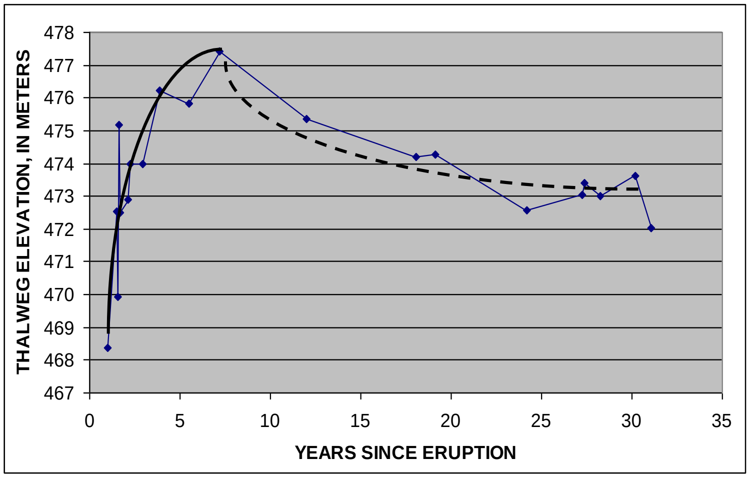

Figure 19. Example of secondary aggradation trend following incision at NF350.

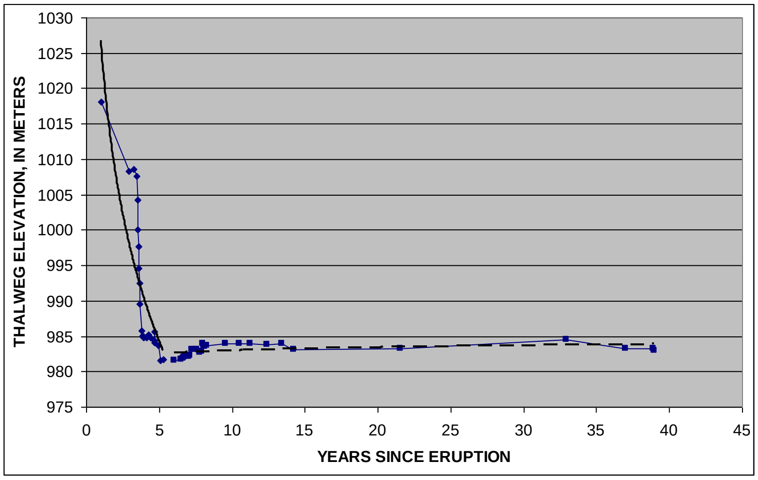

Figure 20. Example of atypical accelerated incision at TR65 due to pumping from Spirit Lake between 1982 and 1985, and subsequent secondary adjustment.

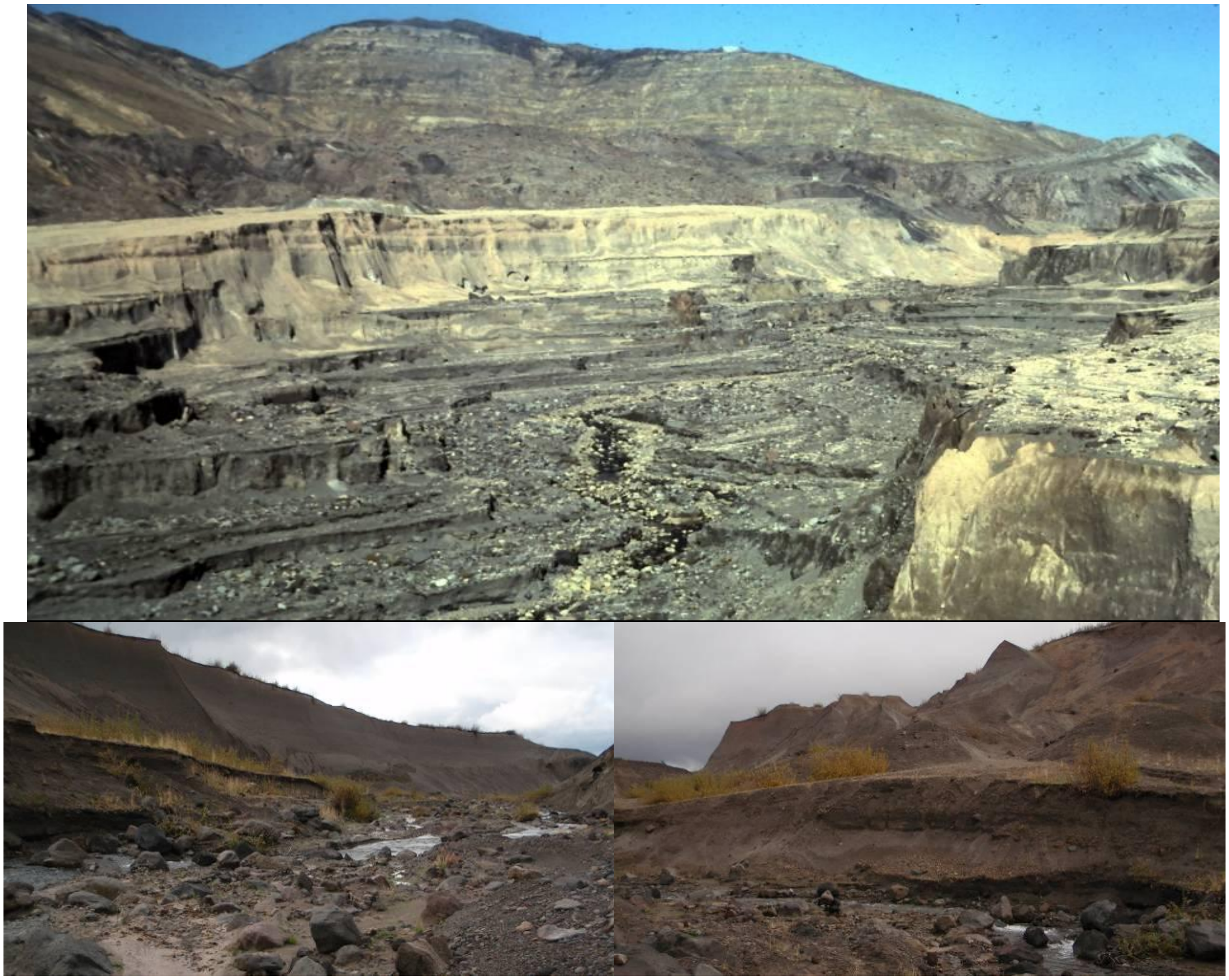

Figure 21. TOP: Photograph of accelerated channel incision by mid-1980's at TR65 by Colin Thorne. BOTTOM: In-channel TR65 2009 USDA-ARS, NSL photographs, left and right bank respectively.

Exponent *b*-values obtained by non-linear regression of Equation 26 and plotted against river kilometer, were used to develop an empirical model of bed-level adjustment for the UNFT. Models like this have been developed and proved robust in diverse fluvial environment such the Mid South (Simon 1989; 1992; 1994), the Midwest (Simon and Rinaldi, 2000); the Arno River, Tuscany, Italy (Rinaldi and Simon, 1998) and the Toutle River System (Simon 1992; 1999).

6.2 Eroded Areas at Monumented Cross-Section Locations

For each cross-section location, successive surveys were overlain starting with either the first survey or the 1980 DEM. Sub-areas representing either erosion or deposition during the time period encompassing the overlain surveys were identified and digitized. Each of these sub areas were then classified as either bed or bank erosion/deposition (Figure 22) and summed for each category, producing a value for net erosion/deposition (in square meters) for both the bed and the banks over the time period. Summing the eroded areas for bed and banks then provided net values for total erosion or deposition for that time period. This was done for all survey pairs through to the 2009-2010 ground surveys conducted by the ARS. Cumulative values (through

2010) were calculated for the bed, bank and total-erosion volumes. Each of these calculated areas was then plotted against time in years (on the x-axis) to identify trends of erosion and deposition for each cross section between 1980 and 2010 (Figure 23). The data contained in the cumulative erosion plots for each cross section (such as Figure 24) were fit to non-linear functions to be used to extrapolate erosion amounts and rates at each site into the future. An example from NF 300 is shown in Figure 22.

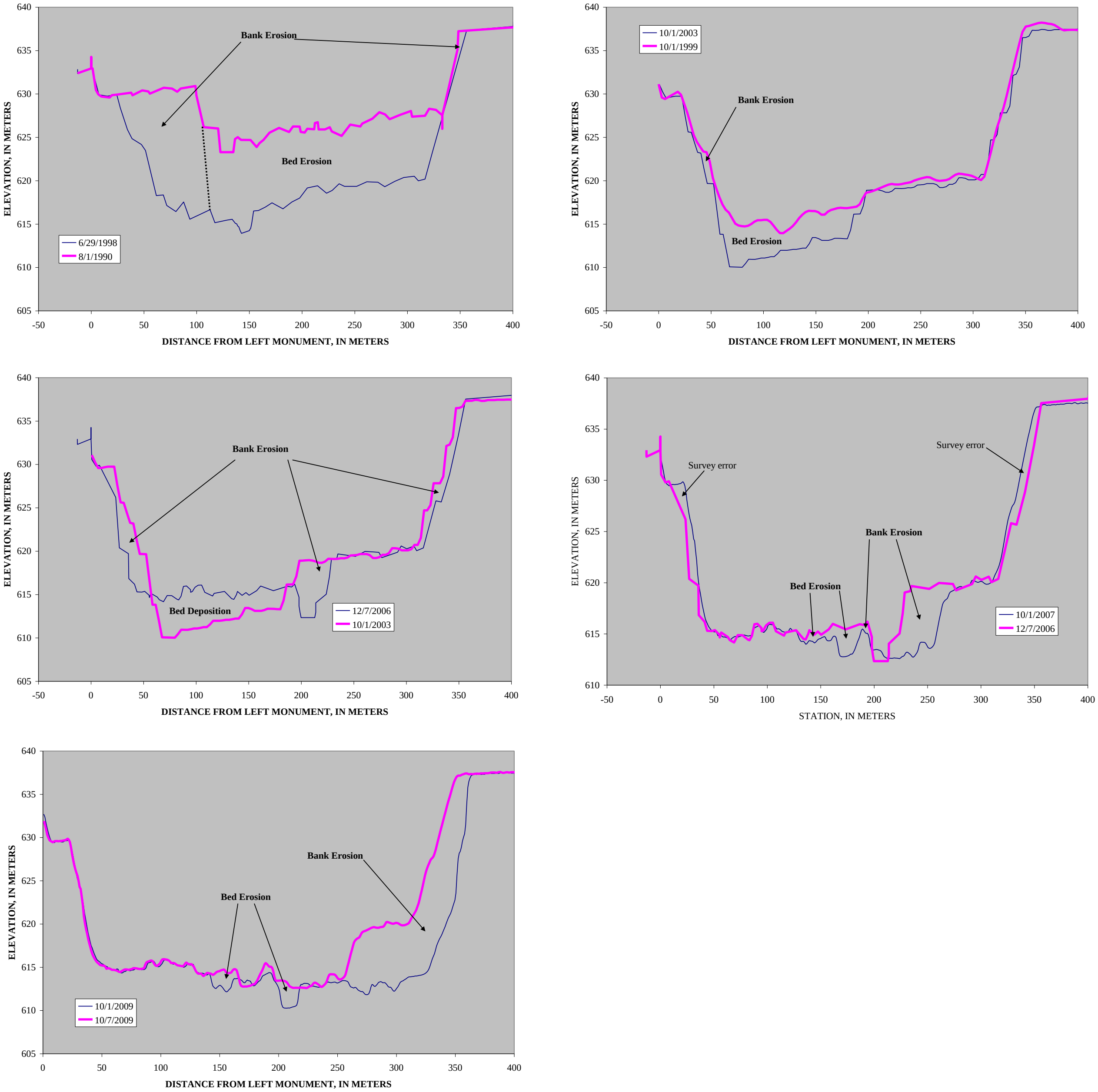

Figure 22. Examples of overlain, successive cross-section surveys (NF300) showing how changes in area due to bed and bank processes were obtained for each paired time-series survey.

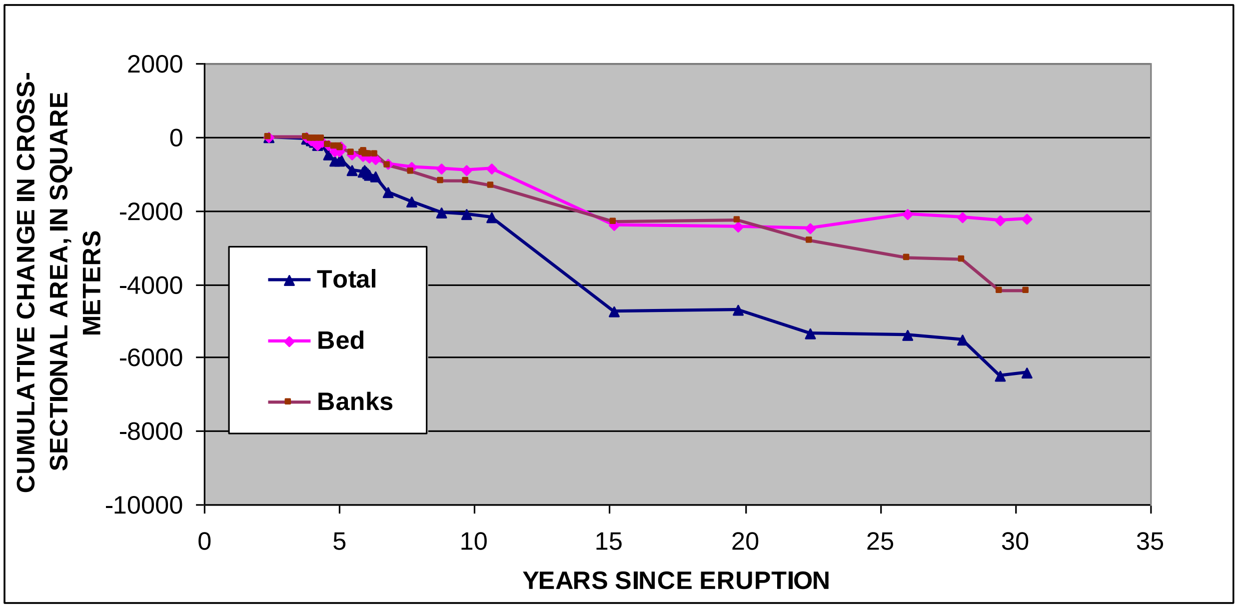

Figure 23. Example of results of calculations of cumulative erosion for a site (NF300). Cumulative amounts of bed, bank and total erosion (in m^2) display the typical non-linear decay in erosion rates. Note: negative values represent erosion.

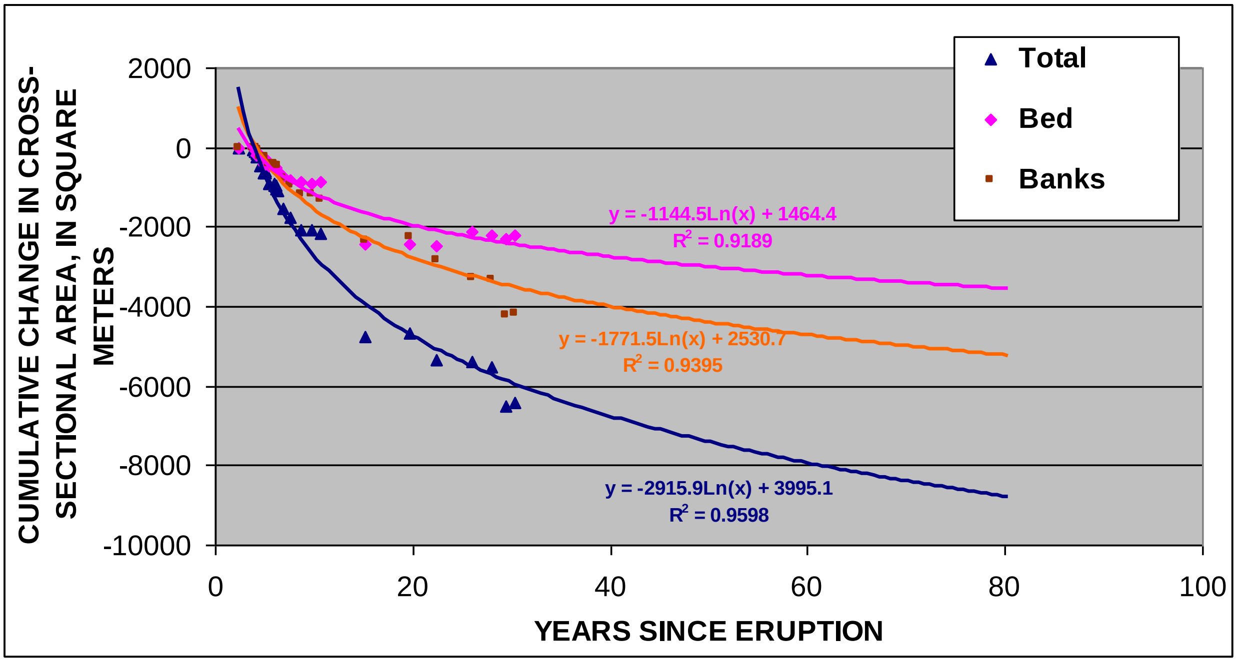

Figure 24. Example from NF300 of how data on cumulative eroded areas were used to develop non-linear regressions for use in temporally extrapolating erosion amounts and rates into the future. Note: negative values represent erosion.

6.3 Eroded Volumes from Reaches Bounded by Monumented Cross-Sections

The method described in the previous section and shown in Figure 22 provides a means of extrapolating erosion rates into the future at each of the surveyed sites by solving each of the regression equations for various times in the future. To obtain erosion volumes as of 2010 from erosion-area data calculated at each cross-section, results in square meters needed to be averaged between sites and then multiplied by the distance of the reach bounded by two adjacent sites. Sites were added between historical cross sections, where needed, for better spatial resolution. Data for these sites came similarly from a combination of historical surveys by the USGS and the DEMs provided by the U.S. Army Corps of Engineers, Portland District. A list of the sites used in the analysis and their pairing with an adjacent site are shown in Table 10. This analysis provides total, net erosion volumes from 1980-2010 as well as individually for the bed and banks. However, to make the results from this study comparable to those conducted by others (West Consultants, 2002; Biedenharn, 2010), and in accordance with directions from the Portland District, the downstream limit of sites included in the temporal extrapolation of erosion volumes, is N-1 (bold in Table 10).

Whereas eroded areas for adjacent sites were averaged and then multiplied by the distance been the sites to obtain total erosion volumes between 1980 and 2010, temporal extrapolation of eroded volumes needed to rely on the regressions developed at each cross section (ie. Figure 25). Because of this, prediction of erosion volumes into the future was conducted using a somewhat different procedure due to the uncertainty in averaging regression coefficients between adjacent sites. Here, the regression equations for the bed and banks at each site were solved individually for a range of years since the eruption (Figure 25). The regressions were solved annually for years 1-55 (1980-2035) to provide good resolution by which to compare results with those of West Consultants (2002) and Biedenharn (2010). Additionally, they were solved for post-eruption years 70, 90, 110 and 130 to bring the temporal extrapolation to 2110, 100 years from present as stipulated in the research objectives. Calculated erosion-area values for each cross section and post-eruption year (stated above) were summed and then multiplied by the reach length between the paired cross sections (Table 10) to obtain the cumulative eroded volume for the reach for that year. A slightly different approach was used for some of the tributary channels because of poor spatial or temporal resolution of ground surveys. Thus, for South Fork Coldwater Creek, upper and lower Carbonate Springs, un-named tributaries to Loowit channel, upper Glacier and Studebaker Creeks, regressions were created for total erosion areas only from the DEMs. These were then solved for the same range of years and multiplied by the length of the channel to obtain erosion volumes. Values for all reaches for a given year were then summed to obtain a total erosion volume for each stipulated post-eruption year. Deposition was accounted for in this procedure during summing of all reach values as deposition volumes had a positive sign while erosion had a negative sign.

Table 10. Locations of all cross sections used in analysis of eroded volumes. Paired sections used for interpolation of erosion rates are represented by the cross-section names in the first and last columns. Site N-1 is bold, denoting the downstream limit of sites used for temporal extrapolation.

Site	Distance to SRS (km)	Distance to North Fork Toutle (km)	Distance from last site (km)	Last site
SRS	0.87	-	0.87	-
NF435	4.08	-	3.21	SRS
NF420	7.03	-	2.95	NF435
NF405	9.37	-	2.35	NF420
NF400	10.79	-	1.41	NF405
N-1	**15.57**	**-**	**4.78**	**NF400**
NF375	17.52	-	1.95	N-1
NF365	18.56	-	1.04	NF375
NF360	19.36	-	0.80	NF365
NF350	22.68	-	3.32	NF360
NF345	23.18	-	0.50	NF350
NF320	26.26	-	0.87	NF327
NF310	28.21	-	1.95	NF320
NF305	29.95	-	1.74	NF310
NF300	31.38	-	1.44	NF305-LiDAR
NF300-Confl	32.39	-	1.00	NF300
CW280	34.37	1.90	2.99	NF300
CW245	35.33	2.86	0.96	CW280
CW255	35.87	3.40	0.54	CW245
CA230	33.72	0.34	2.34	NF300
CA225	34.70	1.32	0.98	CA230
CA220	36.15	2.76	1.45	CA225
CA200	38.07	4.69	1.93	CA220
NF130	34.66	-	2.27	NF300-Confl
NF125	36.72	-	2.06	NF130
NF120	37.62	-	0.91	NF125
NF117	38.62	-	1.00	NF120
NF110	40.83	-	2.21	NF117
NF105	42.24	-	1.41	NF110
TR100	43.04	0.36	0.79	NF105
TR70	43.94	1.26	0.90	TR100
TR65	44.50	1.82	0.56	TR70
TR60	45.69	3.02	1.19	TR65
LO100	42.94	-	0.70	NF105
LO40	44.92	-	1.19	LODam
LO33	45.15	-	0.22	LO40
LO32	46.46	-	1.31	LO33
LO31	46.85	-	0.11	LO31Alt
LO30	48.02	-	1.17	LO31
Step32	46.33	0.24	1.18	LO33
Step31	46.70	0.61	0.12	Step31Alt
Step30	47.54	1.45	0.84	Step31
CS1	39.00	0.12	0.38	NF117
CS2	39.53	0.64	0.52	CS1
CS3	40.33	1.45	0.80	CS2

CS4	40.92	2.03	0.59	CS3
CS5	41.53	2.64	0.61	CS4
CS6	41.94	3.06	0.42	CS5
CS7	42.56	3.68	0.62	CS6
CS8	43.26	4.38	0.70	CS7
Studa1	41.10	2.22	0.18	CS4
Studa2	42.21	3.33	1.11	Studa1
Studa3	43.62	4.74	1.41	Studa2
Studa4	45.22	6.34	1.60	Studa3
Glacier1	41.60	2.72	0.69	CS4
Glacier2	42.18	3.29	0.57	Glacier1
Glacier4	42.68	3.80	0.51	Glacier2
Glacier5	43.08	4.19	0.40	Glacier4
Glacier6	43.56	4.68	0.49	Glacier5
Glacier7	44.33	5.45	0.77	Glacier6
Glacier8	45.03	6.15	0.70	Glacier7
Glacier9	45.92	7.03	0.89	Glacier8

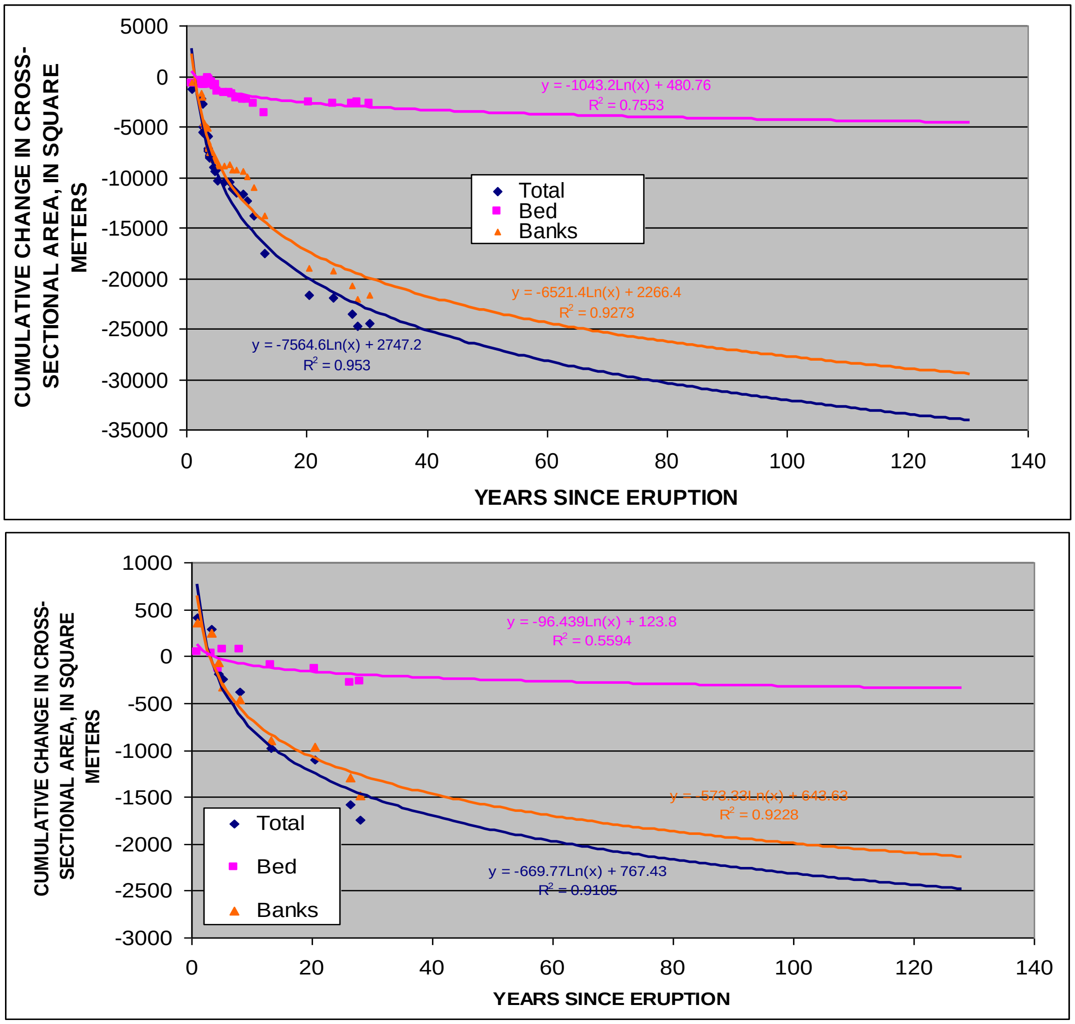

Figure 25. Examples of extrapolating 130 years from the eruption (2110) of regression equations for bed, banks and total erosion from NF310 (top) and LO33 (bottom). Note: (1) the predominance of streambank erosion relative to bed erosion at both sites, and (2) vastly different erosion volumes between the two sites.

7. RESULTS OF EMPRICAL ANALYSIS OF PAST, PRESENT AND FUTURE EROSION RATES

Development of a new drainage network on the debris avalanche deposit following the major eruption of May 18, 1980 occurred initially by the "filling and spilling" of depressions through December of 1982 (Simon, 1999) (Figure 26). Incision into debris avalanche and pyroclastic materials represented the initial fluvial-erosion process, channeling water between these depressions and extending upstream by headcutting. Even after December 1982, contributing drainage areas were not static, however, as channel avulsions caused by subsequent lahars and significant flow events caused channels to capture drainage areas from adjacent drainages. Loowit channel for example has shifted course numerous times, draining initially to Spirit Lake and then avulsing to the west onto the Step Creek drainage in 2004 only to capture Step Creek in 2006. Each of these shifts, as well as development of the UNFT channel system, involved incision. The process of vertical cutting then sets the stage for streambank instability and delivery of sediment through mass failures. It is this latter process that is hypothesized to be the dominant source of sediment in the UNFT.

Figure 26. 1980 photographs of water-filled depressions on the debris avalanche deposit (left). Filling and spilling of these depressions resulted in the first channels that developed on the deposit (right). Photographs from the USGS.

7.1 Spatial Trends of Channel Incision

By 2010, depths of incision had reached 40 m in some locations with these maximum values occurring in the vicinity of the Truman and Loowit channel confluence (rkm 42-43). It is not the total amounts of incision that are critical to determining future sediment loadings, but whether incision rates are constant or whether they are decaying at some rate.

As the timing, magnitude and location of erosion is closely related to flow magnitude, three periods of exceptionally high flows were identified. The first was an extended period during

1982 which included the pumping and breakout of debris-dammed lakes, a lahar and significant storm events on January 24, February 20 and December 3. The second was the February 1996 event, which for the purpose of this analysis also includes the rain-on-snow event of January 1, 1997. The third event is the November 2006 event which followed a period of intense rainfall, generating small debris flows in the Loowit, Step and Glacier Creek drainages. Amounts of incision caused by these three events (periods) were obtained from analysis of time-series thalweg elevations and are shown in Figure 27.

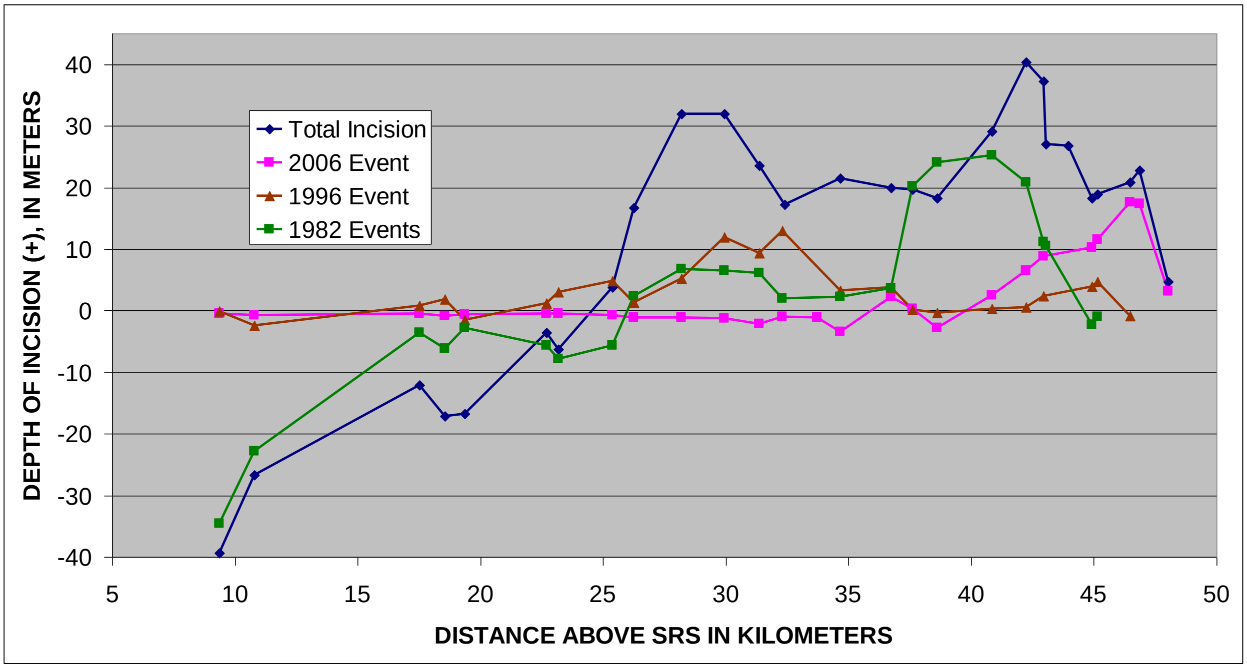

Figure 27. Magnitude and distribution of incision for the UNFT. Note: (1) localized zones of incision for the series of events during 1982 caused by floods, the breakout of Jackson Lake in the Elk Rock reach and the initiation of pumping from Spirit Lake into the Truman channel and (2) limited longitudinal extent of incision for the November 2006 event. Negative values denote deposition.

The 1982 events produced massive amounts of incision (up to 25 m) within the reach between upper Truman channel and NF125, as continuous pumping from Spirit Lake easily eroded through pyroclastic flow deposits (Paine, 1984). In the Elk Rock reach, 6-7 m of incision occurred as additional flow was provided by the breakout of Jackson Lake. This is also the location of the confluence of Castle and Coldwater Creeks with the UNFT. It is also interesting to note the large amounts of aggradation occurring downstream of the toe of the debris avalanche deposit, reaching almost 35 m through 1982 (pre-SRS). The 1996 event, the largest post-eruption flow caused considerably less incision than the 1982 flows. Magnitudes of incision peak at about 12-13 m and are again focused in this confluence reach. A secondary peak occurs in the downstream end of the Loowit channel (LO33 – LO100) at rkm 43-45. Finally, incision caused by the 2006 event is restricted in spatial extent and peaks in the upper Loowit channel with maximum incision reaching depths of more than 17 m. Depths of incision from this event decrease systematically with distance downstream from rkm 47 (LO31 and LO32) (Figure 27 and Table 11).

Table 11. Calculated amounts of incision for three specified time periods and for the entire 30-year post-eruption period (1980-2010). Note: Negative values denote deposition.

1982 Events			1996 Event			2006 Event		
Section	**Rkm**	**Incision**	**Section**	**Rkm**	**Incision**	**Section**	**Rkm**	**Incision**
NF405	9.37	-34.6	NF405	9.37	-0.064	NF405	9.37	-0.53
NF400	10.79	-22.8	NF400	10.79	-2.44	NF400	10.79	-0.725
NF375	17.52	-3.63	NF375	17.52	0.76	NF375	17.52	-0.48
NF365	18.56	-6.21	NF365	18.56	1.80	NF365	18.56	-0.86
NF360	19.36	-2.75	NF360	19.36	-1.54	NF360	19.36	-0.59
NF350	22.68	-5.59	NF350	22.68	1.16	NF350	22.68	-0.46
NF345	23.18	-7.89	NF345	23.18	3.04	NF345	23.18	-0.5
NF327	25.39	-5.61	NF327	25.39	4.87	NF327	25.39	-0.761
NF320	26.26	2.36	NF320	26.26	1.29	NF320	26.26	-1.14
NF310	28.21	6.80	NF310	28.21	5.26	NF310	28.21	-1.07
NF305	29.95	6.46	NF305	29.95	11.9	NF305	29.95	-1.31
NF300	31.38	6.12	NF300	31.38	9.36	NF300	31.38	-2.16
NF Confl.	32.29	1.93	NF Confl.	32.29	12.94	NF Confl.	32.29	-1.03
NF130	34.66	2.24	NF130	34.66	3.31	CA230	33.72	-1.11
NF125	36.72	3.63	NF125	36.72	3.73	NF130	34.66	-3.4
NF120	37.62	20.20	NF120	37.62	0.16	NF125	36.72	2.29
NF117	38.62	24.10	NF117	38.62	-0.28	NF120	37.62	0.28
NF110	40.83	25.30	NF110	40.83	0.30	NF117	38.62	-2.75
NF105	42.25	20.9	NF105	42.25	0.56	NF110	40.83	2.50
LO100	42.94	11.2	LO100	42.94	2.43	NF105	42.25	6.49
TR100	43.04	10.45	LO40	44.92	3.88	LO100	42.94	8.85
LO40	44.92	-2.29	LO33	45.15	4.7	LO40	44.92	10.2
LO33	45.15	-0.97	LO32	46.46	-0.82	LO33	45.15	11.5
						LO32	46.46	17.6
						LO31	46.85	17.3
						LO30	48.02	3.18

Digitizing the areas under each of the incision plots, bounded by the 0.0 incision line (Figure 27), provides a rough indication (in m^2) of the amount of material eroded (per unit width) during each of the periods, as well as total incision since 1980 (Table 12). Incision from these three periods represents 75.6% of the total erosion by incision for the entire post-eruption period, indicating that only 24.4% of the incision along the UNFT occurred during the remaining time. It is also interesting to note that the relative contributions from each of these periods decreases with time. The comparison is of course an approximate one since discharge rates and durations are not considered here. Still, the 1996 and 2006 events provide a possible glimpse of how and where future, major hydrologic events will impact the UNFT.

Table 12. Summary of incision along the UNFT, 1980-2010. [1]Calculated by multiplying incision depth by reach lengths, therefore assuming unit width.

Time period	**Maximum Incision (m)**	**Location of maximum incision (km)**	**Area eroded[1] (m^2)**	**Contribution to total (%)**
1982 events	25.3	40.83; NF110	184,500	38.8
1996 event	12.9	32.29; NF confluence	103,000	21.7
2006 event	17.6	46.46; LO32	71,600	15.1
1980-2010	**40.4**	**42.25; NF105**	**475,000**	**-**

Indicative of the evolving transport conditions along the UNFT, the 2006 event resulted in deposition (aggradation) from about rkm 36 downstream to the SRS. This is the only one of these three major events where more of the UNFT experienced infilling then downcutting. The great amounts of incision in parts of the Loowit channel during November 2006 are, however, the result of a combination of two events that took place higher on the mountain.

First, the avulsions of Loowit Creek (all upstream of LO33) from its original course draining into Spirit Lake before October 2004, then into Step Creek during October 2004 and finally into its present course where Step Creek became a tributary to Loowit, represents an ever increasing contributing drainage area to this short section of channel (Figure 28). The sequence of events shown in Table 13 and linked to Figure 28 was provided by Kurt Spicer of the U.S. Geological Survey, Cascades Volcano Observatory. The result was that a greater volume of flow was concentrated in the reach for the imposed rainfall-runoff conditions.

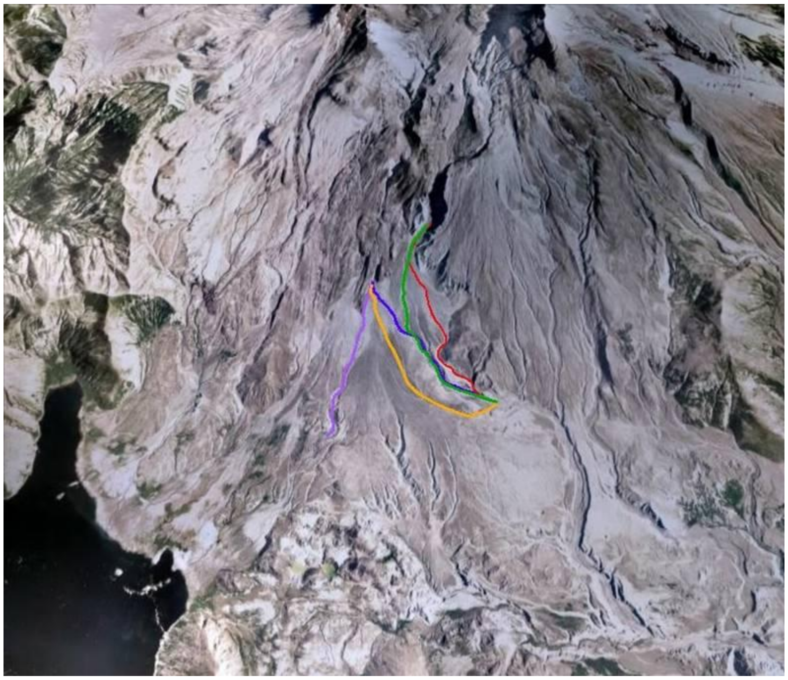

Figure 28. Paths taken by Loowit and Step Creeks (See Table 13 for color code). Modified from K. Spicer, U.S. Geological Survey, pers. comm., 2009.

Table 13. Sequence of course changes to Loowit and Step Creeks. Modified from K. Spicer, U.S. Geological Survey, pers. Comm.., 2009.

Channel	Line color in Figure 28	Date	Event
Loowit	Light purple	Pre 2004	Loowit Creek drained into Spirit Lake prior to a heavy rainfall event in October 2004. A small debris flow came down Loowit canyon and caused the flow to shift over to the route indicated by the dark purple line, where it stayed until November, 2006
Loowit	Dark purple	Pre 2006	Route of Loowit Creek below falls prior to the early November 2006 high rainfall event, and following the October 2004 event
Loowit	Gold	Post 2006	Route of Loowit Creek below falls prior to the early November 2006 high rainfall event, and following the October 2004 event
Step	Red	Pre 2006	Route of Step Creek channel below falls prior to the early November 2006 high rainfall event. End of the red line is at the confluence with Loowit Creek
Step	Green	Post 2006	Route of Step Creek below falls following the high rainfall event in early November, 2006

Second, there is field evidence in the Glacier Creek and Loowit drainages of a series of small debris flows that were released during the day or days preceding the peak flow on November 7 (K. Spicer, 2009, USGS pers. comm.). One tributary to Glacier Creek was found dammed by the debris flow and dendro-chronologic dating of trees growing proximal to the surface indicated germination in 1997, the first growing season after the event. Similar deposits were found in some of the Loowit tributaries that enter Loowit channel just upstream of LO33. Most importantly, evidence of a breached debris dam was located between LO100 and LO40 (Figure 29). Again dendro-chronologic evidence indicated that the dam had formed in 2006. The implications are that the debris dam blocked high flows for a brief period time during the 2006 event. Upon breaching, flows would have been released rapidly providing sufficient shear stress to contribute to the large-scale incision in this reach during the event. Without conditions such as these, flow depths and average boundary shear stresses at LO100 (calculated using a normal depth approximation) would have been about 40-50 cm and between 78 and 91 Pa, respectively.

Incision along the Loowit channel during the 2006 event decreased rapidly from 17.3 m to 3.2 m over a 1.2 km reach between LO31 and LO30. One of the knickpoints formed in the reach as a result of the flows is shown in Figure 30. It is expected that additional incision will eventually occur upstream of rkm 47 along Loowit channel. Conditions are somewhat different further west along Glacier Creek where advancement of a series of knickpoints flowing over bedrock will likely limit further headcutting (Figure 30).

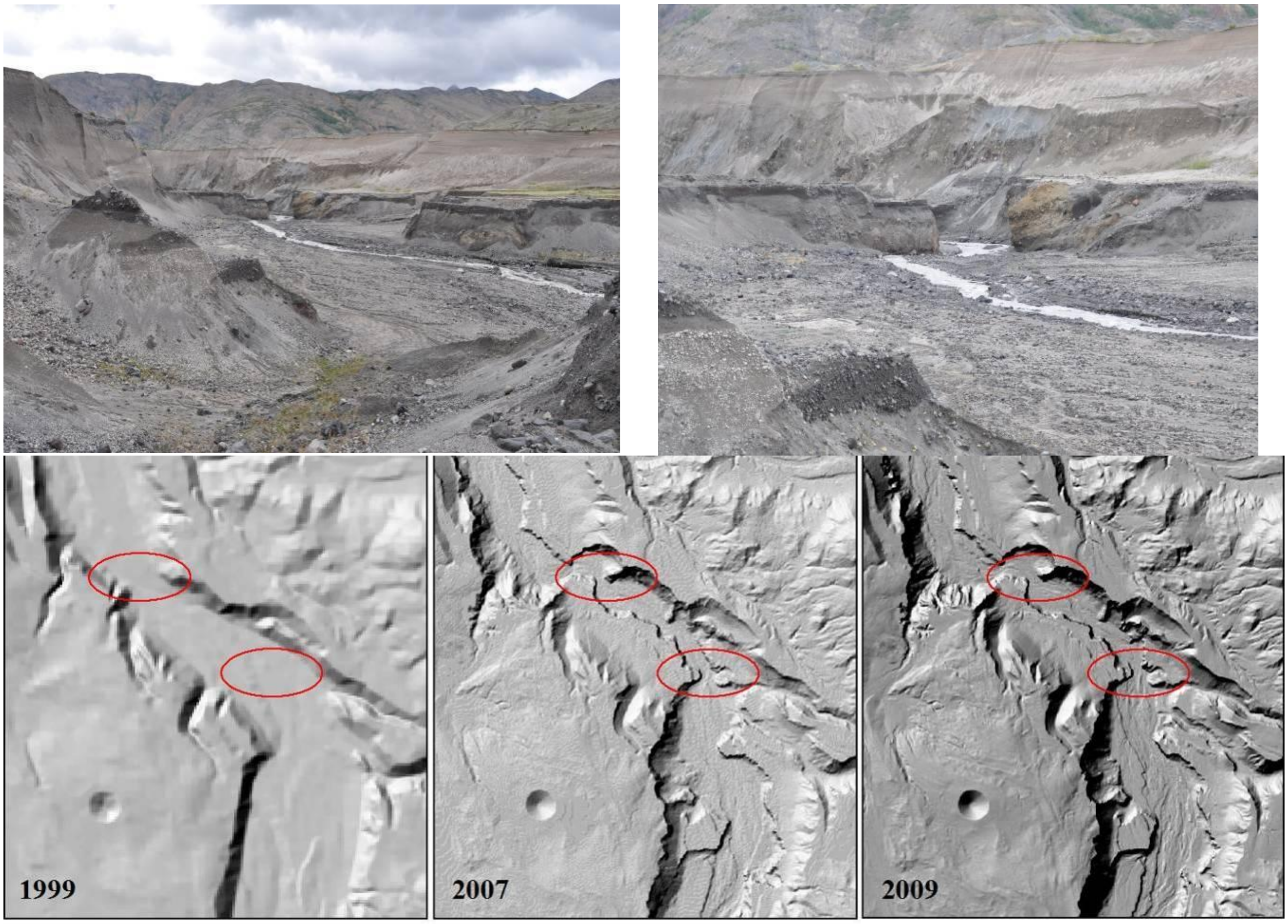

Figure 29. Photographs of the remains of a possible debris dam formed between LO100 and LO40 in November 2006 (top), photographs by USDA-ARS, NSL, and DEMs of the reach at three specific times, showing no constriction in 1999 and constrictions in 2007 and 2010.

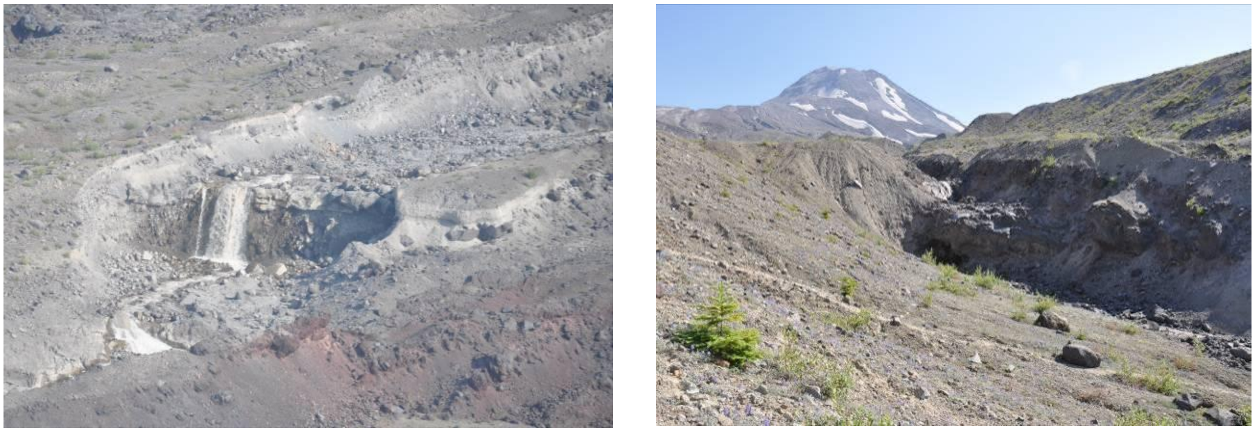

Figure 30. Knickpoints marking the upstream limit of incision processes as of 2010. The site on on Loowit channel between LO31 and LO30 (left) probably formed during the 2006 event. The knickpoints shown on upper Glacier Creek (right) are likely to be stationary for a long period of time as the materials are composed of "old" mountain. Photographs by USDA-ARS, NSL.

7.2 Linking Spatial with Temporal Trends of Incision

Analysis of bed-level changes at a site with time provides evidence of the ‘nature’ of vertical adjustment processes and aids in answering the question whether erosion rates are decaying with time. Example results are shown for sites along the UNFT in Figures 31 and 32. Although there are perturbations to smooth non-linear decay functions, the concept that erosion and/or deposition rates decay with time is clear. In addition, linking temporal changes at a site with the spatial distribution of post-eruption erosion rates along the UNFT results in an empirical model of bed-level response. *b*-values (Equation 26), representing the non-linear rate of change on the bed are used as the metric to quantify post-eruption bed-level response, as well as a potential means to predict future changes.

Calculated *b*-values for each site are plotted against distance upstream of the SRS to produce this empirical model of bed-level response for the UNFT (Figure 33). The two lines shown in the figure represent to methods of calculating regression coefficients from the elevation versus time data extracted from ground surveys and DEMs. The blue line was created from regressions where it was assumed that t_0 was1980 (t_0 = 1.0), that bed-level adjustment started immediately and continued un-interrupted. Thus, this analysis represents rates of net bed-level change over the entire 30-year post-eruption period. Here, the typical pattern of bed-level adjustment in disturbed systems can be seen with aggradation downstream with degradation rates attenuating with distance upstream. This pattern is consistent for stream systems from diverse regions where for one reason or another, the system is experiencing excess amounts of transporting power relative to transport capacity. Degradation rates generally peak in the “area of maximum disturbance” and decrease with distance away from it. In the case of the UNFT, this was the area just upstream of Elk Rock where a constriction in the UNFT valley resulted in some of the thickest debris avalanche deposits (in excess of 100 m). This is also the area where Castle and Coldwater Creeks flow into the North Fork Toutle River. Downstream ends of these tributaries, responding in icsion on the main stem, incised at commensurate rates. A secondary peak in degradation rates occurs near the confluence of the Truman and Loowit channels (NF100), an area impacted by pumping flows from Truman channel as well as the avulsions on Loowit Creek discussed earlier.

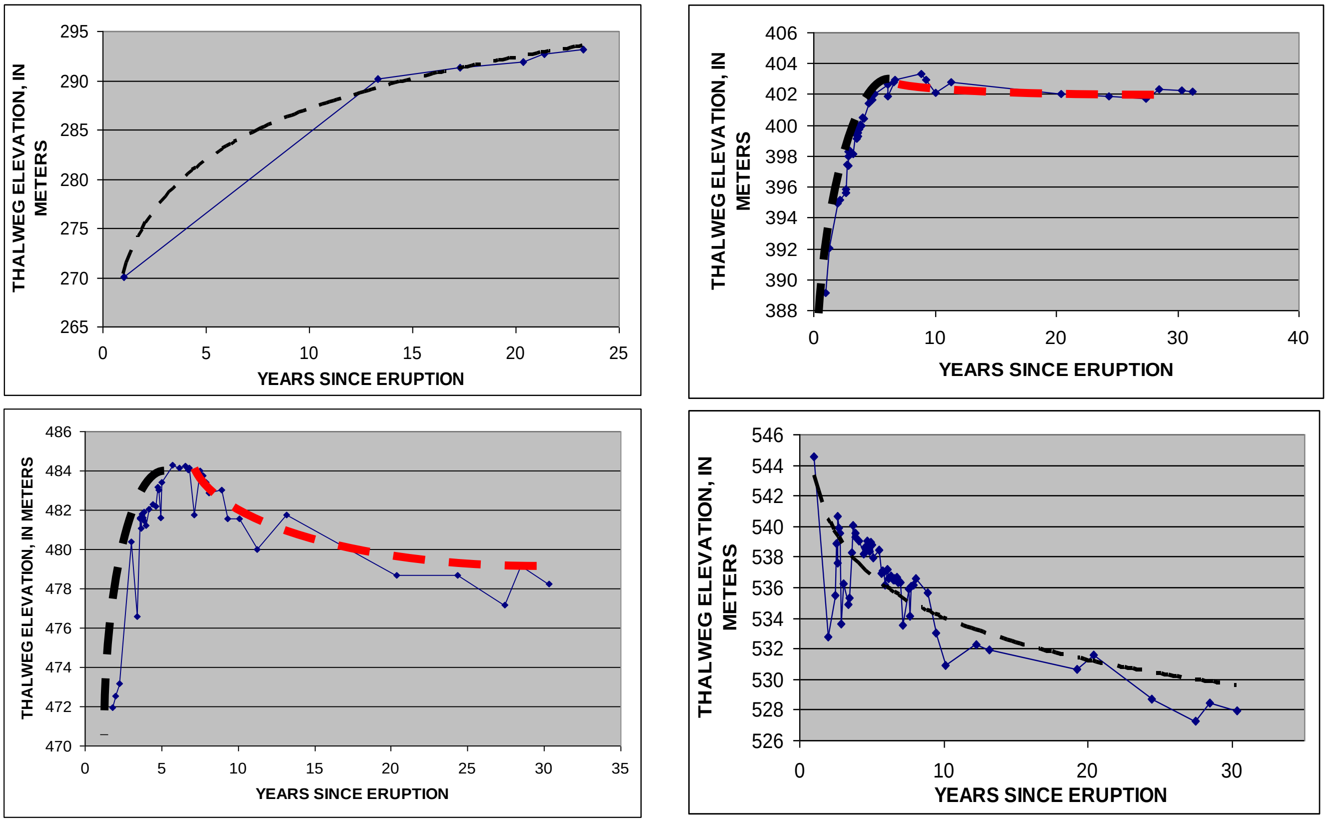

Figure 31. Examples of bed-level adjustment trends showing decay in erosion and deposition rates of initial and, if applicable, secondary adjustments. Moving clockwise from upper left: NF435, NF 375; NF320, NF125.

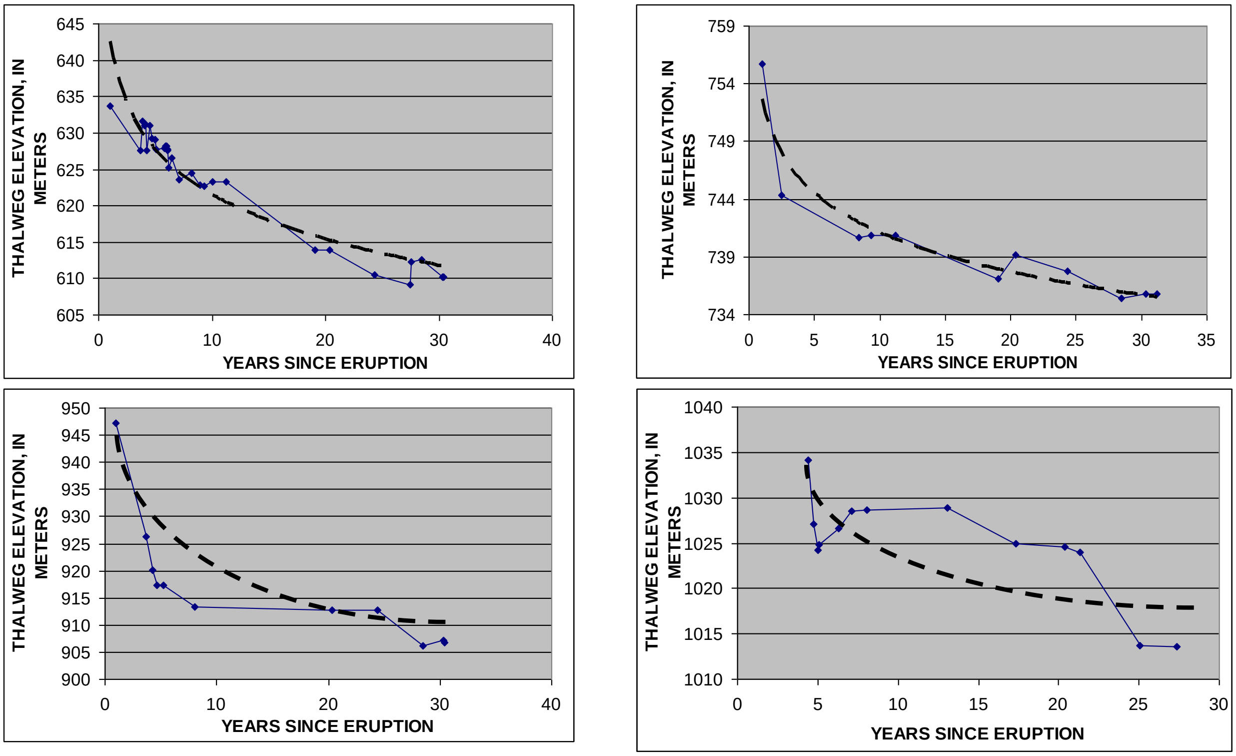

Figure 32. Examples of bed-level adjustment trends showing decay in erosion and deposition rates of initial and, if applicable, secondary adjustments. Moving clockwise from upper left:, LO40, NF105, NF300, and NF345.

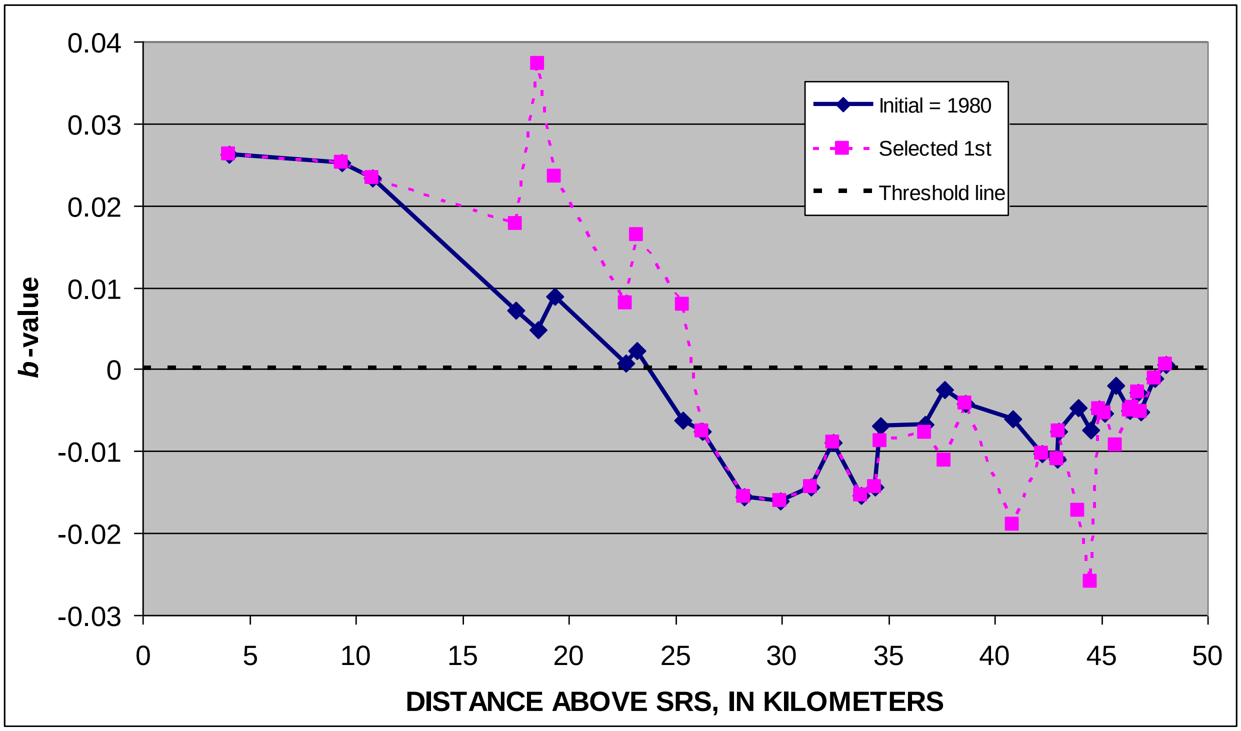

Figure 33. Empirical model of bed-level response for the UNFT. Plotted values are the exponent '*b*' in the power regression E = $a\ t^{b}$ describing the non-linear decay rate of bed-level degradation (-) or aggradation (+).

Aggradation is typical in downstream reaches as the transport capacity of these reaches becomes overwhelmed with the loads delivered from eroding reaches upstream. Simon (1992) documented how two completely different systems, one a cohesive banked, channelized system in West Tennessee, the other the Toutle River System responded in identical ways.

In contrast, the other data series shown in pink in Figure 33 uses *b*-values from regressions created selectively based on the timing of the start of bed-level adjustment, and carried out until a secondary adjustment phase started. This analysis provides a more detailed view of differences between specific sites or reaches, and helps to explain some of the anthropogenic or other atypical events. Although *b*-values using both methods are similar for several extended reaches, a number of locations clearly stand out. The most rapid degradation rates, represented by the most negative *b*-values are for the sites along Truman channel (between rkm 43.9 and 45.7) as a result of the pumping from Spirit Lake between November 1982 through 1985. Here, sediment free water released at 5 m^3/s over the period deeply incised the channel (up to 36 m) by 1985. No further incision occurred and today some reaches of Truman channel are characterized by coarse bed material (resisting further incision) and riparian vegetation helping to stabilize low-bank surfaces. The other clear divergence from the 't_o=1980' trend line is the zone of accelerated aggradation shown between river kilometer 11 and 26. This zone, downstream of the Elk Rock constriction experienced more rapid deposition that would have occurred due to the construction of the SRS. Points further downstream do not diverge or show accelerated deposition rates, probably due to the lack of data in the 1980s that would have helped to define a more rapid rate of infilling then was calculated using the available DEMs.

7.3 Volumes of Erosion from the UNFT

Previous sections of this report have focused on the methods employed to quantify erosion rates from the UNFT and to document that vertical adjustment processes do indeed display the non-linear decay typical of adjusting fluvial systems. Given the original hypotheses of this study, that lateral erosion of streambanks, terraces and hummocks represents the dominant source of sediment being transported through the UNFT, this section explicitly investigates the volumes, relative contributions and rates of change of lateral erosion. The physical basis behind the hypothesized decay in lateral erosion rates is that as banks retreat, the effective shear stress acting on the bank surfaces will be less, as flow depths for a given discharge are reduced. In combination with increases in relative roughness (with decreasing flow depths), this would result in a reduced tendency for hydraulic erosion, undercutting of the banks and failure frequency. The net result of this would be reduced erosion rates with time. The manifestation of these processes (ie. decay in lateral erosion rates) is quantified using the database of time-series ground surveys and DEMs for the UNFT. Results of this analysis are then used to extrapolate erosion rates and volumes for 100 years into the future.

Calculated by taking the average erosion/deposition for beds and banks between adjacent sites and multiplying by the reach length, gross erosion (excluding any deposition) between 1980 and 2010 was 312 million m^3 (408 million yd^3). Of this, 20.3% came from the streambeds while 79.7% was eroded from channel banks and terraces. When accounting for the deposition in downstream reaches, net eroded volumes reaching the N-1 structure were 286 million m^3 (374 million yd^3) by 2010. The spatial distribution of erosion/deposition above N-1 (rkm 15.57) and the overwhelming dominance of lateral erosion as a sediment source are shown in Figure 34. Results are strikingly similar to those shown previously for erosion by incision (Figures 27 and 33), with peak erosion in the Elk Rock reach centered at rkm 26-30 and thus support one of the major theses of this study, that lateral erosion is the single most important sediment source in the UNFT.

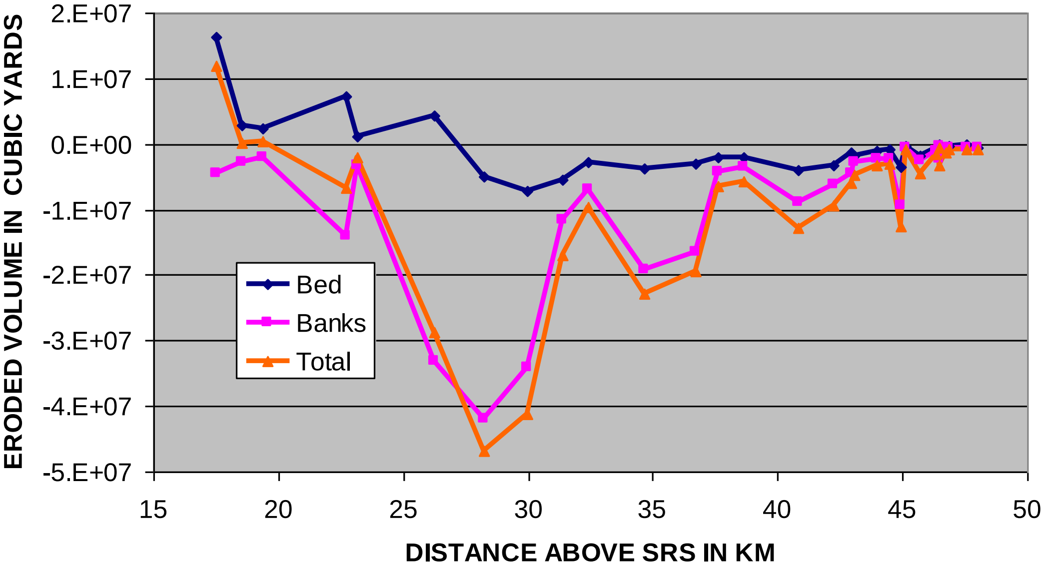

Figure 34. Volume of material eroded/deposited by bed and bank processes along the UNFT above N-1 between 1980 and 2010.

Using the procedures described in earlier sections of this report, non-linear regressions of eroded/deposited area versus time were developed from overlain, time-series cross sections for each site. Calculated areas (in m^2) at each site were then converted to volumes by multiplying values by the length of the reach to the next downstream cross section. Solving this series of equations for 30 years (2010) provides a check on the values obtained by averaging volumes between cross sections. Using the regression approach, net erosion was calculated to be 290 million m^3 (379 million yd^3), a difference of only 1.5%. Results for predicted erosion volumes emanating from the bed and banks, as well as totals, are plotted through 2035, and definitively provide two important conclusions regarding future erosion rates (Figure 35):

1. Streambank erosion is the dominant source of sediment, and
2. Rates of erosion decay non-linearly with time.

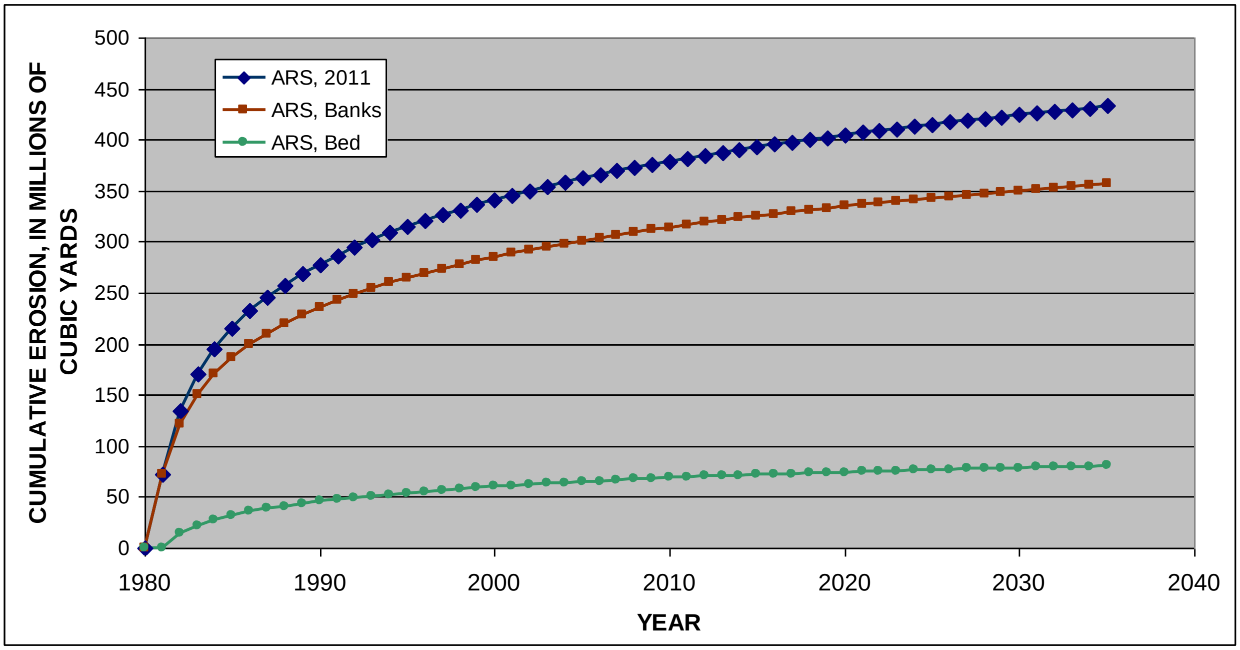

Figure 35. Calculated erosion volumes for the UNFT through 2035. Note (1) the dominance of streambank erosion as the major source of sediment, and (2) the non-linear decay in erosion rates.

Results through 2010 are greater than those of two recent studies by West Consultants (2002) and Biedenharn (2010) over the same period (Figure 36), who obtained values of 289 and 338 million yd^3, respectively. These other studies used DEM data exclusively. With a lower temporal resolution than is provided by this study, it is possible that changes in erosion rates over the first 7 to 19 post-eruption years may have been less precise. When comparisons are extended through to 2035 (Figure 36), however, the values obtained in this study fall between those from West Consultants (2002) and Biedenharn (2010). Data within the Biedenharn (2010) report also supports the general premise throughout this report of decaying rates of erosion with time; Biedenharn (2010) average annual erosion rates reproduced in Table 14.

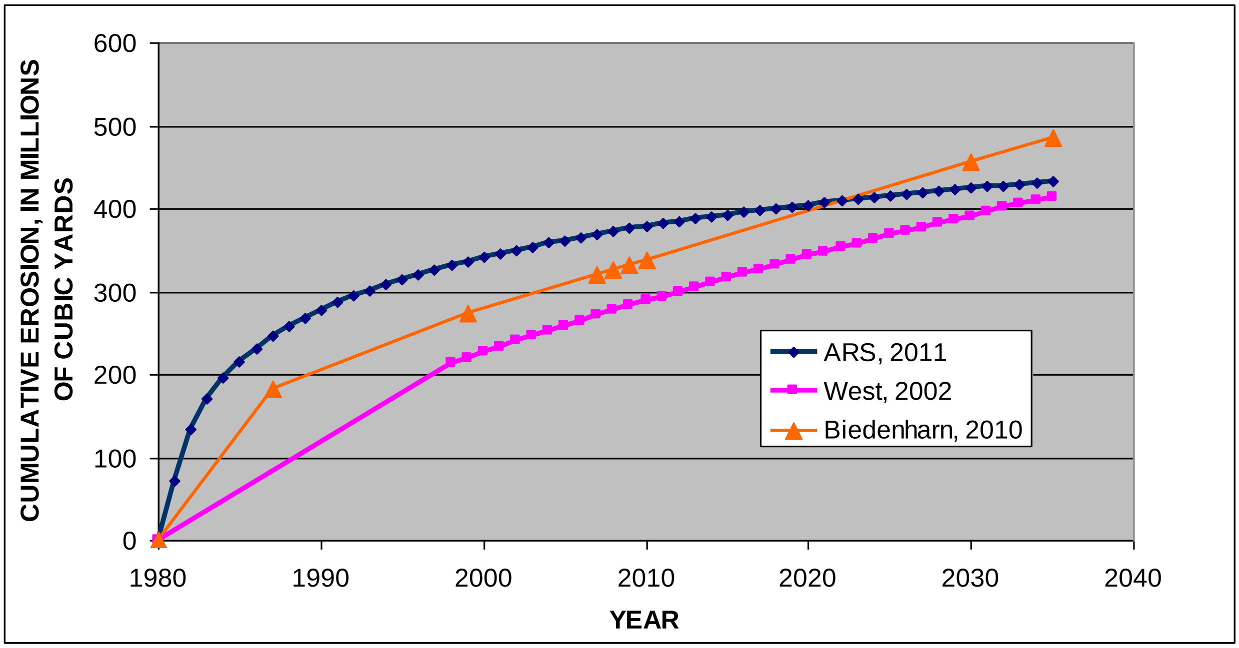

Figure 36. Comparison of cumulative-erosion rates from the debris avalanche to 2035.

Table 14. Debris avalanche erosion, 1984-2007. Modified from Table 4.6 in Biedenharn (2010).

Surface comparison	**Erosion (million yd^3/y)**
1984-1987	26.2
1987-1999	7.5
1999-2007	5.9

Solving the ARS 2011 non-linear regression equation through 2110 gives a calculated, total erosion volume of 509 million yd^3, indicating that an additional 130 million yd^3 will be eroded from the debris avalanche and delivered to the N-1 structure in the next 100 years (Table 15). The temporal distribution of this erosion is shown in Figure 37.

Table 15. Predicted cumulative erosion delivered to N-1 from the UNFT System. Years 2035 and 2110 (100 years from present) are shown shaded.

Cumulative Erosion from Upper North Fork Toutle					
Year	**Mm^3**	**Myd^3**	**Year**	**Mm^3**	**Myd^3**
1980	0	**0**	2010	289.9	379.1
1981	55.1	72.1	2011	292.1	382.0
1982	102.3	133.8	2012	294.2	384.9
1983	129.9	170.0	2013	296.3	387.6
1984	149.6	195.7	2014	298.4	390.2
1985	164.9	215.6	2015	300.3	392.8
1986	177.4	232.0	2016	302.2	395.3
1987	188.0	245.9	2017	304.1	397.7
1988	197.2	257.9	2018	305.9	400.1
1989	205.3	268.5	2019	307.7	402.4
1990	212.6	278.0	2020	309.4	404.7
1991	219.2	286.7	2021	311.1	406.9
1992	225.2	294.6	2022	312.7	409.0
1993	230.8	301.9	2023	314.3	411.1
1994	236.0	308.6	2024	315.8	413.1
1995	240.8	314.9	2025	317.4	415.1
1996	245.3	320.8	2026	318.9	417.1
1997	249.5	326.4	2027	320.3	419.0
1998	253.6	331.6	2028	321.7	420.8
1999	257.4	336.6	2029	323.1	422.7
2000	261.0	341.4	2030	324.5	424.5
2001	264.4	345.9	2031	325.9	426.2
2002	267.7	350.2	2032	327.2	427.9
2003	270.9	354.3	2033	328.5	429.6
2004	273.9	358.3	2034	329.7	431.3
2005	276.8	362.1	2035	330.98	432.9
2006	279.6	365.7	2050	347.3	454.3
2007	282.3	369.2	2070	364.4	476.6
2008	284.9	372.7	2090	378.0	494.4
2009	287.4	375.9	2110	389.34	509.3
			2010-2035		**53.8**
			2010-2110		**130.1**

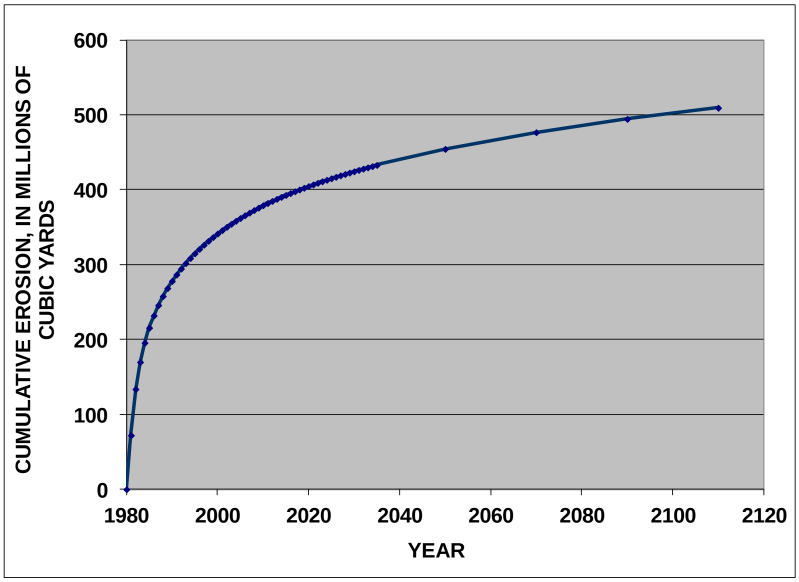

Figure 37. Predicted cumulative-erosion rates to 2110, in millions of cubic yards clearly show a decay in erosion with time.

Data used to generate Figure 37 are shown, by reach, in tabular form to discern the spatial distribution of future erosion along the UNFT (Table 16). Notwithstanding differences in reach lengths between sites, erosion volumes over the next 100 years vary across almost four orders of magnitude. Again, most of this material will be delivered by lateral erosion of banks and terraces. Preliminary numerical modeling results with the BSTEM (Simon *et al*., 2000) show how relative bank stability is controlled by the magnitude and duration of shear forces operating at the base of bank and terrace slopes. With slopes 10-40 m high, and peak-flow depths in the range of 0.5 m, potential reductions in bank strength by lateral seepage and generation of positive pore-water pressures is a non-factor. Channels shift back and forth across the braid plain. Slope/bank instability occurs when one of these braids impacts the toes of slopes at the edge of the braid plain, causing steepening and undercutting of the material. During the highest flows when flow depths exceed the depth of the braids, hydraulic forces may impact both edges of the channel at the same time. When hydraulic erosion is sufficient for the gravitational forces to exceed the geotechnical resistance of the slope, mass failure of the entire slope can occur, creating long talus slopes set at the angle of repose of the material (Figure 38). These slopes may remain dormant for some time if the channel moves to the other side of the braid plain.

Figure 38. Talus slopes formed from mass failure of in situ materials following undercutting by hydraulic forces, STEP32 (left) and LO100 (right). Photographs by USDA-ARS, NSL.

Table 16. Volumes of erosion for the UNFT projected to 2110.

Site name	Distance above SRS (km)	Volume of Erosion (yd^3)							
		1980-2010	2010-2030	2030-2035	2030-2050	2050-2070	2070-2090	2090-2110	Future Erosion (2010-2110)
Mainstem									
N-1	15.57								
NF375	17.52	2103947	-1249098	-233058	-822760	-614527	-490691	-408490	**-3.82E+06**
NF365	18.56	-166728	-636821	-118818	-419463	-313301	-250166	-208258	**-1.95E+06**
NF360	19.36	1388325	-40383	-7535	-26599	-19867	-15864	-13206	**-1.23E+05**
NF350	22.68	-19241590	-4804597	-896445	-3164707	-2363751	-1887419	-1571236	**-1.47E+07**
NF345	23.18	-1077482	-524156	-97797	-345253	-257873	-205908	-171414	**-1.60E+06**
NF320	26.26	-52802831	-7568398	-1412117	-4985176	-3723477	-2973139	-2475075	**-2.31E+07**
NF310	28.21	-58546761	-9844245	-1836746	-6484239	-4843142	-3867174	-3219340	**-3.01E+07**
NF305	29.95	-25941527	-1453173	-271134	-957181	-714928	-570859	-475228	**-4.44E+06**
NF300	31.38	-11106968	-2793375	-521190	-1839949	-1374276	-1097338	-913511	**-8.54E+06**
NF Confl.	32.39	-11267051	-728289	-135885	-479712	-358301	-286098	-238171	**-2.23E+06**
NF130	34.66	-20949913	-3001687	-560057	-1977161	-1476761	-1179171	-981635	**-9.18E+06**
NF125	36.72	-19289651	-1803404	-336480	-1187872	-887233	-708442	-589763	**-5.51E+06**
NF120	37.62	-4151221	-290350	-54174	-191249	-142846	-114060	-94952	**-8.88E+05**
NF117	38.62	-6666282	-76709	-14312	-50527	-37739	-30134	-25086	**-2.35E+05**
NF110	40.83	-10512535	88221	16460	58110	43403	34657	28851	**2.70E+05**
NF105	42.25	-12225168	-1007348	-187952	-663523	-495592	-395722	-329430	**-3.08E+06**
TR100	43.04	-2930129	-277702	-51814	-182918	-136623	-109092	-90816	**-8.49E+05**
TR70	43.94	-4166363	-331553	-61861	-218388	-163116	-130246	-108427	**-1.01E+06**
TR65	44.50	-2695754	-168307	-31403	-110861	-82803	-66117	-55041	**-5.15E+05**
TR60	45.69	-1073436	-86865	-16207	-57217	-42736	-34124	-28407	**-2.66E+05**
LO100	42.94	-5135051	-775871	-144763	-511053	-381711	-304790	-253731	**-2.37E+06**
LO40	44.92	-6869855	-1062887	-198314	-700106	-522916	-417540	-347593	**-3.25E+06**
LO33	45.15	-440912	-99863	-18632	-65778	-49130	-39230	-32658	**-3.05E+05**
LO32	46.46	-2865928	-445295	-83083	-293308	-219075	-174928	-145624	**-1.36E+06**
LO31	46.85	-377744	-71854	-13407	-47329	-35350	-28227	-23498	**-2.20E+05**
LO30	48.02	-288914	-21309	-3976	-14036	-10483	-8371	-6969	**-6.51E+04**
Step32	46.33	-856409	-98577	-18393	-64931	-48497	-38724	-32237	**-3.01E+05**
Step31L	46.45	-178578	-4995	-932	-3290	-2458	-1962	-1634	**-1.53E+04**
Step31R (mid)	46.70	-443127	-10408	-1942	-6856	-5121	-4089	-3404	**-3.18E+04**
Step30	47.54	-205397	-142581	-26603	-93916	-70147	-56011	-46628	**-4.36E+05**
Tributaries									
CA230	0.34	-2106670	-142533	-26594	-93884	-70123	-55992	-46612	**-4.36E+05**
CA225	2.32	-12356170	-1981569	-369722	-1305226	-974886	-778432	-648028	**-6.06E+06**
CA220	3.76	-10359675	-819779	-152955	-539975	-403313	-322039	-268091	**-2.51E+06**
CA200	5.69	-5394262	0	0	0	0	0	0	**0.00E+00**
CW280	1.98	-13277363	-1527302	-284965	-1006008	-751398	-599979	-499470	**-4.67E+06**
CW245	2.94	-2128117	-256933	-47939	-169238	-126405	-100933	-84024	**-7.85E+05**
CW255	3.49	-720709	-64195	-11978	-42284	-31583	-25218	-20994	**-1.96E+05**
SF Coldwater		-6505320	-584137	-108989	-384761	-287382	-229470	-191029	**-1.79E+06**
Upper Carbonate Springs		-7854464	-197419	-36835	-130037	-97126	-77553	-64562	**-6.04E+05**
Lower Carbonate Springs		-8262117	-258645	-48258	-170365	-127247	-101605	-84584	**-7.91E+05**
Unnamed Loowit Tribs		-3937315	-2000	-373	-1317	-984	-786	-654	**-6.11E+03**
Upper Glacier		-14330121	-187756	-35032	-123671	-92371	-73757	-61401	**-5.74E+05**
Studebaker		-12921900	23745	4430	15640	11682	9328	7765	**7.26E+04**
Total		**-3.79E+08**	**-4.53E+07**	**-8.46E+06**	**-2.99E+07**	**-2.23E+07**	**-1.78E+07**	**-1.48E+07**	**-1.39E+08**

8. BANK-MODELING OF FUTURE EROSION RATES

BSTEM-Dynamic 1.0 was used to simulate bank-erosion processes and rates for the UNFT and selected tributaries for 100 years into the future (to 2110). One bank (left or right) was to be modeled at each cross section. This was selected as the bank that had the greatest amount of widening during the calibration period, which in most cases represented current conditions. Before simulations of the next 100 years could be carried out, model calibrations were conducted for most of the sites.

8.1 Distribution of input parameters for BSTEM

Analysis of the geotechnical parameters input to BSTEM showed that the bank material friction angles varied within a narrow range of 20 degrees to 35.5 degrees. The distribution within this range was fairly linear (Figure 39) with both the mean and median value occurring at approximately 32 degrees, which typically corresponds to materials with a high sand content.

Values of effective cohesion (*c'*) input to BSTEM-Dynamic 1.0 from field data showed a high degree of variability, ranging from 0 to 47.5 kPa. Investigation of the distribution of *c'* values, however, showed that the data set was heavily skewed towards bank materials with low cohesion values, with the median *c'* value being just 0.4 kPa (Table 17; Figure 39). This is not surprising given the granular nature of the bank materials. Cohesion is a characteristic of fine-grained materials, accounting for the strength of the electro-chemical bonds binding clay minerals. However, the banks and terraces of the debris avalanche deposit are almost devoid of clay. Cohesion measured in these materials is, therefore, considered to emanate from cementation or thermal alteration during emplacement of the debris avalanche. Thus the measured cohesion is not a true cohesion but still serves to increase the shear strength of the *in situ* bank materials.

The site specific data shown in Table 18 indicate that there are many layers of bank material with very little or no cohesion; these layers are dominated by un-cemented sands and gravels. Reaches upstream of the Loowit Truman confluence (the Pumice Plain) are dominated by pumice and contain some thermally altered and cemented materials represented by layers with significant cohesion.

Table 17. Summary statistics for BSTEM input parameters.

	Friction angle ϕ' (degrees)	*Cohesion c' (kPa)*	τ_c (Pa)	*k* (cm^3/Ns)
Minimum	20.0	0.00	0.22	0.03
Maximum	35.5	47.5	32.1	5.59
Mean	31.8	6.29	7.40	0.73
Median	32.3	0.40	6.01	0.33
St. Dev.	3.24	12.0	6.08	1.16

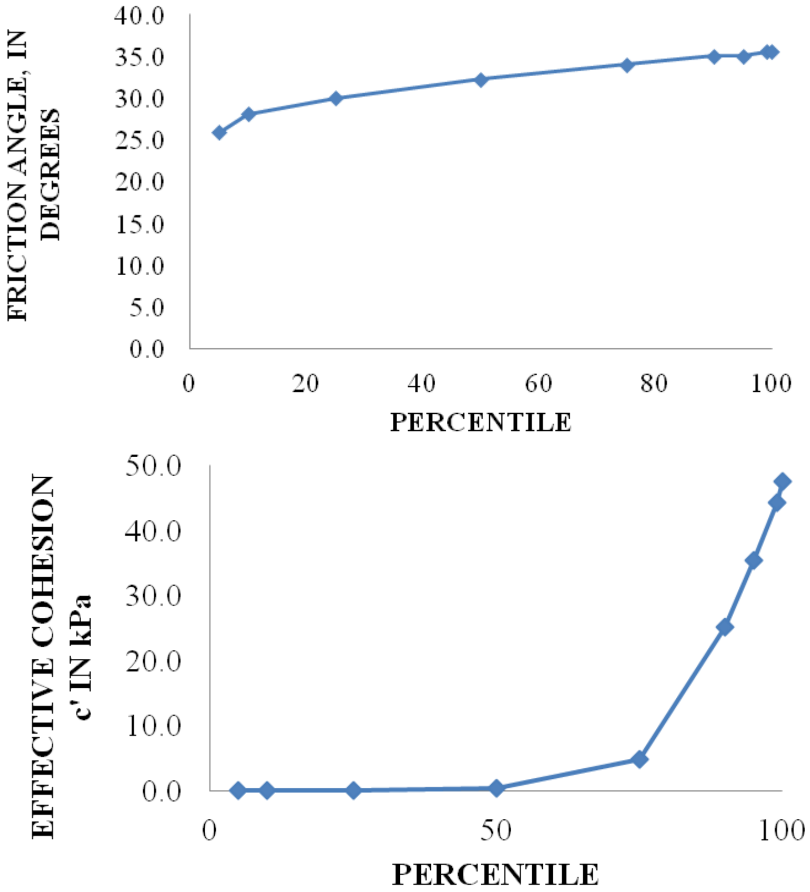

Figure 39. Distribution of friction angles (top) and effective cohesion (bottom) for *in situ* bank materials modeled in BSTEM.

Critical shear stress (τ_c) of the bank-toe materials represents the primary variable in resisting hydraulic undercutting. The τ_c values for d_{50} ranged from 0.22 to 32.1 Pa, values that generally correspond to fine sand and coarse gravel, respectively. The plot of distributions for τ_c values (Figure 40) shows that 95 % of the values were 15 Pa or lower, with just 5 % of values occurring within the 15 to 32 Pa range. The median τ_c value for all sites corresponds to a non-cohesive particle with a diameter of approximately 6.2 mm.

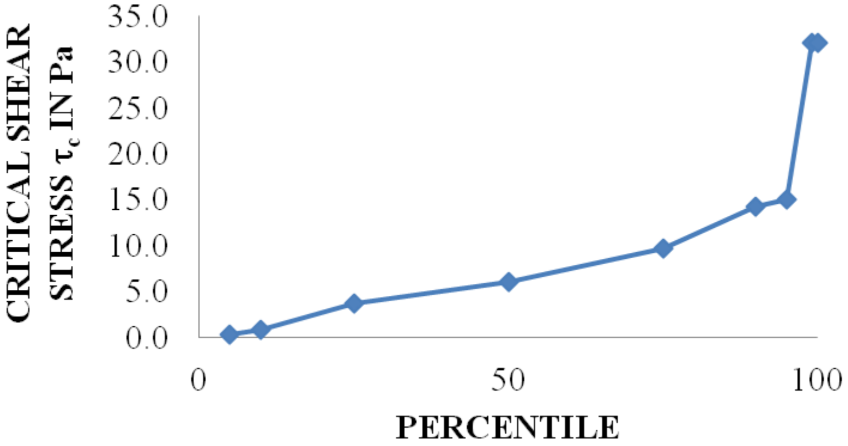

Figure 40. Distribution of τ_c values for bank and toe materials modeled in BSTEM.

Input parameters for hydraulic and geotechnical resistance of the bank and terrace materials were obtained from field data collected during the summer field seasons of 2009 and 2010. Previous sections have described the adjustment of critical shear stress values due to the low specific gravity of the sediments as well as the apparent cohesion measured at some sites in these granular materials due to cementation and thermal alteration. Input values for each of the sites are shown in Table 18.

Table 18. Input parameters for all sites simulated using BSTEM-Dynamic 1.0.

		Friction angle ϕ' (degrees)	Cohesion c' (kPa)	Saturated unit weight (kN/m^3)	ϕ^b (degrees)	Hydraulic Conductivity k_{sat} (m/s)	van Genuchten α (1/m)	van Genuchten n	τ_c (Pa)	k (cm^3/Ns)
CA230	Own data layer 1	30.0	0.0	19.6	15.0	3.160E-03	3.5237	2.3286	5.79	0.375
	Own data layer 2	30.0	0.0	19.6	15.0	3.160E-03	3.5237	2.3286	5.79	0.375
	Own data layer 3	30.0	0.0	17.3	15.0	7.439E-05	3.5237	3.1769	1.17	1.405
	Own data layer 4	33.0	0.0	18.2	15.0	7.439E-05	3.5237	3.1769	1.13	1.446
	Own data layer 5									
	Own data Bank Toe			18.2					4.96	0.426
CW280	Own data layer 1	34.0	4.7	19.5	15.0	5.064E-06	0.6577	1.6788	3.89	0.521
	Own data layer 2	34.0	4.7	19.5	15.0	1.745E-03	3.5237	2.3286	3.89	0.521
	Own data layer 3	34.0	0.0	19.5	15.0	1.745E-03	3.5237	2.3286	10.63	0.227
	Own data layer 4									
	Own data layer 5									
	Own data Bank Toe			19.5					8.40	0.276
		Friction angle ϕ' (degrees)	Cohesion c' (kPa)	Saturated unit weight (kN/m^3)	ϕ^b (degrees)	Hydraulic Conductivity k_{sat} (m/s)	van Genuchten α (1/m)	van Genuchten n	τ_c (Pa)	k (cm^3/Ns)
LO32	Own data layer 1	32.0	5.4	19.3	15.0	3.160E-03	3.5237	2.3286	3.01	0.644
	Own data layer 2	32.0	0.0	19.0	15.0	3.160E-03	3.5237	2.3286	3.44	0.576
	Own data layer 3									
	Own data layer 4									
	Own data layer 5									
	Own data Bank Toe			19.0					6.89	0.325
LO33	L2-4	33.5	25.7	18.9	15.0	9.473E-07	1.5812	1.4158	0.29	4.450
	L2-3	30.0	3.5	18.3	15.0	5.064E-06	0.6577	1.6788	0.29	4.450
	L2-2	32.0	0.0	19.7	15.0	7.439E-05	3.5237	3.1769	0.86	1.812
	L2-1	32.0	0.0	19.7	15.0	3.160E-03	3.5237	2.3286	5.54	0.389
	Toe	29.0	0.0	19.7	15.0	3.160E-03	3.5237	2.3286	2.80	0.684
	Own data Bank Toe			19.7					2.49	0.753
LO40	Own data layer 1	30.0	0.0	19.4	15.0	3.160E-03	3.5237	2.3286	12.15	0.203
	Own data layer 2	30.0	3.5	18.9	15.0	5.064E-06	0.6577	1.6788	0.29	4.450
	Own data layer 3	30.0	0.0	18.3	15.0	1.130E-06	4.0563	2.3286	0.86	1.812
	Own data layer 4	30.0	0.0	19.4	15.0	3.160E-03	3.5237	2.3286	9.18	0.256
	Own data layer 5									
	Own data Bank Toe			19.4					7.25	0.311
LO100	Own data layer 1	32.0	47.5	19.6	15.0	9.473E-07	1.5812	1.4158	5.28	0.405
	Own data layer 2	28.0	41.0	18.7	15.0	9.473E-07	1.5812	1.4158	0.22	5.592
	Own data layer 3	29.0	0.0	19.2	15.0	7.439E-05	3.5237	3.1769	6.46	0.343
	Own data layer 4									
	Own data layer 5									
	Own data Bank Toe			19.2					7.07	0.318

		Friction angle ϕ' (degrees)	Cohesion c' (kPa)	Saturated unit weight (kN/m^3)	ϕ^b (degrees)	Hydraulic Conductivity k_{sat} (m/s)	van Genuchten α (1/m)	van Genuchten n	τ_c (Pa)	k (cm^3/Ns)
NF105	Own data layer 1	33.0	36.0	20.7	15.0	1.708E-06	1.4962	1.2531	7.19	0.037
	Own data layer 2	34.0	0.4	19.0	15.0	3.160E-03	3.5237	2.3286	4.53	0.047
	Own data layer 3	32.0	0.4	19.5	15.0	3.160E-03	3.5237	2.3286	7.95	0.288
	Own data layer 4									
	Own data layer 5									
	Own data Bank Toe			19.5					7.95	0.288
NF110	R5 Insitu	32.5	0.4	18.3	15.0	1.745E-03	3.5237	2.3286	10.21	0.235
	R4 Insitu	31.5	31.5	19.4	15.0	1.708E-06	1.4962	1.2531	6.37	0.346
	R4 Talus	31.5	0.4	19.4	15.0	1.745E-03	3.5237	2.3286	0.39	3.484
	R3 Insitu	33.0	13.6	19.0	15.0	5.064E-06	0.6577	1.6788	4.57	0.456
	Own data layer 5									
	Own data Bank Toe			19.4					7.39	0.306
NF125	R3	34.0	0.4	19.5	15.0	1.745E-03	3.5237	2.3286	32.08	0.091
	R2 Insitu	34.0	0.4	19.5	15.0	1.745E-03	3.5237	2.3286	32.08	0.091
	R2 Clay	34.0	14.2	20.0	15.0	1.708E-06	1.4962	1.2531	5.00	0.423
	R2 Talus	34.0	0.4	20.0	15.0	1.745E-03	3.5237	2.3286	15.05	0.170
	R2 Toe	34.0	0.4	20.0	15.0	1.745E-03	3.5237	2.3286	15.05	0.170
	Own data Bank Toe			20.0					8.88	0.263
NF300	Own data layer 1	35.0	0.4	19.5	15.0	1.745E-03	3.5237	2.3286	7.78	0.294
	Own data layer 2	35.0	0.4	19.5	15.0	1.745E-03	3.5237	2.3286	7.78	0.294
	Own data layer 3	35.0	0.4	19.5	15.0	1.745E-03	3.5237	2.3286	5.36	0.273
	Own data layer 4									
	Own data layer 5									
	Own data Bank Toe			19.5					5.20	0.273
NF310	R4 IS	35.5	9.3	18.0	15.0	1.130E-06	4.0563	2.3286	0.78	1.965
	R4 T	35.5	0.0	18.0	15.0	1.745E-03	3.5237	2.3286	6.01	0.363
	R3	35.0	7.7	19.0	15.0	1.130E-06	4.0563	2.3286	14.31	0.177
	R2	35.0	0.0	18.5	15.0	1.745E-03	3.5237	2.3286	14.33	0.177
	Own data layer 5									
	Own data Bank Toe			19.0					10.43	0.230
NF350	L IS	35.0	34.9	19.0	15.0	9.473E-07	1.5812	1.4158	3.50	0.568
	L T	35.0	0.0	19.0	15.0	3.160E-03	3.5237	2.3286	3.50	0.569
	Own data Bank Toe			19.0					7.57	0.300
NF375	R2 IS	27.8	0.0	19.0	15.0	3.160E-03	3.5237	2.3286	3.01	0.644
	R2 T	27.8	0.0	17.8	15.0	3.160E-03	3.5237	2.3286	14.09	0.180
	R1 Toe	20.0	0.0	17.8	15.0	3.160E-03	3.5237	2.3286	16.31	0.159
	Own data Bank Toe			17.8					13.70	0.184

8.2 Model Calibration

Selection of the calibration period was based on: (1) having limited to no bed erosion over the period, and (2) that the period was bounded by cross-section surveys. Simulation results for the calibration period were compared to the surveyed bank geometry at the end of the calibration period. In most cases, mass failure and bank retreat in these non-cohesive sediments is largely controlled by hydraulic erosion of the bank-toe materials. Initial simulations, however, showed minimal hydraulic erosion and, therefore, very limited bank erosion. To overcome this problem, we identified that perhaps the critical shear stress could be adjusted to account for the lower specific gravity of the bank-toe materials. This has been described in an earlier section of the report. After applying the adjustment of the critical shear stress for lower specific gravity, simulation results showed hydraulic erosion and undercutting and, substantial bank erosion and retreat. Initial and modified values of τ_c based on weighting Equation 24 and applied to Equation 8 are shown in Table 19.

Table 19. Initial and adjusted values of critical shear stress based on weighted values of specific gravity (See Equations 8 and 24).

Channel	Site	Initial τ_c (Pa)	Modified τ_c based on specific gravity adjustment (Pa)
Castle Creek	CA230	7.8	5.1
Coldwater Creek	CW280	17.0	10.6
Loowit	LO100	8.0	7.8
Loowit	LO32	11.4	7.3
Loowit	LO33	4.2	2.8
Loowit	LO40	14.6	9.2
North Fork Toutle	NF105	13.6	8.4
North Fork Toutle	NF110	14.3	8.8
North Fork Toutle	NF125	25.3	15.1
North Fork Toutle	NF300	8.5	5.4
North Fork Toutle	NF310	57.4	33.7
North Fork Toutle	NF350	11.9	7.6
North Fork Toutle	NF375	26.7	16.3
Truman	TR100	16.5	10.3
Truman	TR65	12.8	8.1

Since bank-toe resistance to hydraulic erosion is a function of the particle size and adjusted weight of bank-toe materials, and discharge is an independent variable, Manning's *n* was then used as the calibration parameter. The normal depth calculations were conducted at the selected *n*-value to obtain a stage-discharge relation. If the first calibration run did not produce a model output similar to that of the surveyed channel geometry, another *n*-value was selected, a new stage-discharge relation determined, and BSTEM-Dynamic re-run with the new *n*-value. This process was repeated iteratively with reasonable values of *n* until the simulated geometry approached the surveyed geometry at the end of the calibration period. Table 20 provides a summary of the locations and final values used at each site for model calibration. Figure 41 provides example calibration results for two sites on the UNFT main stem and one on Coldwater Creek.

Table 20. Summary of calibration runs with BSTEM-Dynamic 1.0.

Channel	Site	Bank Modeled	Roughness Modeled	Calibration Period
Castle Creek	CA230	RB	0.0590	2007 - 2010
Coldwater Creek	CW280	LB	0.0350	1985 - 1986
Loowit	LO100	RB	0.0399	2007 - 2010
Loowit	LO32	LB	0.0600	2007 - 2010
Loowit	LO33	LB	0.0650	2007 - 2010
Loowit	LO40	LB	0.0305	2007 - 2010
North Fork Toutle	NF105	LB	0.0650	2007 - 2010
North Fork Toutle	NF110	RB	0.0550	2007 - 2010
North Fork Toutle	NF125	RB	0.0325	2007 - 2010
North Fork Toutle	NF300	RB	0.0450	2007 - 2010
North Fork Toutle	NF310	RB	0.0300	2006 - 2010
North Fork Toutle	NF350	LB	0.0400	-
North Fork Toutle	NF375	RB	0.0300	-
Truman	TR100	RB	0.0600	2007 - 2010
Truman	TR65	LB	0.0550	2007 - 2010

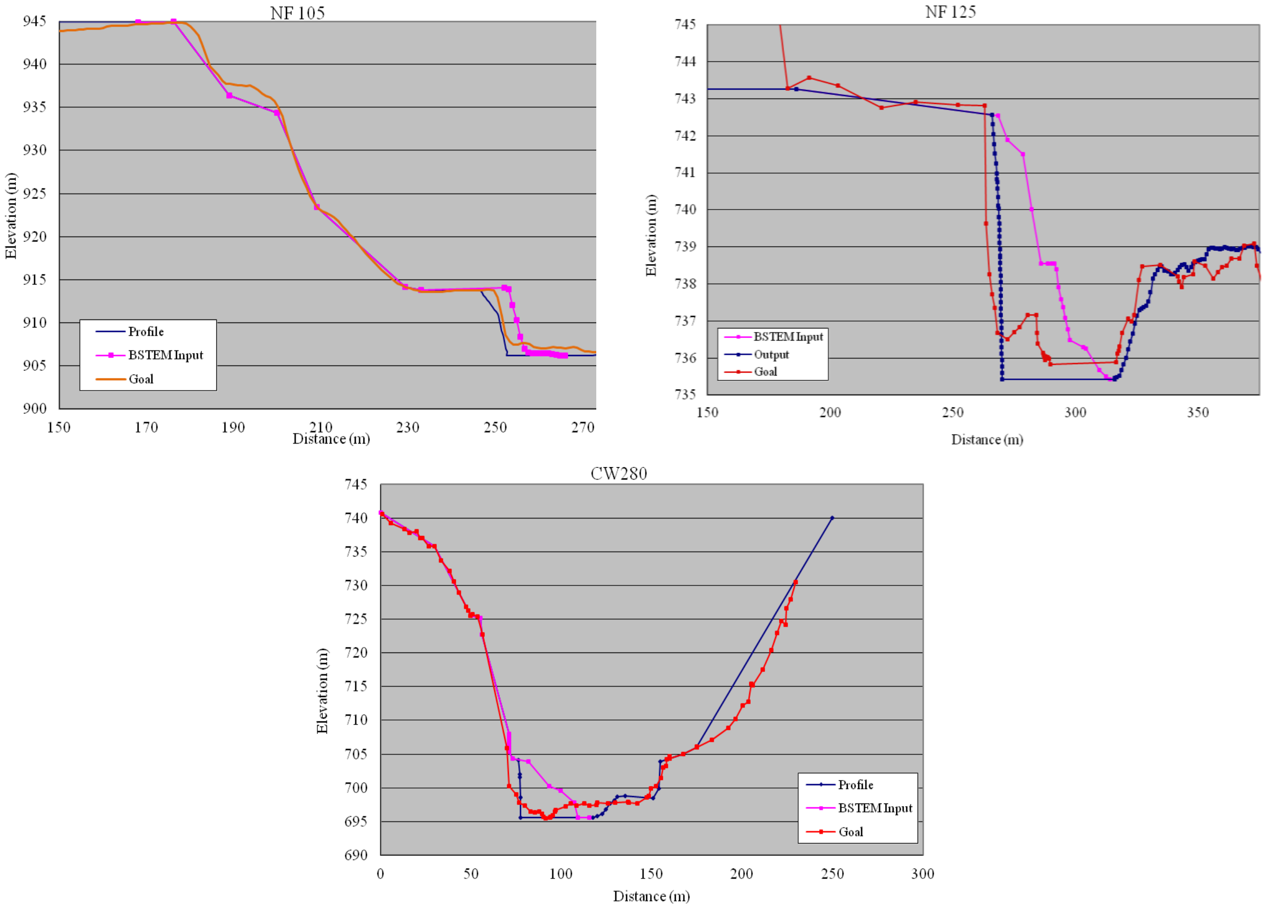

Figure 41. Calibration results for NF 105 (top left), NF 125 (top right) and CW 280 (bottom).

8.3 Flow Series for Simulations of Future Bank-Erosion (2010-2110)

The flow period used to develop a 100-year flow series was determined through discussion and agreement with the Corps of Engineers to be representative of current hydrologic conditions in the UNFT. By this it is meant that drainage integration throughout the debris avalanche deposit is complete, flows from Spirit Lake are not augmented by pumping, and the SRS, being filled, is no longer serving as a dam. The 15-year flow period selected was October 1, 1995 – September 30, 2010 given that the first spillway flow occurred in October 1995.

The relation between mean-daily flow and drainage area is somewhat complex due to the non-contributing portion that includes Spirit Lake. However, a certain amount of flow is discharged from the lake. Mean-daily discharge values emanating from the lake were provided in tabular form by the Portland District U.S. Army Corps of Engineers, pers. comm., (2011) (Figure 42).

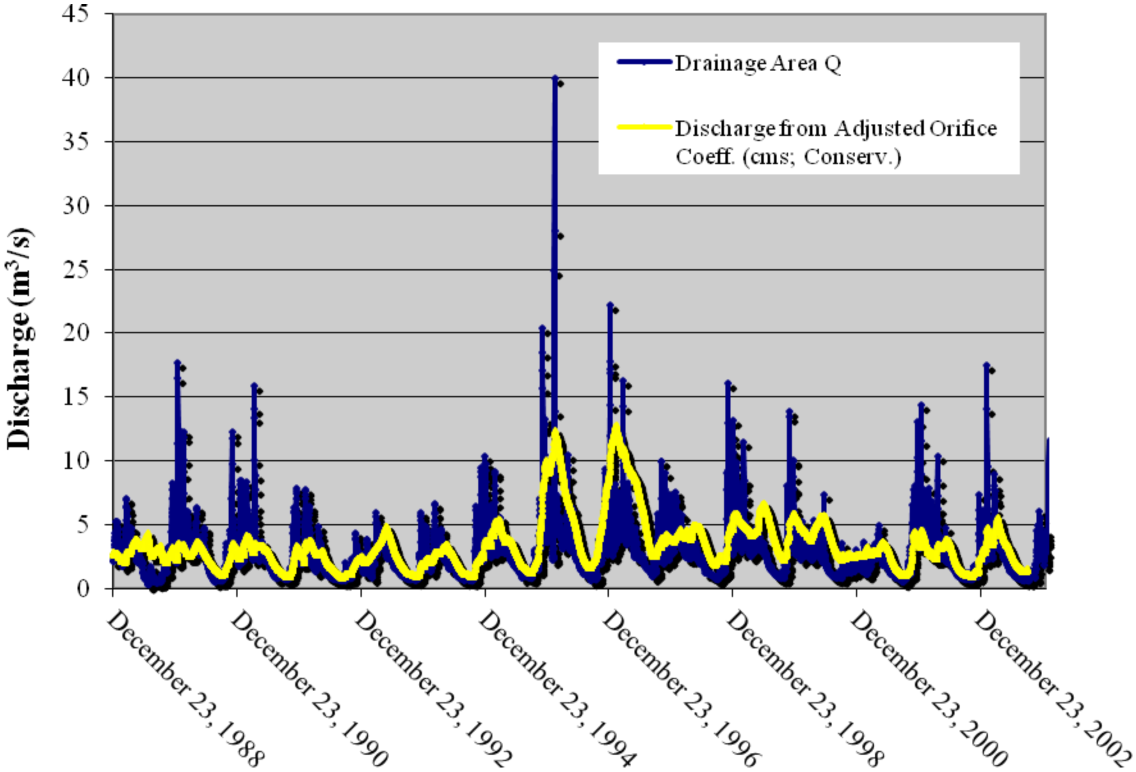

Figure 42. Example of discharge from Spirit Lake. Blue trace represents discharge based on drainage area. Yellow trace is discharge provided by U.S. Army Corps of Engineers, pers. comm., (2011) and used for calculation of downstream flows.

Adjustments to mean-daily discharge values at a particular modeled cross section were then calculated using the following equations:

$$DA_{SRS-Lake} = DA_{SRS} - DA_{Spirit\ Lake} \tag{27a}$$

$$DA_{Site-Lake} = DA_{Site} - DA_{Spirit\ Lake} \tag{27b}$$

$$Q_{Site.ADJ} = Q * (DA_{Site-Lake} / DA_{SRS-Lake}) + Q_{Lake} \tag{27c}$$

The result of this adjustment to the initial flow series was that peaks were greatly reduced and base flows were slightly raised at the upstream-most sites (Figure 43; top).This affect of course was attenuated with distance downstream and the associated increase in drainage area (Figure 43; bottom).

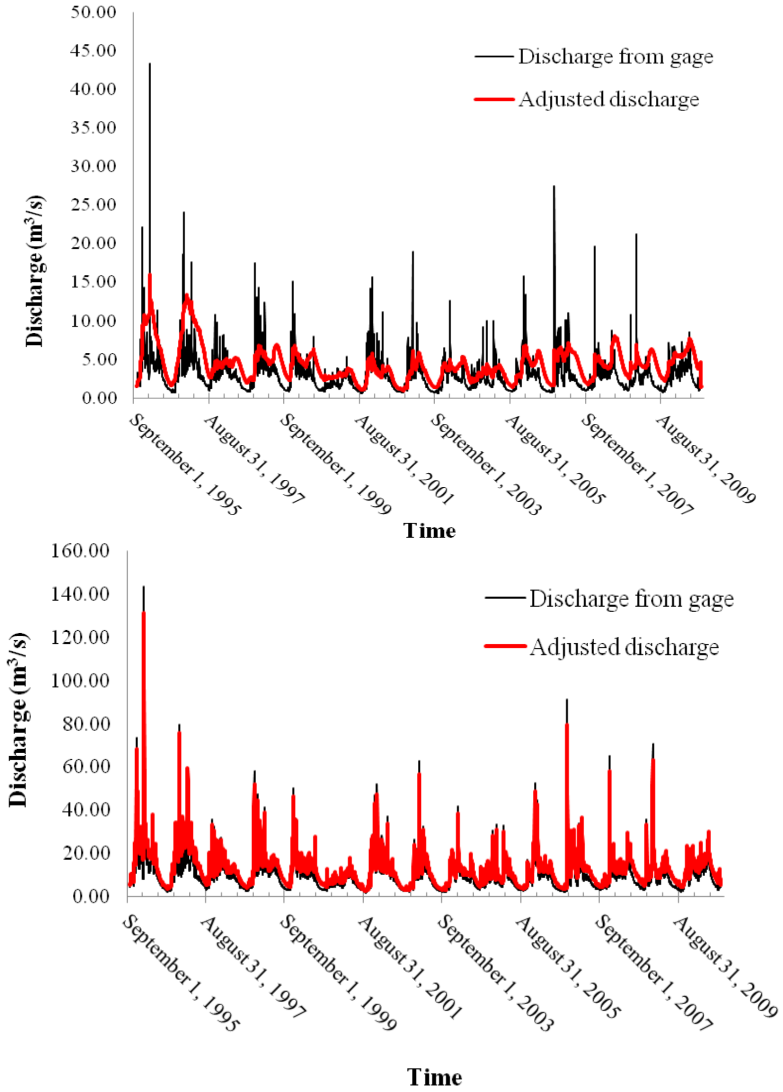

Figure 43. Example comparison of 15-year flow series of discharge values generated for TR 65 (top) and NF300 (bottom) based solely on drainage area ratio (black trace; which includes Spirit Lake) with calculated discharge values for the sites (red trace) using the equations provided by the Portland District USACE, 2011, pers. comm.

The resulting mean-daily flows were repeated seven times with the last five years of the 7th iteration truncated to provide a 100-year flow series. It should also be pointed out that the simulation period includes an *extreme* non-hydrologic event (November 2006) that was repeated seven times. This flow, discussed in detail in an earlier section of the report, was greatly enhanced by the suspected breach of a debris dam on Loowit channel. As a final note to the flow series, the flow of February 1996 was the largest post-eruption flow on record (Table 6). This event was also repeated seven times and had implications for modeling results.

8.4 Results of 100-Year Simulations

In total, 15 sites were modeled using BSTEM-Dynamic 1.0. The initial cross-section geometry used corresponded to the last ground survey conducted by the USDA-ARS during the field seasons of 2009 and 2010. A summary of the range of flow conditions and Manning's *n* used in the 100-year simulations is provided in Table 21.

Model simulations were conducted for the most currently active bank (left or right) in the cross section. Examples of simulated bank erosion and retreat from two typical cross sections (NF110 and CW280) are shown in Figures 44 and 45. The bottom plot of each of these figures is a magnified version of the upper plot. The reduction in retreat rates can clearly be seen in the two examples provided. Given that the 100-year simulations are driven by seven sets of identical data, changes in the rate of retreat as observed in Figures 44 and 45 must, therefore, be a function of the reduction in the ability of the flows to undermine bank-toe regions. With the input critical shear stresses remaining constant through the course of the simulation, the reduction in erosion rates is related to the reduction in shear stress for a given discharge as the channel widens. This was the process that was initially hypothesized as the cause of non-linear decay in erosion rates.

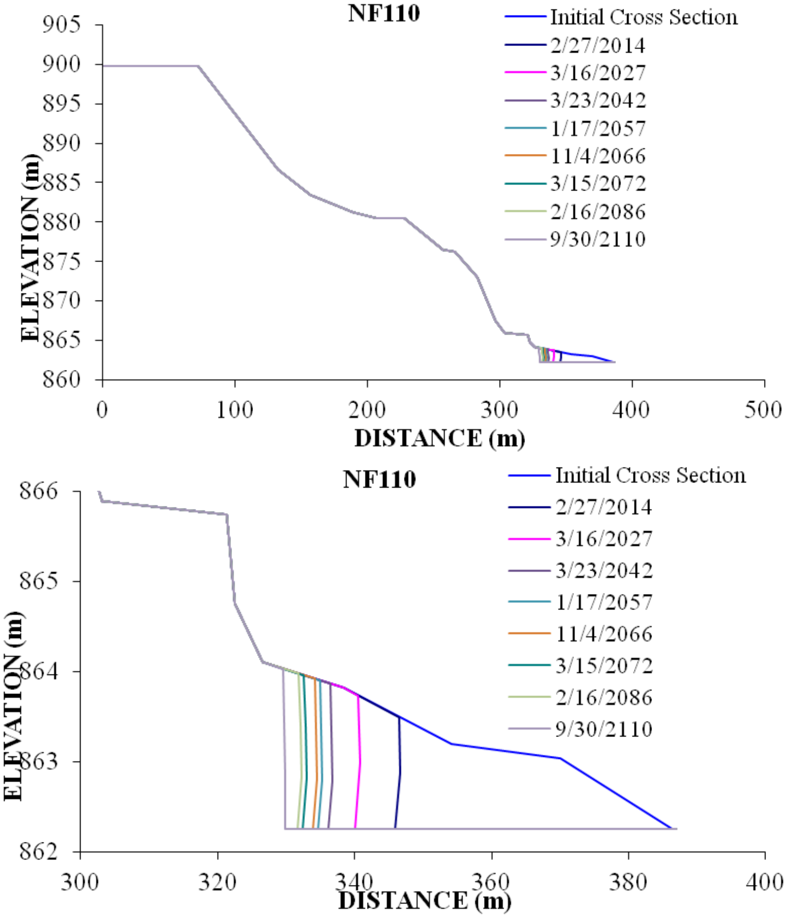

Figure 44. Time-series bank erosion as modeled by BSTEM-Dynamic 1.0 at NF110. Bottom plot represents magnified version of the upper plot.

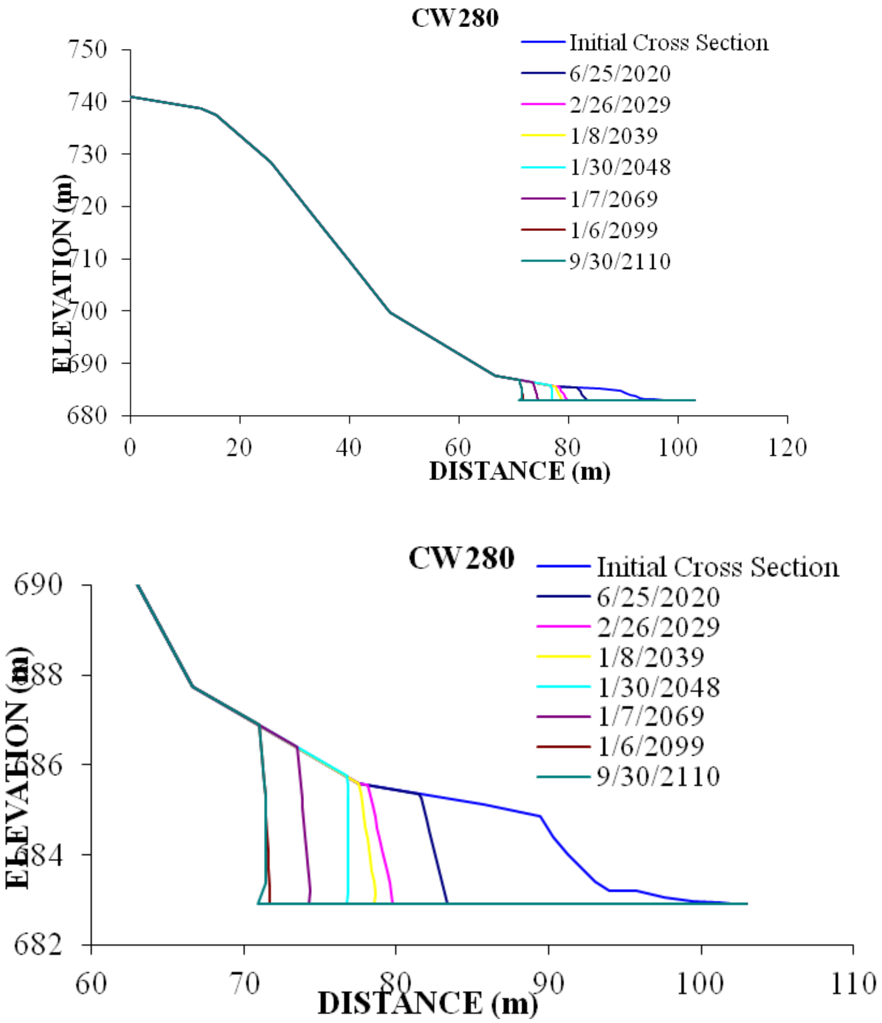

Figure 45. Time-series bank erosion as modeled by BSTEM-Dynamic 1.0 at CW280. Bottom plot represents magnified version of the upper plot.

As modeling results pertain to only one bank, an estimate of the amount of erosion on the opposite bank had to be determined to compare results with empirically derived values. This was accomplished in two ways: (1) The modeled value for each site (in m^2) was multiplied by 2.0 and, (2) The modeled value was multiplied by one minus the ratio between the empirically-derived eroded area for the modeled bank and the total area of eroded banks (left and right). These approaches were considered potentially applicable based on the premise that the braided channels of the UNFT frequently avulse from one side of the valley to other in response to high-flow events. The bank that tends to erode during a given period is the one that has the flow impacting its base. Method 1 assumes that the flow spends roughly an equal amount of time on each side of the valley. Method 2 is an attempt to discern the difference in the magnitude and duration in which flows impact each bank. Results for both methods of estimating total bank erosion in each cross section, along with the empirically-derived values of bank erosion are shown in Table 22.

Table 21. Summary of 100-year flow conditions for each of the 15 modeled sites.

Channel	Site	Distance above SRS (km)	Bank Modeled	Next site downstream for extrapolation	Minimum Q (m^3/s)	Maximum Q (m^3/s)	Minimum stage (m)	Maximum stage (m)	Roughness
Castle Creek	CA230	33.72	RB	NF300	0.06	4.5	0.19	0.74	0.059
Coldwater Creek	CW280	34.37	LB	NF300	0.52	38.7	0.18	1.29	0.035
Loowit	LO100	42.94	LB	NF105	0.14	10.6	0.06	0.43	0.040
Loowit	LO32	46.46	RB	LO33	0.06	4.5	0.06	0.47	0.06
Loowit	LO33	45.15	LB	LO40	0.12	9.2	0.06	0.54	0.065
Loowit	LO40	44.92	LB	LO100	0.13	9.4	0.1	0.42	0.0305
North Fork Toutle	NF105	42.24	LB	NF110	1.2	30.3	0.16	0.84	0.065
North Fork Toutle	NF110	40.83	RB	NF125	1.25	33.4	0.29	1.01	0.055
North Fork Toutle	NF125	36.72	RB	NF300	1.54	50.5	0.19	0.96	0.0325
North Fork Toutle	NF300	31.38	RB	NF310	2.66	131	2.51	3.79	0.045
North Fork Toutle	NF310	28.21	RB	NF350	2.93	151	0.43	1.48	0.03
North Fork Toutle	NF350	22.68	LB	NF375	2.37	178	0.28	1.46	0.04
North Fork Toutle	NF375	17.52	RB	N-1	3.3	178	0.35	1.22	0.03
Truman	TR100	43.04	RB	NF105	0.98	17.4	0.28	1.16	0.06

Table 22. Comparison of two methods of extrapolating modeled areas of bank erosion to the opposite bank. Note [1] and [2] represent Method 1 and Method 2, respectively.

Channel	**Site**	**Simulated area eroded (m^2)**	**Simulated area eroded doubled[1] (m^2)**	**% Difference (simulated vs. empirical)[1]**	**Simulated area eroded times multiplier[2] (m^2)**	**% Difference (simulated vs. empirical)[2]**	**Empirical area eroded (both banks) (m^2)**
Castle Creek	CA230	372	745	-19%	424	-54%	919
Coldwater Creek	CW280	54.2	108	-74%	69	-83%	414
Loowit	LO32	3.3	7	-99%	6	-99%	555
Loowit	LO33	156	312	-63%	368	-56%	841
Loowit	LO40	41.4	83	-86%	63	-89%	599
Loowit	LO100	397	795	-67%	1692	-31%	2441
North Fork Toutle	NF105	105	209	-85%	141	-90%	1395
North Fork Toutle	NF110	54.1	108	144%	116	163%	44
North Fork Toutle	NF125	817	1634	-9%	3666	104%	1793
North Fork Toutle	NF300	1366	2732	5%	2668	3%	2598
North Fork Toutle	NF310	2923	5846	-6%	5162	-17.2%	6234
North Fork Toutle	NF350	257	513	-73%	1054	-46%	1937
North Fork Toutle	NF375	520	1040	-23%	526	-61%	1354
Truman	TR65	447	894	14%	1036	32%	786
Truman	TR100	463	925	128%	885	118%	406
Sum			**15951**		**17876**		**22315**
Average				**-21%**		**-14%**	

The empirical values were determined by subtracting the total empirically-predicted bank erosion in 2110 from those predicted in 2010. Results are shown plotted by river kilometer in Figure 46 and for the most part, show reasonably good agreement with the empirical estimates. Both methods of extrapolating from one bank to the entire cross section are generally lower than the empirically-derived values; 21% and 14% respectively (Table 22). These averages do not imply that BSTEM-predicted erosion is 14-21% less than that derived empirically, as the results shown in Table 22 must next be extrapolated over the reach lengths between individual cross sections to obtain estimates of eroded volumes. Further, the sum of the eroded areas for each site shows that Method 2 is 20% less than the empirical values as compared to 29% less than for Method 1. Based on these results, we employed Method 2 for calculations of total volumes of bank erosion over the 100 years simulated.

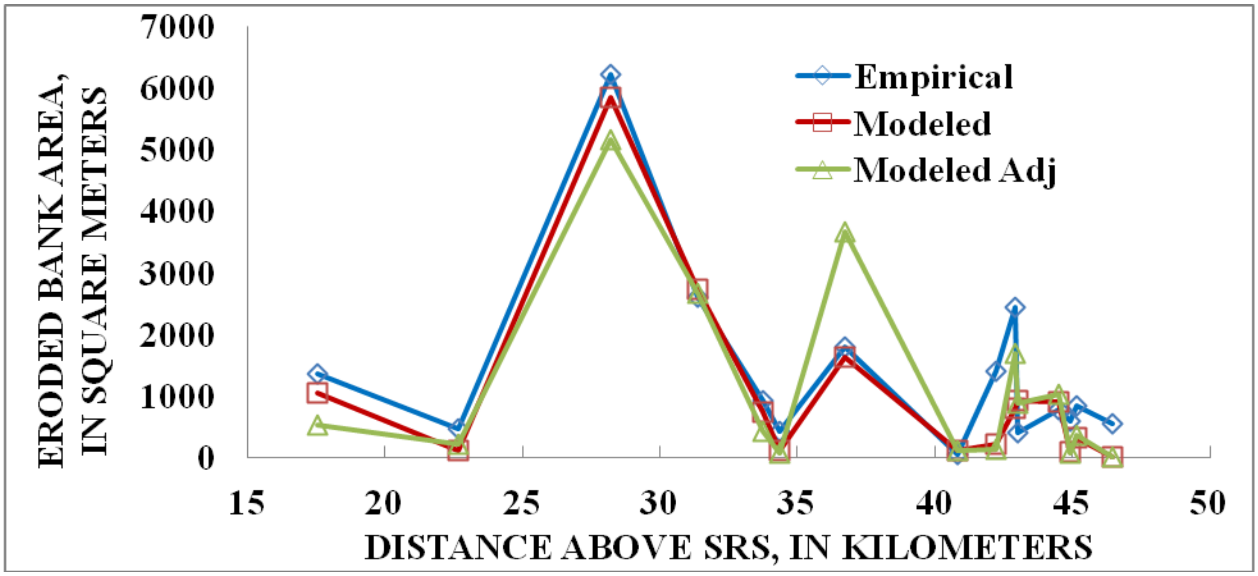

Figure 46. Comparison of two-bank eroded areas; Method 1 of multiplying eroded area of modeled bank by 2.0 is shown in red. Method 2 of multiplying eroded area of modeled bank by 1 minus the ratio of the one-bank eroded area to total bank erosion is shown in green.

Simulated values of bank erosion (for both banks) at the cross sections ranged from 6 m^2 at LO32 to about 3,670 m^2 at NF125, with an average modeled value of bank erosion of 1,053 m^2 over the next century. Empirically-derived total bank-erosion areas for the modeled sites was roughly 22,300 m^2 compared to about 17,900 m^2 predicted by BSTEM-Dynamic 1.0 using Method 2 to extrapolate eroded areas to the opposite bank. The low predicted value of erosion for LO32 is curious given the scale of the canyon at this location. The site experienced significant incision during the extreme November 2006 event with about 550 m^2 being eroded from the bed and about twice that from the banks. Ground surveys subsequent to this event (the last being in September 2009) show mild bed aggradation and some channel narrowing, possibly due to the over-widened cross section resulting in a loss of transport capacity. Thus, available shear stresses provided by the 100-year flow series are insufficient to undercut bank toes and lead to mass failure. LO30, located 1.5 km upstream also shows little evidence of continued incision and widening, indicating that the reach between LO32 and LO30 may mark the upstream limit of significant channel erosion.

In general, geotechnical failure of *in situ* debris avalanche deposits made up the bulk of the eroded material. Hydraulic erosion, although persistent, represented a relatively small component of the total amount of bank erosion. This is typical of many unstable alluvial channels, particularly those composed of non-cohesive materials, where hydraulic undercutting of toe materials may be the primary driver (although not the primary source) of bank erosion and retreat.

Peaks in bank-erosion rates appeared to occur roughly every 15 years (Figure 47). This is the combined result of (1) repeating the February 1996 flow every 15 years as part of the generated flow series, and (2) another wet flow year (originally 1997) followed immediately thereafter. Thus, failures in the first two years of each 15-year period served to somewhat flatten bankslopes as well as to reduce applied shear stresses for successive years within each 15-year period. It is no surprise, therefore, that erosion rates for the last 13 years of each 15-year period are limited. The parallel retreat depicted in Figures 44 and 45 demonstrates a limitation of BSTEM in dynamic mode once a failure is simulated. The slope angle of retreat represents the most critical failure-plane angle as determined by the search routine in BSTEM. Because BSTEM is not a sediment-routing model, the failed material is not stored at the toe of the bank but is assumed to be removed from the cross section and delivered to the flow. Still, attenuation of erosion rates is again indicated by the non-linear reduction in the peak rates, pointing to the episodic nature of bank-failure processes, as well as the effect of widening on reduction in applied shear stresses and hence, erosion rates, with time.

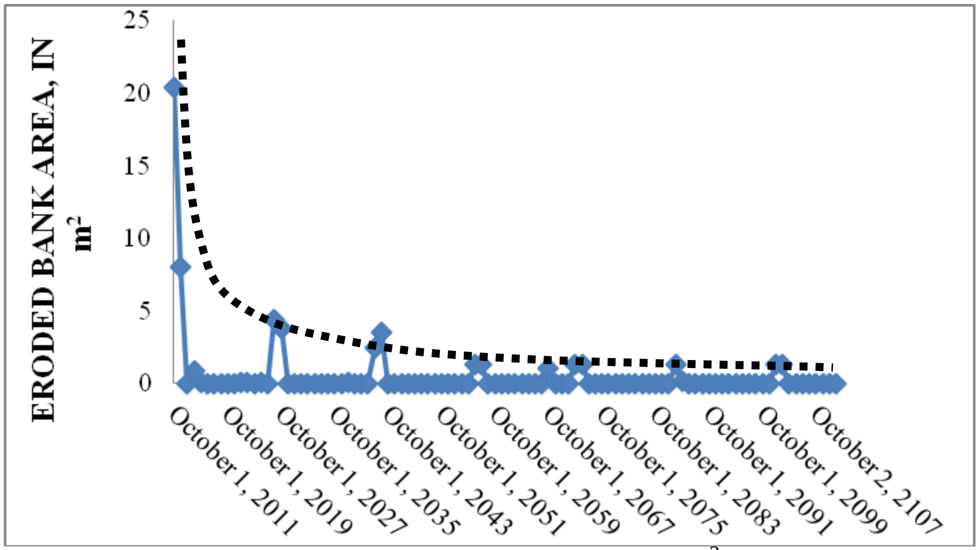

Figure 47. Annual rates of bank erosion at NF110 expressed in m^2 (one bank). Note the hypothesized non-linear attenuation of peak, bank-erosion rates.

8.5 Trend and Magnitude of Total Erosion from Banks and Terraces

To obtain values of total erosion, the two-bank eroded areas from the individual cross sections were extrapolated to adjacent reaches. Using the eroded-area results (in m^2) of the 100-year simulations at individual cross-section locations, eroded volumes were calculated by multiplying by the distance between cross sections. Specifically the eroded area at a specific cross section was multiplied by the distance (in m) between that section and the next section downstream. For the reach between the N-1 structure and NF375, the eroded area at NF375 was multiplied by the distance to the N-1 structure. For the downstream-most tributary sites such as CW280, the eroded area at the site was multiplied by the distance of the entire channel length. For un-modeled tributary reaches upstream of the last modeled site, the empirically derived eroded area from the site was used.

Volumes of erosion from the modeled reaches for the next century range from 7.5×10^3 m^3 at LO32 to 31.2×10^6 m^3 at NF125 (Figure 48). The longitudinal trend is somewhat misleading as eroded areas from a given cross section have been multiplied by different reach lengths. It can be seen, however, that predicted bank and terrace erosion from (1) along the UNFT between NF310 to NF125 (rkm 28.2 – 36.7) will remain high, and (2) decrease markedly upstream from LO40. The latter reach is the one heavily impacted by the purported debris-dam failure causing 10.2 to 17.3 m of erosion during the high flows of November 2006. For example, as much bank and terrace erosion occurred at LO40 during and in the aftermath of the November 2006 flows as occurred from 1980-2005 (about 740 m^2). This is typical of the reach. The result of these large, rapid changes was a much wider stream bed where post-event shear stresses are largely insufficient to undercut bank toes. In addition, coarse particle sizes at the bank toe tend to resist rapid undercutting and lateral retreat. It remains to be seen if a future *extreme* event will re-incise the reach and de-stabilize the terrace slopes. Given that this reach has been aggradational since the November 2006 event and knickpoints are located upstream of this reach, it appears that re-activation of the reach may be very infrequent.

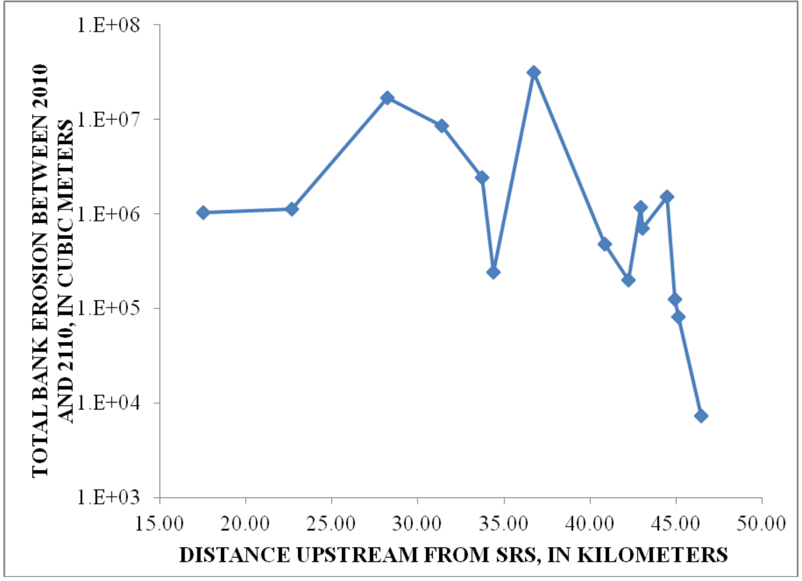

Figure 48. Distribution of erosion volumes by reach. Note: eroded areas for a given site have been multiplied by different reach lengths.

8.6 Comparison between Simulated and Empirically-Derived Erosion Volumes for Modeled Reaches

By comparing simulated erosion volumes with the empirically-derived volumes over just the modeled reaches, we can obtain a better understanding of how these two approaches differ. Figure 49 shows the temporal trends of the data for both approaches. Bank- and terrace-erosion volumes for the reaches simulated with BSTEM-Dynamic between N-1 and LO32, and from the confluence of Loowit and Truman Channel to TR65 decay non-linearly with time (Figure 49). Erosion rates calculated from the 100-year simulations and extrapolated between modeled sites gives 77.3 x 10^6 m^3 (100 x 10^6 yd^3) of erosion compared to 74.4 x 10^6 m^3 (97.3 x 10^6 yd^3) for the empirically-derived values, 3.9% more. These data are re-plotted in Figure 49 (right) using the 2010 empirically-derived value for banks as a starting point to show total bank and terrace erosion since 1980. Simulation results predict a total of 287 x 10^6 m^3 (376 x 10^6 yd^3) of banks and terraces eroded in the reaches since 1980. The estimates differ by 2.87 x 10^6 m^3 (3.75 x 10^6 yd^3), about 1.0% higher than the empirically-derived value of 284 x 10^6 m^3 (37.1 x 10^7 yd^3). The similarity of the 100-year calculations is encouraging in support of the hypothesis of non-linear decay in bank-erosion rates.

It is interesting to consider the difference in the general trend of the 100-year empirical and modeling estimates. Whereas the empirical calculations are based on extrapolation of a logarithmic regression of measured bank-erosion rates and show a smooth non-linear decay, the modeled decay in erosion rates is much faster initially and then shows the typical stair-step appearance that characterizes the episodic nature of bank and terrace erosion (Figure 49). Still, the estimates of future bank and terrace erosion using the two approaches are exceptionally close given the completely different methods used to obtain the values. Clearly, both methods show trends of non-linear decay.

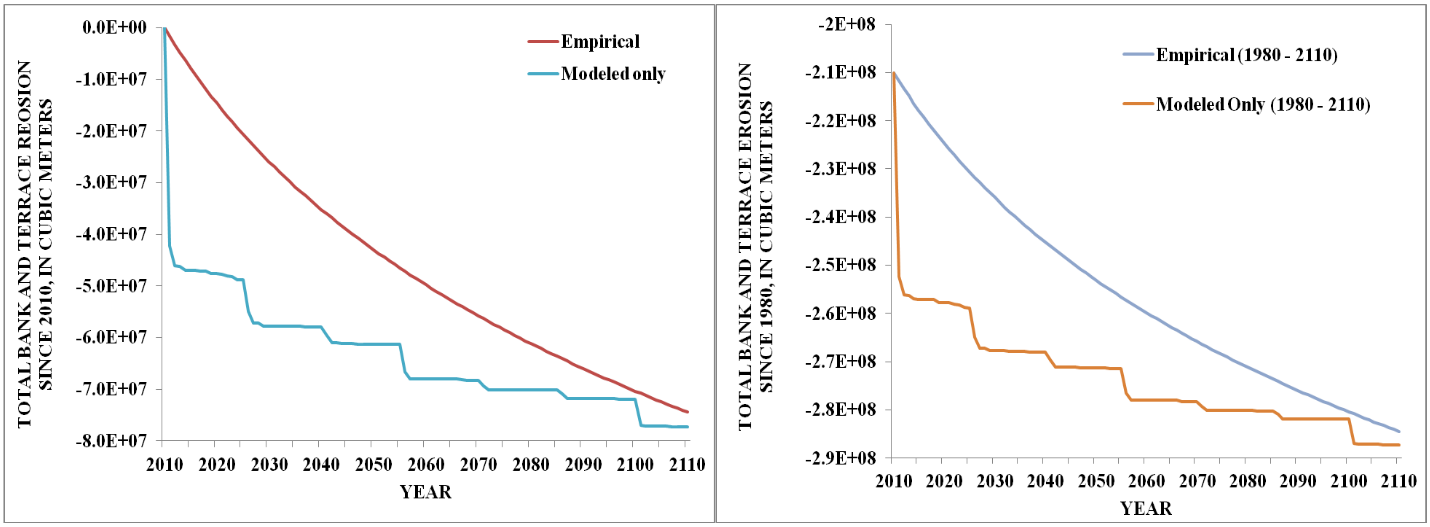

Figure 49. Comparison of modeled and empirically-derived annual, bank-erosion volumes for modeled reaches of the UNFT from 2010 to 2110. Erosion volume between 2010 and 2110 (left) Erosion volume 1980-2010 (right).

8.7 Comparison between Simulated and Empirically-Derived Erosion Volumes for UNFT

Bank- and terrace-erosion volumes for the entire UNFT basin, including non-modeled reaches, are determined by combining simulation results from modeled reaches with estimates of what BSTEM-Dynamic would have predicted in other reaches. To compare modeled and empirical results, and to determine erosion volumes for the entire UNFT (including the non-modeled reaches) data from the non-modeled reaches needed to be added to the modeled results. Given that the average, modeled results at each cross section were, on average, roughly 20% less than the empirically-derived bank-erosion values, estimates of future erosion from the non-modeled reaches were added to modeled data at 80% of those calculated empirically.

Erosion volumes derived from simulated erosion areas plus estimated values from the un-modeled reaches are shown overlain with the empirically-derived values, for the UNFT (Figure 50). Erosion rates calculated from the 100-year simulations 2010-2110, extrapolated between modeled sites and with un-modeled estimates added, predicts about 78.7 x 10^6 m^3 (103 x 10^6 yd^3) of additional erosion to 2110 compared to 76.7 x 10^6 m^3 (100 x 10^6 yd^3) for the empirically-derived values. Modeled erosion volumes over the UNFT by 2110 are, therefore, about 2.7% more than those predicted empirically.

These data are re-plotted in Figure 50 (right) using the 2010 empirically-derived value (Table 15) as a starting point to obtain cumulative erosion since 1980. Simulation results give a total of 319 x 10^6 m^3 (417 x 10^6 yd^3) of banks and terraces eroded in the reaches since 1980. This value is 0.7% higher than the empirically-derived value of 317 x 10^6 m^3 (415 x 10^6 yd^3).

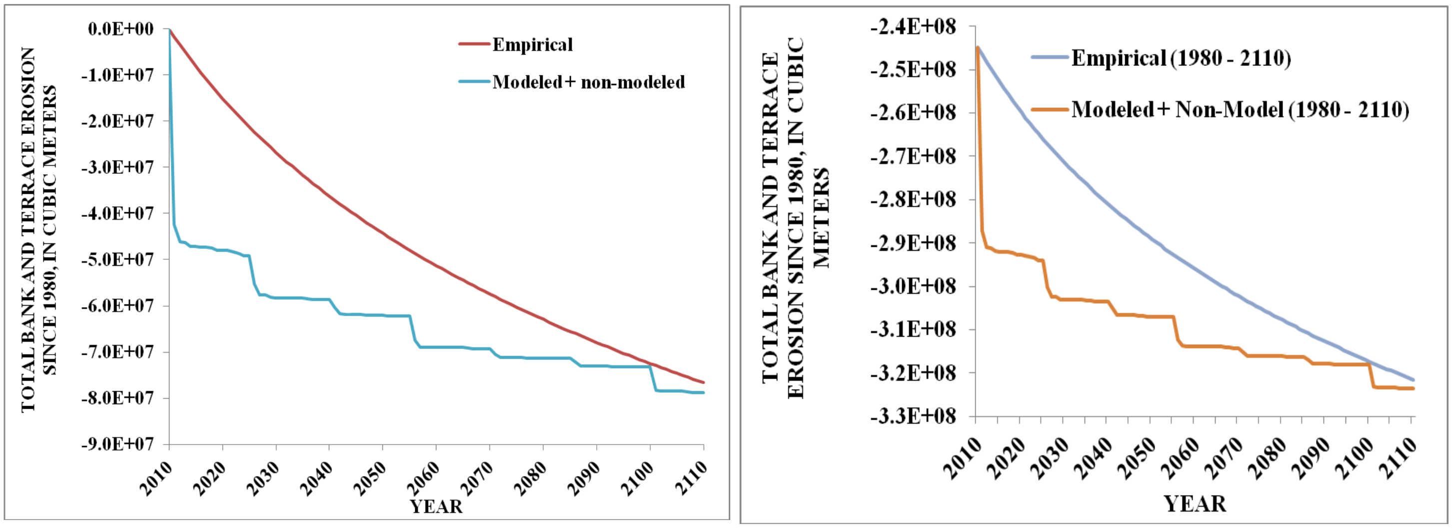

Figure 50. Comparison of modeled and empirically-derived annual, bank-erosion volumes for the UNFT from 2010 to 2110. Erosion volume between 2010 and 2110 (left) Erosion volume 1980-2010 (right).

To place the BSTEM-simulated results in the context of earlier predictions, we first view the simulated, cumulative bank-erosion volumes (in yd^3) with the empirically-derived values for channel beds and banks. Here we have re-created Figure 35, extended the plot to 2110 and added the erosion volumes provided by the simulation analysis described above (Figure 51). Differences between the modeled and empirically-derived bank-erosion values have already been discussed above. The plot, however, serves to further covey that the proportion of eroded materials emanating from streambanks and terraces is significant. According to the empirical calculations, lateral erosion accounts for 82.1% of the total volume and 78.9% based on the modeled values, with the remainder coming from the channel bed.

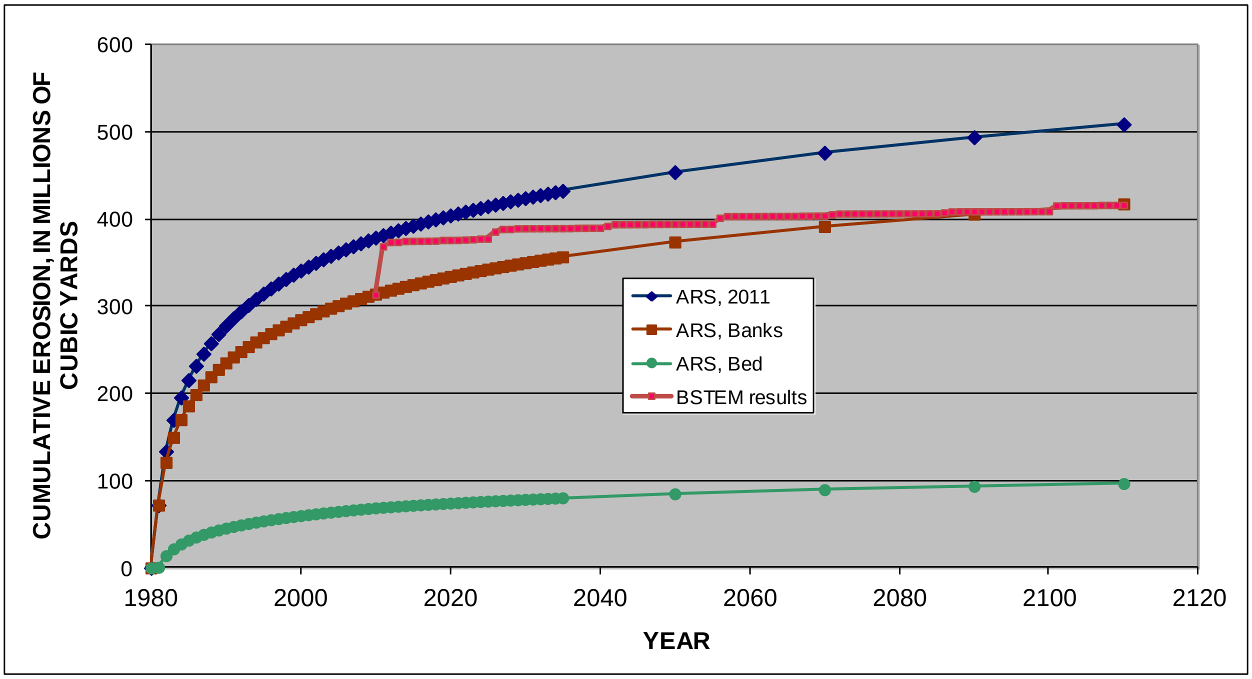

Figure 51. Trends of total erosion for the UNFT showing the empirically-derived contributions from bed, banks and total and, the BSTEM derived contributions from banks and terraces.

Total-erosion estimates, including the empirical values reported here and those documented by Biedenharn *et al*., (2010), are shown together in Figure (52). To bring the BSTEM-simulation results in line with the other two estimates and to estimate total erosion, the bed-material component needed to be added. To accomplish this, empirically-derived bed load data is added to the BSTEM-simulated values for the years 2010-2110. This component, representing about 18% of the total eroded volume between 1980 and 2010 provides the final estimate of total eroded volumes by 2110, to 491 x 10^6 yd^3 (Figure 52). This estimate is 17.8 x 10^6 yd^3 (3.5%) less than the total volume predicted by the empirical method alone for both bed and banks.

Results of dynamic simulation of bank-erosion processes using BSTEM-Dynamic 1.0 have provided results similar to those provided by extrapolating measured changes in channel geometry with time. Although differences between the two methods will increase with time past 2110, there is now parallel evidence that erosion rates from the debris avalanche are decaying. The two estimates provided in this report, one process-based that accounts for roughly 80% of the predicted load (with bed-load component added) and the other, based on temporal extrapolation of time-series series data, are remarkably consistent through the period 2010-2110 . Both estimates do, however, differ considerably from the one documented by Biedenharn *et al*.,

(2010) who use a linear temporal extrapolation of differences in LiDAR surfaces. That study predicted 486 x 10^6 yd^3 of total erosion by 2035.

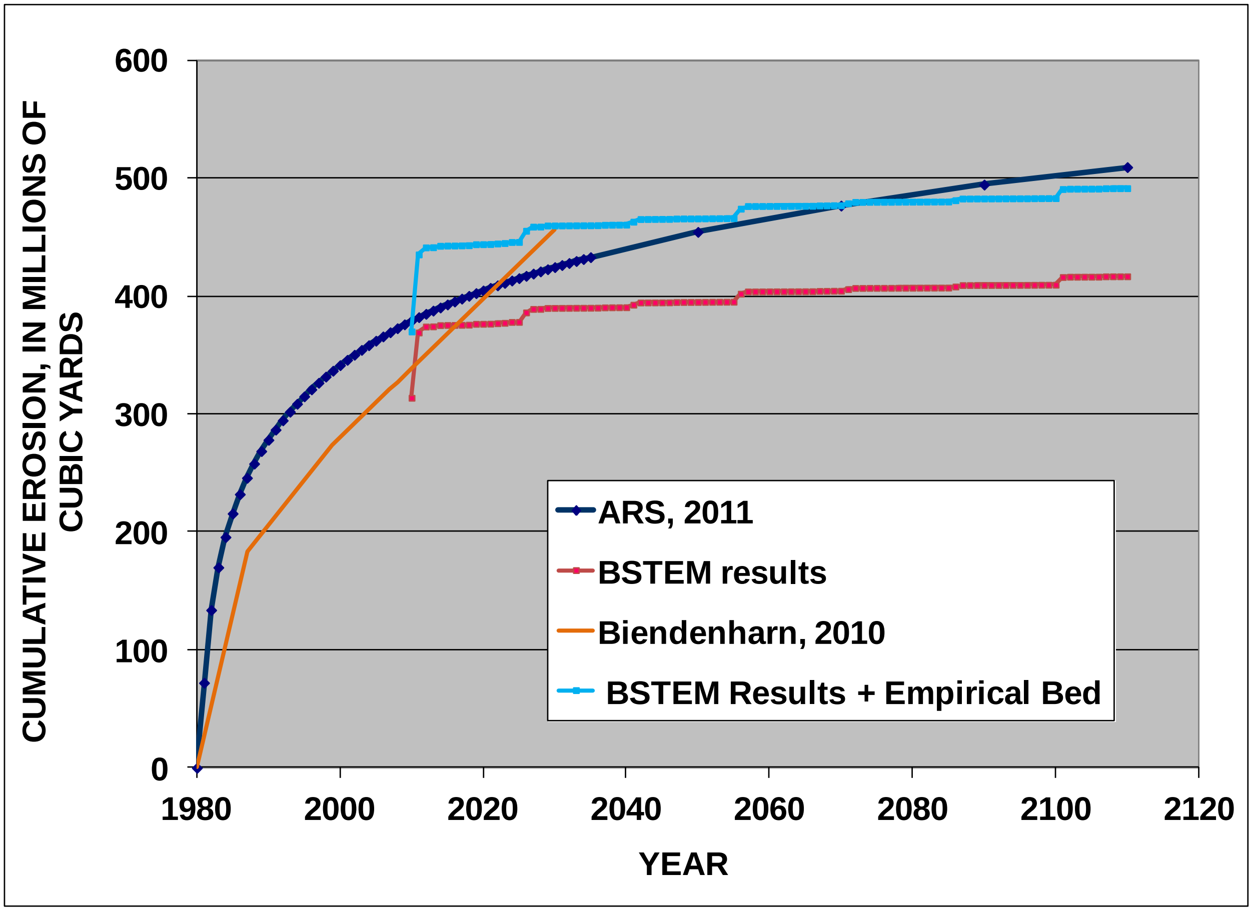

Figure 52. Trends of total, cumulative erosion for the UNFT showing the Biedenharn (2010), ARS-empirical, BSTEM bank-erosion results (red), and the BSTEM results augmented with the empirically-derived values for bed erosion (bright blue).

9. MEASURED AND MODELED PARTICLE SIZE DISTRIBUTIONS

9.1 Measured Particle Size Distributions of *in situ* Bank, Talus, Toe and Bed Braidplain Material.

Measured particle size distributions obtained from field data collection showed that the gravel fraction was dominant in all of the geomorphic surfaces encountered be it *in situ* bank material, bank talus, bank-toe material or the bed braidplain (Table 23; Figure 53). The silt and clay fractions were nominal in all cases. The mean percentage of the boulder and sand fractions did however vary according to location within the valley of the UNFT. In general, the bank toe and bed braidplain material was coarser than the *in situ* bank and talus material. In the case of the toe material which was largely composed of failed bank material, this was likely a result of the winnowing of the finer particle-size fractions by hydraulic action on this lower part of the banks. Similarly on the bed braidplain, hydraulic action has likely removed finer materials, including some of the gravel fractions, leaving a greater percentage of the boulder-size class than is typically found in the *in situ* bank and talus material. The UNFT is probably capable of transporting boulder-sized material during high-flows given the steepeness of the channels and the lower specific gravity of the pumiceous materials.

Table 23. Mean percent occurrence of particle size classes in floodplain material types.

Surface	BOULDER %	GRAVEL %	SAND %	SILT %	CLAY %	D_{50} (mm)
Bank *in situ*	12.1	54.9	27.4	4.3	0.9	17.0
Bank Talus	13.3	58.6	25.5	2.0	0.6	16.3
Toe	34.0	46.4	16.0	2.9	1.2	48.0
Bed	27.5	40.8	26.8	3.1	1.5	26.8

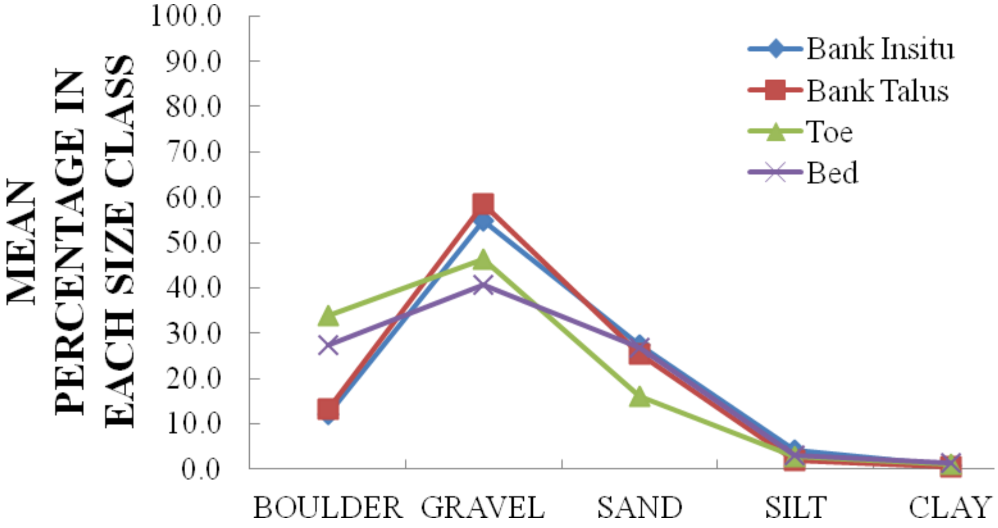

Figure 53. Mean percent occurrence of particle size classes in floodplain material types.

Investigation of the longitudinal trends in d_{50} of the different geomorphic surfaces upstream from the SRS (Figure 54) revealed that the particle-size distributions of the *in situ* bank- and toe-material varied less than the talus and braidplain material. d_{50} for the bank material ranged from 0.358 to 66.8 mm, the toe material similarly ranged from 1.90 to 70.0 mm. d_{50} for the talus ranged from 2.28 to 323 mm and d_{50} for the bed braidplain ranged from 1.90 to 323 mm. Longitudinal trends in the d_{50} of braidplain material in particular have been affected by both hydraulic processes occurring within the channels, and by debris flows and mass-wasting events that have brought additional coarse material to the channels from surrounding slopes. Debris flow events such as that associated with the November 2006 flows may explain, in part, the coarser d_{50} signature found in both the Truman and Loowit channels. This relatively coarser distribution, particularly in Loowit channel may help to explain the reduced amounts of incision and widening upstream of LO33 as shear stresses may be insufficient to entrain bank-toe materials. It can be seen that braidplain d_{50} generally decreases with distance downstream as would be expected in alluvial channels.

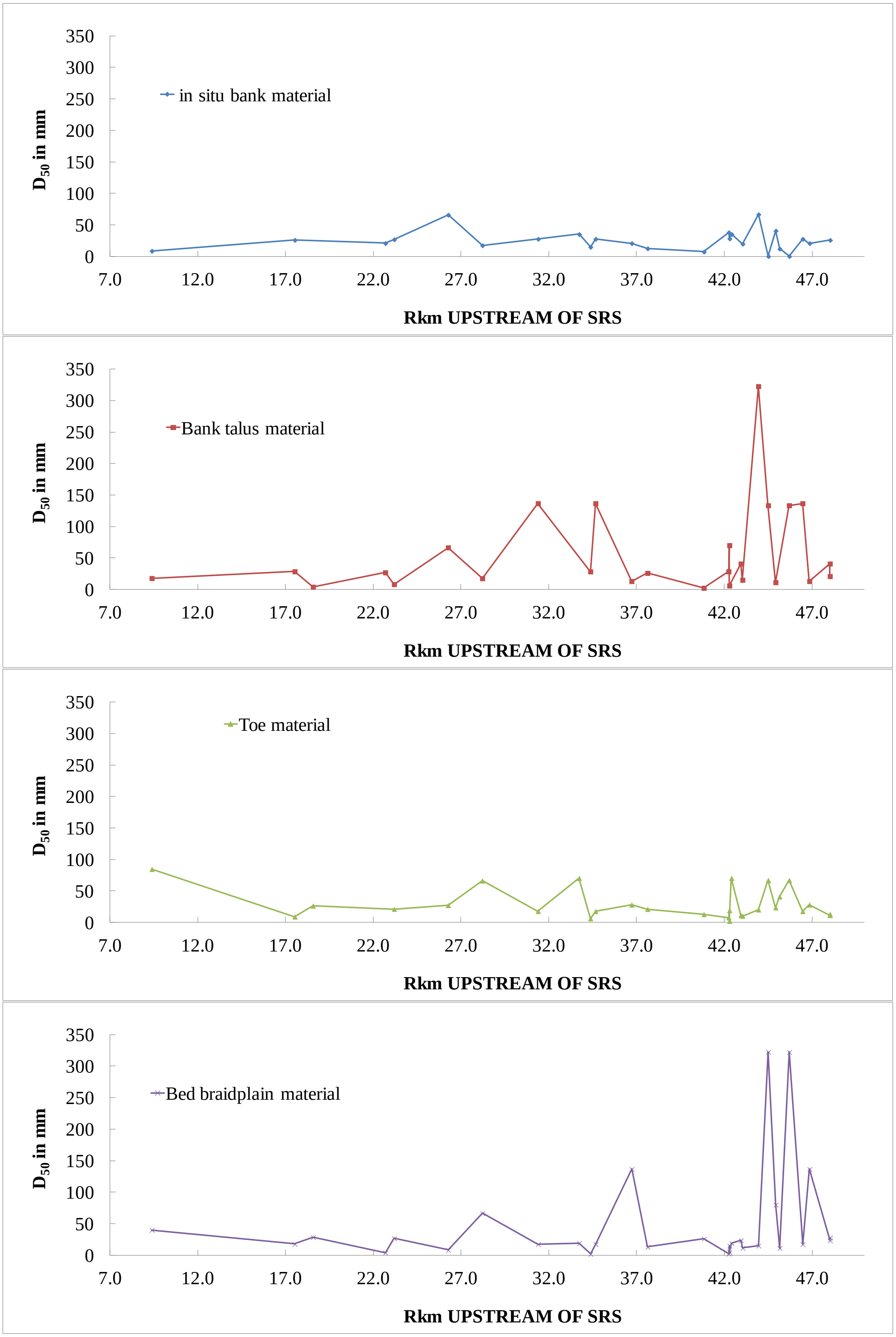

Figure 54. Median particle diameter, D_{50}, for *in situ* bank material, talus, bank toe and braidplain material sampled by USDA 2009-10.

9.2 Particle Size Distributions for Predicted Eroded Materials

Longitudinal plots of predicted bank erosion volumes in cubic yards are shown in Figure 55. The volumes have been separated out into three particle size classes of interest: <0.25 mm, 0.25 to 2.0 mm and >2 mm. The general trend was for predicted bank erosion in all size classes to increase moving downstream from 47.54 to 36.72 km upstream of the SRS. Following a decrease in predicted erosion at rkm 34.37, erosion volumes continued to increase again to rkm 28.21, before declining downstream to 17.52 km upstream of the SRS. Erosion volumes ranged from negative values (indicating net deposition) to 40.8 million cubic yards of eroded material over the modeled period (at rkm 36.72). The average eroded volume at each site over the modeled time period was 4.1 x 10^6 yd^3 of material (Table 24). The total eroded volume of bank and terrace materials from all sites over the modeled period was estimated to be approximately 103 x 10^6 yd^3 of material (Table 24); of that volume, 19.9 % was in the < 0.25 mm particle size category, 15.4 % was in the 0.25 to 2.0 mm particle size category, and 64.7 % was in the >2 mm particle size category (Table 25). The percentage contribution from each size class varied by site, with the 0.25 to 2.0 mm sized class contributing from 6.4 to 27.5 % of the eroded volume at each site, and an average of 19.0 % (Table 25).

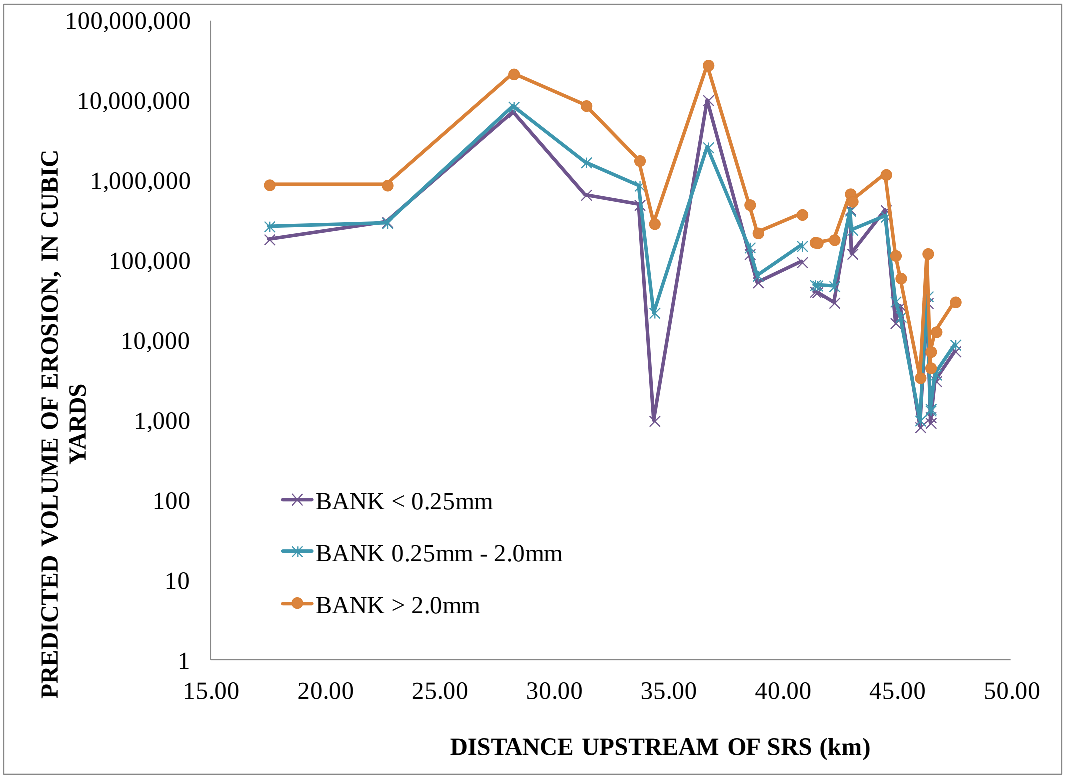

Figure 55. Volumes of bank erosion predicted by BSTEM-Dynamic 1.0 for the three particle size classes of interest; < 0.25 mm, 0.25 – 2.00 mm and >2.00 mm. Data provided in Table 24.

Table 24. Volumes of bank erosion predicted by BSTEM-Dynamic 1.0 for the three particle size classes of interest; < 0.25 mm, 0.25 – 2.00 mm and >2.00 mm.

				ERODED VOLUME (CUBIC YARDS)			
		rKm	**Description**	**<0.25**	**0.25-2.0**	**>2.0**	TOTAL
BANKS	MODELED REACHES - BANKS	17.52	NF375	1.85E+05	2.68E+05	8.90E+05	1.34E+06
		22.68	NF350	3.04E+05	2.96E+05	8.80E+05	1.48E+06
		28.21	NF310	7.18E+06	8.45E+06	2.17E+07	3.73E+07
		31.38	NF300	6.66E+05	1.70E+06	8.71E+06	1.11E+07
		33.72	CA230	4.99E+05	8.68E+05	1.79E+06	3.15E+06
		34.37	CW280	9.89E+02	2.23E+04	2.91E+05	3.14E+05
		36.72	NF125	1.02E+07	2.62E+06	2.80E+07	4.08E+07
		38.54	SF Coldwater	1.21E+05	1.46E+05	5.02E+05	7.69E+05
		38.90	Lower Carbonate Springs	5.35E+04	6.48E+04	2.22E+05	3.41E+05
		40.83	NF110	9.58E+04	1.53E+05	3.78E+05	6.26E+05
		40.97	Studebaker	-3.56E+03	-4.31E+03	-1.48E+04	-2.27E+04
		41.40	Upper Carbonate Springs	4.08E+04	4.94E+04	1.70E+05	2.60E+05
		41.50	Upper Glacier	4.03E+04	4.88E+04	1.68E+05	2.57E+05
		42.24	NF105	2.97E+04	4.79E+04	1.83E+05	2.61E+05
		42.94	LO100	4.35E+05	4.22E+05	6.87E+05	1.54E+06
	NON-MODELED REACHES BANKS	43.03	TR100	1.22E+05	2.43E+05	5.53E+05	9.17E+05
		44.50	TR65	4.28E+05	3.56E+05	1.20E+06	1.98E+06
		44.92	LO40	1.65E+04	3.08E+04	1.16E+05	1.63E+05
		45.15	LO33	2.70E+04	1.98E+04	6.04E+04	1.07E+05
		46.00	Unnamed Loowit Tribs	8.24E+02	9.99E+02	3.43E+03	5.25E+03
		46.33	Step32	2.95E+04	3.58E+04	1.23E+05	1.88E+05
		46.45	Step31L	1.10E+03	1.33E+03	4.57E+03	7.00E+03
		46.46	LO32	9.33E+02	1.40E+03	7.28E+03	9.61E+03
		46.70	Step31R (mid)	3.10E+03	3.76E+03	1.29E+04	1.98E+04
		47.54	Step30	7.33E+03	8.88E+03	3.05E+04	4.67E+04
			TOTALS	2.05E+07	1.59E+07	6.66E+07	**102,992,535**
			PERCENTAGES	19.90%	15.39%	64.71%	

Table 25. Percentages of eroded material, by class size, as predicted by BSTEM-Dynamic 1.0 for the three particle size classes of interest; < 0.25 mm, 0.25 – 2.00 mm and >2.00 mm.

				PERCENTAGE OF ERODED VOLUME IN SIZE CLASS		
		rKm	**Description**	**<0.25**	**0.25-2.0**	**>2.0**
BANKS	MODELED REACHES - BANKS	17.52	NF375	13.7%	20.0%	66.3%
		22.68	NF350	20.5%	20.0%	59.5%
		28.21	NF310	19.2%	22.6%	58.1%
		31.38	NF300	6.0%	15.3%	78.7%
		33.72	CA230	15.8%	27.5%	56.7%
		34.37	CW280	0.3%	7.1%	92.6%
		36.72	NF125	25.0%	6.4%	68.6%
		38.54	SF Coldwater	15.7%	19.0%	65.3%
		38.90	Lower Carbonate Springs	15.7%	19.0%	65.3%
		40.83	NF110	15.3%	24.4%	60.3%
		40.97	Studebaker	15.7%	19.0%	65.3%
		41.40	Upper Carbonate Springs	15.7%	19.0%	65.3%
		41.50	Upper Glacier	15.7%	19.0%	65.3%
		42.24	NF105	11.4%	18.4%	70.2%
		42.94	LO100	28.2%	27.3%	44.5%
	NON-MODELED REACHES BANKS	43.03	TR100	13.3%	26.4%	60.3%
		44.50	TR65	21.6%	17.9%	60.5%
		44.92	LO40	10.1%	18.8%	71.0%
		45.15	LO33	25.2%	18.5%	56.3%
		46.00	Unnamed Loowit Tribs	15.7%	19.0%	65.3%
		46.33	Step32	15.7%	19.0%	65.3%
		46.45	Step31L	15.7%	19.0%	65.3%
		46.46	LO32	9.7%	14.5%	75.8%
		46.70	Step31R (mid)	15.7%	19.0%	65.3%
		47.54	Step30	15.7%	19.0%	65.3%
			AVERAGE	16%	19%	65%

10. SUMMARY AND CONCLUSIONS

The UNFT River Basin remains an incredibly dynamic fluvial system 30 years after the catastrophic eruption of Mount St Helens in 1980. Incision of up to about 40 m has created a network of canyons through which flows of the UNFT River and its tributaries often seem dwarfed. Much of the incision occurred during particularly high flow events, caused by both ‘natural’ hydrologic events as well as those enhanced by human activities such as pumping from debris-dammed lakes. An estimated 76% of the incision took place during three periods of variable length: (1) the high flows of 1982 which included the breakout of Jackson Lake and pumping at a rate of 5 m^3/s from Spirit Lake, (2) the February 1996 flow event, the largest in the post-eruption period, and (3) the unique November 2006 which combined an estimated 100-year rainfall event with the capture of drainage area and a possible breakout of a debris-jammed channel. Vertical incision into debris avalanche and pyroclastic flow deposits set the stage for lateral erosion of streambanks and terrace slopes.

Lateral erosion has become the dominant process and source of sediment in the system, contributing an estimated 80% of the material being eroded from the channel boundaries. Over the 30 year post-eruption period, about 408 million yd^3 of material has been eroded from the UNFT. Some of this material has been deposited in downstream reaches, particularly in the sediment plain upstream of the SRS. Thus, by 2010, 374 million yd^3 of eroded sediment had been delivered to N-1 (the downstream limit of this study). Non-linear regressions of bed and bank erosion at each cross-section over time were solved for a range of years and multiplied by the distance to the next downstream cross section to obtain erosion volumes. Cumulative erosion of sediment delivered to the N-1 structure by 2010 was also computed in this way as a check on both methods. The calculated erosion volumes differed by only 1.5%. Results for predicted erosion volumes emanating from the bed and banks, as well as totals provide two important conclusions regarding future erosion rates: (1) streambank erosion is the dominant source of sediment, and (2) rates of erosion clearly decay non-linearly with time.

Projections of calculated erosion volumes to 2035 fall between recent estimates by others. Further extrapolation of sediment delivery to N-1 2010 through 2110 indicates erosion of an additional 130 million yd^3, bringing the cumulative total to 509 million yd^3.

Long-term (100 years) erosion rates were also predicted at 15 sites using the mechanistic model BSTEM-Dynamic 1.0. Initial modeling difficulties were solved by adjusting critical shear stress values for the generally lower specific gravity of the sediments. This was accomplished through derived relations based on the percentage of the various geologic types comprising the debris avalanche. The roughness coefficient, Manning’s n, was then adjusted to calibrate model output to surveyed geometry. Conversion from eroded areas at each site to volume over adjacent reaches was achieved by multiplying by the distance between cross sections.

As hypothesized, results of the 100-year simulations clearly indicate a non-linear decay of erosion rates with time. While the empirical analysis shows a smooth decay with time as defined by the logarithmic regressions employed, simulation results display a stair-stepped trend and reflect the episodic nature of the erosion process. Peak erosion rates for each of the 15-year flow periods diminish non-linearly with time as applied shear stresses decrease with channel widening.

Erosion rates predicted with BSTEM-Dynamic for the period 2010-2110 are 103 x 10^6 yd^3, about 3% more than predicted empirically. Given the great differences in the two approaches of obtaining predictions, these results are encouraging. Most of this eroded material is coarser than 2 mm, with about 19% of it in the important 0.25 – 2.0 mm size class.

ACKNOWLDEGMENTS

The funding for this research was provided by the U.S. Army Corps of Engineers, Portland District, where Chris Nygaard and Paul Sclafani provided straightforward management and oversight of the work. Thank you for being understanding during the trials and tribulations of this project and for lending a hand and getting dirty in the field.

This project would not have been successful without the combined, dedicated efforts of the staff of the Watershed Physical Processes Research Unit, National Sedimentation Laboratory. These are the people that don’t get their names on the covers of reports but work tirelessly both in the field and at their computers to help produce an excellent research product. We thank Lauren Klimetz, Rob Thomas and Brian Bell for their field work assistance and analysis of the cross section data. We also thank friends and colleagues from around the country who agreed to assist us working very long hours in the field: They are: Nick Jokay, Nathan Shasha, Sol Brich, Lisa Carter, Janine Castro, Tyler Joki, Brian Zabel, Paul Bakke, Desiree Tullos, Staci Pomeroy, John Higson, and Yavuz Ozeren. This project could not have been completed without their help.

Major thanks go to Kurt Spicer, USGS, Cascades Volcano Observatory (CVO), Kurt Spicer, not only for his expertise in the field locating surveys and collecting data, but in supplying historical data as well as providing first-hand knowledge of the area. Also to Adam Mosbrucker, and Tami Christianson at CVO. Mick Ursic, of the USDA-ARS provided de-bugging support and additional coding of BSTEM-Dynamic to handle the somewhat unique conditions on the UNFT. For this we are grateful.

We would like to thank Hillsboro Aviation and our pilots, Buckey McKay and James Brown. They went above and beyond just being pilots. Their customer service was paramount and they handled our needs efficiently. We had no issue putting our lives in their hands daily.

Given the amount of work that had to be completed over the duration of this project, the assistance provided by the people and agencies listed above were absolutely crucial. It is encouraging to see in this day and age, the kind of inter-agency cooperation that occurred during the course of this research. We thank you.

REFERENCES

Abernethy, B., and Rutherfurd, I.D., 2001. The distribution and strength of riparian tree roots in relation to riverbank reinforcement. Hydrological Processes, 15(1), 63-79.

Bagnold, R.A., 1966. An approach to the sediment transport problem from general physics. U.S. Geological Survey Professional Paper 422-I. US Government Printing Office: Washington, DC.

Begin, Z. B., Meyer, D. F. and Schumm, S. A. 1981. Development of longitudinal profiles of alluvial channels in response to bed-level lowering, Earth Surface Processes and Landforms, 6, 49-68.

Biedenharn Group, 2010. Cowlitz-Toutle River Watershed Sediment Budget. Vicksburg, Mississippi, 62 p.

Blatt, H., Middleton, G., and Murray, R., 1980. Origin of Sedimentary Rocks (2nd Ed.). Prentice Hall, Englewood Cliffs, NJ, 634 p.

Buffington, J.F., 1999. The legend of A. F. Shields. Journal of Hydraulic Engineering, 125(4), 376-387.

Bull, W.B., 1979. Threshold of critical power in streams. Bull. Geological Society of America, 90, 453-464.

Chow, V.T., 1959. Open Channel Hydraulics. McGraw-Hill: New York, NY.

Coppin, N.J., and Richards, I.G., 1990. Use of Vegetation in Civil Engineering. Butterworths: London, UK.

Daniels, H. E., 1945, The statistical theory of the strength of bundles of threads, I., Proc. R. Soc. London, Ser. A., 183, 405– 435.

Davies, T.R.H. and Sutherland, A.J., 1983. Extremal hypotheses for river behavior. Water Resources Research, 19 (1):141-148.

Endo, T., and Tsuruta, T., 1969. On the effect of tree roots upon the shearing strength of soil. Annual report of the Hokkaido branch, Forest Place Experimental Station: Sapporo, Japan; pp.167-183.

Einstein, H.A. (1942). Formulas for the Transport of Bed Sediment. Trans. American Society of Civil Engineers, Vol. 107, pp. 561-574

Ennos, A.R., 1990. The anchorage of leek seedlings: The effect of root length and soil strength. Annals of Botany, 65(4), 409-416.

Fan, C.-C., and Su, C.-F., 2008. Role of roots in the shear strength of root-reinforced soils with high moisture content. Ecological Engineering, 33(2), 157-166.

Fredlund, D.G., and Rahardjo, H., 1993. Soil Mechanics of Unsaturated Soils. John Wiley and Sons, Inc.: New York.

Fredlund, D.G., Morgenstern, N.R., and Widger, R.A., 1978. The shear strength of unsaturated soils. Canadian Geotechnical Journal, 15, 313-321.

Gomez, B., 1983. ‘Temporal variations in bedload transport rates: The effect of progressive bed armoring’, Earth Surface Processes and Landforms, 8, 41-54.

Graf, W.L., 1977. The rate law in fluvial geomorphology. American Journal of Science, 277, 178-191.

Gray, D.H., and Leiser, A.T., 1982. Biotechnical Slope Protection and Erosion Control. Van Nostrand Reinhold Company: New York, NY.

Gray, D.H., and Sotir, R.B., 1996. Biotechnical and Soil Bioengineering Slope Stabilization: A Practical Guide for Erosion Control. John Wiley & Sons, Inc.: New York, NY.

Hanson, G.J., and Simon, A., 2001. Erodibility of cohesive streambeds in the loess area of the midwestern USA, Hydrological Processes, 15(1), 23-38.

Hanson, G.J., 1990, Surface erodibility of earthen channels at high stress, Part II - Developing an in situ testing device, Transactions of the American Society of Agricultural Engineers, 33(1), 132-137.

Hanson, G. J., 1991. Development of a Jet Index to Characterize Erosion Resistance of Soils in Earthen Spillways. Transactions of the ASAE. Volume 34(5), 2015-2020 p.

Hoek, E. and Bray, J.D., 1977. Rock Slope Engineering. Spon Press. pp368.

Hjulström, F., 1935. The morphological activity of rivers as illustrated by River Fyris. Bulletin of the Geological Institute, University of Uppsala, 25(3), 221-527.

Humboldt Manufacturing, 2011a. http://www.humboldtmfg.com/datasheets/Shear_Vane.pdf, accessed December 30, 2011.

Humboldt Manufacturing, 2011b. http://www.humboldtmfg.com/manuals/H-4200_Soil_Penetrometer.pdf, accessed December 30, 2011.

Karcz, I., 1980. Thermodynamic approach to geomorphic thresholds. In: D.R. Coates and J.D. Vitek (Editors), Thresholds in Geomorphology. George A1len & Unwin, London, p. 209-226.

Knighton, A.D., 1998. Fluvial Forms and Processes: A New Perspective. Arnold: London, UK.

Langendoen, E.J., 2010. Assessing post-dam removal sediment dynamics using the CONCEPTS computer model. In: Proceedings of the 2nd Joint Federal Interagency Conference, Las Vegas, NV, June 27-July 1, 2010, 12 p.

Laursen, E.M., 1958. The total sediment load of streams. Journal of the Hydraulics Division, ASCE, 84, 1530-1–1530-36.

Leopold, L.B., and Langbein, W.B. 1962. The concept of entropy in landscape evolution. U.S. Geol. Surv. Prof. Paper 500-A.

Lohnes, R.A., Handy, R.L., 1968. Slope angles in friable loess. J. Geol. 76 _3., 247–258.

Major, J.J., and Mark, L.E., 2006. Peak flow responses to landscape disturbances caused by the cataclysmic 1980 eruption of Mount St. Helens, Washington. GSA Bulletin, 118(7/8), 938-958.

Major, J.J., Pierson, T.C., Dinehart, R.L., and Costa, J.E., 2000. Sediment yield following severe volcanic disturbance – A two-decade perspective from Mount St. Helens. Geology, 28(9), 819-822.

Meyer, D.F. and Dodge, J.E., 1988. Post-eruption changes in channel geometry of streams in the Toutle River drainage basin, 1983-85, Mount St. Helens, Washington, 226 p.

Meyer-Peter, E., and Müller, R., 1948. Formulas for bed-load transport. In: 2nd Meeting of the International Association for Hydraulic Structures Research, 7-9 June, 1948, Stockholm, 39-64.

Meyer, D.F., Nolan, K.M.m and Dodge, J.E., 1986. Post-eruption changes in channel geometry of streams in the Toutle River drainage basin, 1980-82, Mount St. Helens, Washington. U.S. Geological Survey Open-File Report 85-412, Tacoma Washington, 128 p.

Micheli, E.R., and Kirchner, W., 2002. Effects of wet meadow riparian vegetation on streambank erosion. 2. Measurements of vegetated bank strength and consequences for failure mechanics. *Earth Surface Processes and Landforms*, 27: 687-697.

Morgenstern, N.R., and Price, V.R., 1965. The analysis of the stability of general slip surfaces. Geotechnique, 15, 79-93.

Paine, A.D.M., 1984. Canyon and terrace formation near Mount St. Helens, Washington (M.S. thesis), Colorado State University, Fort Collins, Colorado, 157 p.

Parker, R.S., 1977. Experimental study of drainage system evolution and its hydrologic implications. Hydrology Papers No. 90, Colorado State University, 58 pp.

Parker, G., 1990. Surface-based bedload transport relation for gravel rivers. Journal of Hydraulic Research, 28(4), 417-436.

Partheniades, E., 1965. Erosion and deposition of cohesive soils. Journal of the Hydraulics Division, ASCE, 91(HY1), 105-139.

Pollen, N., 2007. Temporal and spatial variability in root reinforcement of streambanks: Accounting for soil shear strength and moisture. Catena, 69(3), 197-205.

Pollen, N., and Simon, A., 2005. Estimating the mechanical effects of riparian vegetation on streambank stability using a fiber bundle model. Water Resources Research, 41, W07025, doi:10.1029/2004WR003801.

Pollen, N., Simon, A., and Collison, A.J.C., 2004. Advances in assessing the mechanical and hydrologic effects of riparian vegetation on streambank stability. In: S. Bennett and A. Simon, (eds.), Riparian Vegetation and Fluvial Geomorphology, Water Science and Applications 8. AGU: Washington, DC; pp.125-139.

Press, W.H., Teukolsky, S.A., Vetterling, W.T., and Flannery, B.P., 1992. Numerical Recipes in C: The Art of Scientific Computing (2nd edn.). New York, Cambridge Univ. Press, 994 pp.

Riestenberg, M., and Sovonick-Dunford, S.S., 1983. The role of woody vegetation in stabilizing slopes in the Cincinnati area. Ohio, Geological Society of America Bulletin, 94(4), 506-518.

Rinaldi, M., and Simon, A., 1998, Adjustments of the Arno River, Central Italy, Geomorphology, 22: 57-71.

Shields, A. (1936). Application of similarity principles and turbulence research to bed-load movement. W.P. Ott, and J.C. van Uchelen (translators), Hydrodynamics Laboratory Publication 167. USDA Soil Conservation Service Cooperative Laboratory, California Institute of Technology: Pasadena, CA.

Simon, A., 1989. A model of channel response in disturbed alluvial channels. Earth Surface Processes and Landforms, 14(1), 11-26.

Simon, A. 1991. Channel hydraulics and energy expenditure in channel adjustment: Elk Rock reach, North Fork Toutle River, Washington (Abstr.). Geol. Soc. Am. Abstr. With programs, 23L A88.

Simon, A., 1992, Energy, time, and channel evolution in catastrophically disturbed fluvial systems. Geomorphology, 5, 345-372.

Simon, A., 1994. Gradation processes and channel evolution in modified West Tennessee streams: Process, response and form. U.S. Geological Survey Professional Paper 1470, 84 p.

Simon, A., 1999. Channel and drainage-basin response of the Toutle River System in the aftermath of the 1980 eruption of Mount St. Helens, Washington. U.S. Geological Survey Open-File Report 96-633, Vancouver, Washington, 130 p.

Simon, A., and Collison, A.J.C., 2002. Quantifying the mechanical and hydrologic effects of riparian vegetation on stream-bank stability, Earth Surface Processes and Landforms, 27(5), 527-546.

Simon A., Curini A.. 1998. Pore pressure and bank stability: The influence of matric suction. *In* Water Resources Engineering '98*, ed.* Abt S.R., 358-363. New York*:* American Society of Civil Engineers.

Simon A, Curini A, Darby S.E, Langendoen E.J., 2000. Bank and near-bank processes in an incised channel, *Geomorphology* 35: 183-217.

Simon, A., and Darby, S.E., 1997. Process-form interactions in unstable sand-bed river channels: A numerical modeling approach. Geomorphology, 21: 85-106.

Simon A., and Rinaldi, M., 2000, Channel instability in the loess area of the midwestern United States. Journal of American Water Resources Association, 36: 133-150.

Simon, A., and Rinaldi, M. 2006. Disturbance, stream incision, and channel evolution: The roles of excess transport capacity and boundary materials in controlling channel response. *Geomorphology* 79: 361-383.

Simon, A. and Robbins, C.H., 1987. Man-induced gradient adjustment of the South Fork Forked Deer River, West Tennessee. Environmental Geology and Water Science, 9(2), 109-118.

Simon, A., and Thorne, C.R., 1996. Channel adjustment of an unstable coarse-grained stream: Opposing trends of boundary and critical shear stress, and the applicability of extremal hypotheses. Earth Surface Processes and Landforms, 21, 155-180.

Smith, G.A., and Smith R.D., 1985. Specific gravity characteristics of recent volcaniclastic sediment: Implications for sorting and grain size analysis. Journal of Geology, 93: 619-622.

Temple, D.M., 1980. Tractive force design of vegetated channels. Transactions of the American Society of Agricultural Engineers, 23(4), 884-890.

Temple, D.M., Robinson, K.M., Ahring, R.M., and Davis, A.G., 1987. Stability Design of Grass-Lined Open Channels. USDA ARS Agriculture Handbook Number 667. US Government Printing Office: Washington, DC.

Terzaghi, K., and Peck, R. B. 1967. *Soil mechanics in engineering practice*, Wiley, New York.

Thomas, R.E., and Pollen-Bankhead, N., 2010. Modeling root-reinforcement with a fiber-bundle model and Monte Carlo simulation. Ecological Engineering, 36(1), 47-61.

Thorne, C.R., 1990. Effects of vegetation on riverbank erosion and stability, In: J.B. Thornes, (ed.), Vegetation and Erosion. John Wiley & Sons Ltd.: Chichester, UK; pp.125-144.

Thorne, C.R., and Tovey, N.K., 1981. Stability of composite river banks. Earth Surface Processes and Landforms, 6, 469-484.

van Genuchten, M. Th., 1980. A closed-form equation for predicting the hydraulic conductivity of unsaturated soils. Soil Science Society of America Journal, 44, 892-898.

van Rijn, L.C., 1984a. Sediment transport, Part I: Bed Load Transport. Journal of Hydraulic Engineering, ASCE, 110(10), 1431-1456.

van Rijn, L.C., 1984b. Sediment transport, Part II: Suspended Load Transport. Journal of Hydraulic Engineering, ASCE, 110(11), 1613-1641.

Waldron, L.J., 1977. The shear resistance of root-permeated homogeneous and stratified soil. Soil Science Society of America Journal, 41(5), 843-849.

Waldron, L.J., and Dakessian, S., 1981. Soil reinforcement by roots: Calculation of increased soil shear resistance from root properties. Soil Science, 132(6), 427-435.

West Consultants, 2002. Mount St. Helens Engineering Reanalysis Hydrologic, Hydraulic and Sedimentation Analysis, Volume 1: Technical Report. Bellvue, Eashington, 185 p.

Williams, G.P. and Wolman, M.G., 1984. Downstream effects of dams on alluvial rivers. U.S. Geological Survey Professional Paper, 1286, 83 pp.

Wolman, M.G., 1955. The natural channel of Brandywine Creek, Pennsylvania. U.S. Geological Survey Professional Paper., 271, 56 p., 36: 133-150.

Wu, T.H., 1984. Effect of vegetation on slope stability, Transportation Research Record, 965, 37-46.

Wu, T.H., McKinnell III, W.P., and Swanston, D.N., 1979. Strength of tree roots and landslides on Prince of Wales Island, Alaska. Canadian Geotechnical Journal, 16(1), 19-33.

Wu, W, Wang, S.S.Y., and Jia, Y., 2000. Nonuniform sediment transport in alluvial rivers. Journal of Hydraulic Research, 38(6), 427-434.

Yang, C.T., 1973. Incipient motion and sediment transport. Journal of the Hydraulics Division, ASCE, 99(HY10), 1679-1704.